



저작자표시-비영리-동일조건변경허락 2.0 대한민국

이용자는 아래의 조건을 따르는 경우에 한하여 자유롭게

- 이 저작물을 복제, 배포, 전송, 전시, 공연 및 방송할 수 있습니다.
- 이차적 저작물을 작성할 수 있습니다.

다음과 같은 조건을 따라야 합니다:



저작자표시. 귀하는 원저작자를 표시하여야 합니다.



비영리. 귀하는 이 저작물을 영리 목적으로 이용할 수 없습니다.



동일조건변경허락. 귀하가 이 저작물을 개작, 변형 또는 가공했을 경우에는, 이 저작물과 동일한 이용허락조건하에서만 배포할 수 있습니다.

- 귀하는, 이 저작물의 재이용이나 배포의 경우, 이 저작물에 적용된 이용허락조건을 명확하게 나타내어야 합니다.
- 저작권자로부터 별도의 허가를 받으면 이러한 조건들은 적용되지 않습니다.

저작권법에 따른 이용자의 권리는 위의 내용에 의하여 영향을 받지 않습니다.

이것은 [이용허락규약\(Legal Code\)](#)을 이해하기 쉽게 요약한 것입니다.

[Disclaimer](#)

공학박사학위논문

에너지 저장 및 환경 모니터링 소자용
산화주석계 이종접합 나노구조의 제조와 특성 평가

Synthesis of SnO₂-based Hetero-nanostructure
and Their Applications
for Environmental Monitoring and Energy Storage

2014 년 2월

서울대학교 대학원

재료공학부

전 정 훈

Abstract

Nanoporous materials have been attracted many attention due to its high-surface-to-volume ratio and structural features resulting their peculiar and fascinating properties. Various synthesis techniques have been suggested and the enhanced physical and chemical properties of nanoporous materials are confirmed in various fields such as optic device, sensors, and energy application.

In this research, the two main topics will be discussed: 1) synthesis of Sn-based porous structure using electrochemical methods and their gas sensing properties, 2) electrochemical performance of $\text{SnO}_2/\text{TiO}_2$ heterostructured nanotube synthesized by atomic layer deposition and PAN template

In the first chapter, nanoporous Sn based nanostructures for semiconductor gas sensor is synthesized via electrochemical methods, anodic oxidation and electrodeposition. Tin oxide is a well-known semiconductor-type gas sensor material detecting inflammable and toxic gases and the gas adsorption/desorption on the surface of sensor material changes its electric resistivity. Therefore, the surface area is one of the key factors to determine the gas sensing performance such as sensitivity, selectivity, and response-recovery time. In order to synthesize a porous structure, electrochemical methods of anodizing (top-down) and electrodeposition (bottom-up) are chosen. The synthesized porous structures

exhibited enhanced gas sensing properties in terms of gas response, reaction time and recovery time and it is confirmed that the structural effect of porous structure lead to improved sensing performance. In addition, heterostructuring with CuO forming PN junction is applied to give functionality on selective sensing toward H₂S and the mechanism on enhanced selectivity toward H₂S is investigated.

In the second chapter, synthesis of SnO₂/TiO₂ hetero-structured nanotube for anode material of Li ion battery is studied. The technical needs for high performance lithium ion batteries (LIBs) have increased in a wide range, from hybrid electric vehicles (HEVs) to light-weight and portable electronic devices. In this manner, SnO₂ is one of the promising materials for anode electrode in LIBs due to its high theoretical capacity (782 mAh g⁻¹) to replace commercially used graphite-based materials (372 mAh g⁻¹). However, a large volume expansion about 300% during lithium insertion/extraction causes a pulverization and electrical connectivity loss. Hollow nanotube is the most promising structure due to the interior free space accommodating the volume change during lithiation/delithiation. In addition, titanium dioxide (TiO₂) as anode materials of LIBs is considered another promising anode material in term of achieving higher safety and stability even though it shows low reversible capacity (170 mAh g⁻¹). The volume change of TiO₂ is less than 4% during the formation of typical Li-ion intercalation compound in the reaction, which thus greatly improves the overall

safety of battery and this structural stability enable outstanding faster charge/discharge properties at high C-rate. So, to obtain solution for practical implementation, heterostructure of SnO₂ and TiO₂ nanotubes resulting synergetic effect is suggested for the anode of LIBs. The electrochemical performances of the products are investigated and highly enhanced properties of SnO₂/TiO₂ hetero-nanotube are confirmed especially in term of reversible capacity and high rate cyclability.

Keywords: Nanostructure, Porous structure, Anodic oxidation, Electrochemical deposition, Nanotube, ALD (atomic layer deposition), RIE(Reactive ion etching), Semiconductor gas sensor, Li-ion battery, Anode, Sn, CuO, Cu₆Sn₅, SnO₂, TiO₂.

Student Number: 2009-31239

Table of Contents

Abstract	i
Contents	iv
List of figures	vi
 Chapter 1. General Background	 1
1.1 Electrochemical methods for the synthesis of nanoporous structure....	2
1.1.1. Anodic oxidation.....	2
1.1.2. Electrodeposition	4
1.2. Semiconductor gas sensor.....	5
1.2.1 Working mechanism	5
1.2.2 SnO ₂ gas sensor	8
1.3. Lithium-ion battery.....	8
1.3.1. Reaction mechanism	9
1.3.2. SnO ₂ based anode materials	10
1.4. Reference	17
 Chapter 2. Synthesis of porous SnO₂ based Nanostructures for Gas Sensing Application	 20
2.1. Introduction	21
2.2. Synthesis of Nanoporous SnO ₂ via anodic oxidation and its gas sensing properties	23
2.3. Nanoporous SnO ₂ /CuO via anodic oxidation and reactive ion	

etching and its gas sensing mechanism.....	40
2.4. The synthesis of porous SnO ₂ dendrite via electrodeposition and its gas sensing property	58
2.5 3-D nanoporous SnO ₂ /CuO hybrid dendrite via co-electrodeposition and its gas sensing property	75
2.6 References.....	98
 Chapter 3. Heterostructured nanotube of SnO₂ and TiO₂ for Li	
ion Battery Application	105
3.1. Introduction.....	106
3.2. SnO ₂ @TiO ₂ double-shell nanotube and its electrochemical properties.....	110
3.3. TiO ₂ @SnO ₂ @TiO ₂ multi-shell nanotubes and its electrochemical properties	134
3.4. References.....	148
 Abstract (Korean)	153

List of Figures

Chapter 1

Figure 1.1 The pore formation at the beginning of the anodization. Regime 1: formation of barrier oxide on the entire area; regime 2: local field distributions caused by the surface fluctuations; regime 3: creation of pores by field-enhanced or/and temperature-enhanced dissolution; regime 4: stable pore growth

Figure 1.2. Schematic diagram of current density curve during the initial growth at constant voltage. j_b and j_p indicate the current density for the barrier film and the porous film formation, respectively. j_{hp} represents a hypothetical current density, which is the difference between j_p and j_b .

Figure 1.3 The mechanism of CO gas sensing in SnO_2 gas sensor

Figure 1.4 Band diagram of O_2 adsorption on the surface of n-type semiconductor SnO_2

Figure 1.5 Lithium-ion rechargeable battery mechanism

Figure 1.6 The specific capacity of group IV elements

Chapter 2

Figure 2.2.1 (a) Plain view of as-deposition Sn film on Si/SiO₂ substrate and (b) its cross-sectional view

Figure 2.2.2 Current density-time transients at constant applied voltage of 6 V during anodizing of as-deposited Sn films.

Figure 2.2.3 Plain and cross-sectional views of as-anodized films anodized at 5°C for (a) 15, (b) 30, (c) 60, and (d) 90 s.

Figure 2.2.4 Plain and cross-sectional views of as-anodized films anodized for 15 sec at (a, b) 5, (c, d) 15, (e, f) 25 °C

Figure 2.2.5 (a) Plain and (b) cross-sectional views of as-annealed films at 700°C for 1h

Figure 2.2.6 TEM image of as-annealed films

Figure 2.2.7 X-ray diffraction pattern of (a) as-prepared Sn film, (b) as-anodized film, (c) as-annealed film at 500°C for 1h, (d) as-annealed film at 700°C for 1h

Figure 2.2.8 XPS spectra of as-prepared Sn film (dash line), as-anodized film (solid line) and as-annealed film (dot line)

Figure 2.2.9 Gas sensing transient of nanoporous SnO₂ film at 400°C

Figure 2.2.10 Gas reponse of nanoporous SnO₂ film at 400°C

Figure 2.2.11 Gas response of nanoporous SnO₂ according to operating temperature and H₂ concentration

Figure 2.2.12 Gas response of nanoporous SnO₂ commercial SnO₂ powder, thermally oxidized SnO₂ sensor toward NH₃ and CO gases

Figure 2.3.1 Morphology changes with the variation of CF₄ flow for 7 min; (a) 10, (b) 20, (c) 30 sccm

Figure 2.3.2 Morphology changes with the variation of etching time with 10 sccm of CF₄; (a) 5, (b) 7, (c) 10 min

Figure 2.3.3 Plain and cross-sectional view of (a, c, e) as-etched film and (b, d, f) as-annealed film

Figure 2.3.4 Plain view of as-CuO impregnated film

Figure 2.3.5 X-ray diffraction patterns; (a) as-Sn prepared film, (b) as-anodized film, (c) as-annealed film and (d) as-CuO impregnated film

Figure 2.3.6 The selected area electron diffraction pattern (SAED) and high resolution image of (a, b) as-anodized film and (b) as-annealed film

Figure 2.3.7 Gas sensing transient of nanoporous SnO₂-CuO film toward H₂S at 250 °C

Figure 2.3.8 Temperature dependence of gas response in nanoporous SnO₂-CuO sensor toward 20 ppm H₂S

Figure 2.3.9 Gas response of nano-porous CuO-SnO₂ sensor to H₂, CO, NH₃,

C₂H₅OH and H₂S at 250 °C

Figure 2.3.10 The (a) Cu2p and (b) S2p XPS spectra of nano-porous CuO-SnO₂ film before and after H₂S exposure at 250°C

Figure 2.3.11 (a) Bind energy shift of Sn3d_{5/2} and O1s and (b) electrical resistance changes as increasing reaction temperature with H₂S

Figure 2.4.1 SEM micrographs of Sn foam deposited on SiO₂ applying cathodic current density of 2Acm⁻² for (a) 5sec, (b) 10sec, (c) 15 sec and (d) detailed microstructure of (c), cross sectional view of interface between Sn deposits and substrate (e)

Figure 2.4.2 SEM micrographs of Sn foam deposited on SUS applying cathodic current density of 2Acm⁻² for (a) 5sec, (b) 10sec, (c) 15 sec and (d) detailed micrograph of (c)

Figure 2.4.3. SEM micrographs of SnO₂ foam on SiO₂ annealed at 600°C for 1h with 1 °C/min: Plain view (a, b) and its cross sectional view (c), and plain view (d) annealed at 700°C for 1h with 10 °C/min

Figure 2.4.4. XRD patterns of Sn foam deposited on SiO₂ (a) and treated at (b) 200°C, (c) 300°C, (d) 400°C, (e) 500°C, (f) 600°C

Figure 2.4.5. Response transient of porous SnO₂ foam sensor toward ethanol at

300 °C

Figure 2.4.6. Response time (a) and gas response (b) of porous SnO₂ foam toward ethanol as a function of operating temperature

Figure 2.4.7. Response time (a) and gas response (b) toward 10ppm ethanol : Comparison between those of porous SnO₂ foam and commercial SnO₂ powder.

Figure 2.4.8. Response time (a) and gas response (b) of porous SnO₂ foam toward various gases.

Figure 2.4.9. Changes of gas response during 30 cycle exposure toward 10 ppm ethanol at 300 °C

Figure 2.5.1 Surface morphology of porous foams electrodeposited in 1.5M H₂SO₄ electrolyte of different composition; (a) 0.15 M CuSO₄ • 5H₂O, (b) 0.1 M CuSO₄ • 5H₂O, 0.12 M SnSO₄, (c) 0.025 M CuSO₄ • 5H₂O, 0.14 M SnSO₄, (d) 0.15 M SnSO₄

Figure 2.5.2 X-ray diffraction pattern of porous foams electrodeposited in 1.5M H₂SO₄ electrolyte of different composition; (a) 0.15 M CuSO₄ • 5H₂O, (b) 0.1 M CuSO₄ • 5H₂O, 0.12 M SnSO₄, (c) 0.025 M CuSO₄ • 5H₂O, 0.14 M SnSO₄, (d)

0.15 M SnSO_4

Figure 2.5.3 (a) High magnitude image and (b) TEM image of synthesized nanodendrites, (c) tin and (d) copper element mapping images using EELS of (b).

Figure 2.5.4. X-ray diffraction pattern of stripped nanodendrite foam from copper foil

Figure 2.5.5 The cathodic linear sweep voltammetry of electrodeposition in 1.5M H_2SO_4 electrolyte of different composition; (1) curve 1: 0.15 M $\text{CuSO}_4 \cdot 5\text{H}_2\text{O}$, (2) curve 2: 0.15 M SnSO_4 , (3) curve 3: 0.125 M $\text{CuSO}_4 \cdot 5\text{H}_2\text{O}$, 0.15 M SnSO_4 , (4) curve 4: 0.027 M $\text{CuSO}_4 \cdot 5\text{H}_2\text{O}$, 0.15 M SnSO_4 .

Figure 2.5.6 Phase analysis of deposits synthesized in the electrolyte of different electrolyte composition; 0.125 M $\text{CuSO}_4 \cdot 5\text{H}_2\text{O}$, 0.15 M SnSO_4 at (a) -0.53V and (b) -0.78V, 0.027 M $\text{CuSO}_4 \cdot 5\text{H}_2\text{O}$, 0.15 M SnSO_4 at (c) -0.53V and (d) -0.78V.

Figure. 2.5.7 Current transient in electrolyte at -0.53, -0.78 and 1 V vs. SCE in different electrolyte composition of curve 3 ($\text{CuSO}_4\text{:SnSO}_4=0.027\text{:}0.15$ M) and curve 4 ($\text{CuSO}_4\text{:SnSO}_4=0.125\text{:}0.15$ M)

Figure 2.5.8 EDS spectra of synthesized deposits at -0.53, -0.78 and 1 V vs. SCE

in different electrolyte composition of curve 3 ($\text{CuSO}_4\text{:SnSO}_4=0.027\text{:}0.15$ M) and curve 4 ($\text{CuSO}_4\text{:SnSO}_4=0.125\text{:}0.15$ M)

Figure 2.5.9 SEM micrographs of the as-synthesized deposits on SiO_2/Si substrate by (a, b) electrochemical deposition, (c, d) the as-annealed films and (e~g) its STEM images with EDS mapping.

Figure 2.5.10 XRD patterns of Sn foams; (a) the as-deposited and (b) the heat treated at 700°C .

Figure 2.5.11 (a) Gas sensing transient of CuO/SnO_2 porous form, (b) gas response according to operating temperature and the long-term stability of gas sensing performance (c).

Figure 2.5.12 The comparison of gas sensing performance with other gases: (a) Gas response (R_a/R_g), (b) Response time ($t_{90\%}$).

Chapter 3

Figure 3.2.1 Schematic diagram of the fabrication procedures and schematic illustration of Li-ion insertion/extraction in $\text{SnO}_2@\text{TiO}_2$ double-shell nanotubes.

Figure 3.2.2 Morphologies of as-electrospun PAN nanofibers on wafer.

Figure 3.2.3 Characterization of $\text{SnO}_2@\text{TiO}_2$ double-shell nanotubes; a) FE-SEM and b) low magnification TEM images of double-shell nanotube network, c)

STEM image and EDS line profiles of individual double-shell nanotube (red line: Ti, green line: Sn), d) high magnification TEM image and SAED pattern of double-shell nanotube

Figure 3.2.4 STEM images with EDS mapping (green: Sn, red: Ti) and low-magnitude TEM images; the SnO₂-TiO₂ multi-shell nanotube of (a, b) 75 and (c, d) 150 ALD cycles for TiO₂ shell coating.

Figure 3.2.5 X-ray diffraction pattern of SnO₂@TiO₂ double-shell nanotubes

Figure 3.2.6 SnO₂ single shell nanotubes; (a) FE-SEM image, (b) STEM image and EDS line-profile (green: Sn, red: Ti), and (c) low-magnitude TEM image.

Figure 3.2.7 a) Charge/discharge voltage profile of SnO₂@TiO₂ nanotube electrode between 0.01 and 3.0 V at 800 mA g⁻¹, b) Columbic efficiency of SnO₂ and SnO₂@TiO₂ nanotube electrodes at 800 and 1500 mA g⁻¹, c) Cyclic voltammetry of SnO₂@TiO₂ nanotube electrode.

Figure 3.2.8 TEM images and SAED patterns at each potential in Figure 3.1.7c: a) discharge 2.0 V (point 1), b) discharge 0.2 V (point 2), c) charge 1.5V (point 3), and d) charge 2.9 V (point 4).

Figure 3.2.9 Charge/discharge voltage profile of SnO₂ nanotube electrode between 0.01 and 3.0 V at 800 mA g⁻¹.

Figure 3.2.10 Cyclability of SnO₂ and SnO₂@TiO₂ nanotube electrodes at (a) 800 and (b) 1500 mA g⁻¹, respectively.

Figure 3.2.11 Rate capability test of SnO₂@TiO₂ double shell nanotube

Figure 3.2.12 (a) The morphology of TiO₂ nanotube, (b) cycle performance and (c) charge/discharge voltage profile of TiO₂ nanotube electrode between 0.01 and 3.0 V at 800 and 1500 mA g⁻¹.

Figure 3.2.13 a) FESEM and b) TEM images of SnO₂ nanotube electrode after 5 cycles at 1500 mA g⁻¹, c) FESEM and d) TEM images of SnO₂@TiO₂ double-shell nanotube electrode after 5 cycles at 1500 mA g⁻¹, e) STEM image of individual double-shell nanotube in d), and (f, g) EDS element mapping of e)

Figure 3.2.14 (a) STEM image of SnO₂ nanotube electrode after 5 cycles at 1500 mA g⁻¹ and (b) EDS element mapping.

Figure 3.2.15 FESEM, STEM images, and element mapping of a, b) SnO₂ single-shell nanotube electrode and c, d) SnO₂@TiO₂ double-shell nanotube electrode after 50 cycles at 1500 mA g⁻¹.

Figure 3.3.1 (a) As prepared PAN and (b) As-coated PAN

Figure 3.3.2 (a, b) FESEM, (c) TEM images and (d) X-ray diffraction pattern of TiO₂@SnO₂@TiO₂ nanotube

Figure 3.3.3 (a) STEM analysis direction, (b) STEM image and its (c) line profile and (d, e) elements mapping image in inert square of (b)

Figure 3.3.4 FESEM, TEM images and X-ray diffraction pattern of (a~c) SnO_2 and (d~f) TiO_2 nanotube

Figure 3.3.5 (a) Charge/discharge voltage profile, (b) cyclic voltammetry, (c) cycle performances and (d) its coulombic efficiency of $\text{TiO}_2@\text{SnO}_2@\text{TiO}_2$ nanotube

Figure 3.3.6 (a) Rate performance and (b) coulombic efficiency of $\text{TiO}_2@\text{SnO}_2@\text{TiO}_2$ nanotube at varied current density

Chapter 1.

General Background

1.1 Electrochemical methods for the synthesis of nanoporous structure

Nano-porous structure exhibit special properties and features due to its large surface-to-volume ratio that usually cannot be achieved by their conventional dense structure. Therefore, porous materials find nowadays many applications as end products and in several technological processes. For the fabrication of porous structure, several synthesis methods have been developed including sol-gel process, membrane, spray pyrolysis and so on. Among them, electrochemical methods such as anodic deposition and electrodeposition is most commonly employed method for the synthesis of self-ordered porous structure, which is relatively simple, low cost, and high yield process. In this manner, we studied anodic oxidation, electrodeposition and template-based process for the synthesis of nano-porous structures and those applications

1.1.1. Anodic Oxidation

Anodizing increases corrosion resistance and wear resistance, and provides better adhesion for paint primers and glues than does bare metal. Anodic films can also be used for a number of cosmetic effects, either with thick porous coatings that can absorb dyes or with thin transparent coatings that add interference effects to reflected light.

Recently, Large scale and ordered nanoporous array is synthesized through anodic oxidation process in wide range of applications, separator, bio/chemical sensor, photonic crystals, solar cell electrode. The pore formation mechanism is displayed schematically in Figure 1.1, corresponding to the four regimes of Figure 1.2. [1]. At the beginning of the anodization, the barrier film, which consists of non-conductive oxide [2] covers the entire surface of the aluminum (regime 1 in Figure 1.1 and 1.2). The electric field is focused locally on fluctuations of the surface (regime 2 in Figure 1.1 and 1.2). This leads to field-enhanced or/and temperature enhanced dissolution in the formed oxide and thus to the growth of pores (regime 3 in Figure 1.1 and 1.2). Since some pores begin to stop growing due to competition among the pores, the current decreases again as shown in regime 4 in Figure 1.2. Finally, j_p maintains an equilibrated state. In this stage, pores grow in a stable manner. However, it is very often observed that during the stable pore growth, the current density continues to decrease slightly. This is due to diffusion limits in the long pore channels [3,4].

In the case of the formation of porous films, the following current density profiles are typically observed [3-7]. First, the current density j_p decreases rapidly (regime 1 in Figure 1.2). Then, it passes through minimum value (regime 2 in Figure 1.2). It increases to arrive at a maximum value (regime 3 in Figure 1.2). Subsequently, it slightly decreases again. Finally, a steady current density remains (regime 4 in Figure 1.2). One can consider the current density j_p as the sum of j_b

and hypothetical current density j_{hp} , which means the pure current density for creating pores. j_b is determined by the applied potential in terms of the anodizing ratio, while j_{hp} depends on the electrolyte and the temperature as well as on the applied potential.

1.1.2. Electrodeposition

Electrodeposition is a process that uses electrical current to reduce dissolved metal cations so that they form a coherent metal coating on an electrode. The term is also used for electrical oxidation of anions onto a solid substrate, as in the formation silver chloride on silver wire to make silver/silver-chloride electrodes. Electroplating is primarily used to change the surface properties of an object (e.g. abrasion and wear resistance, corrosion protection, lubricity, aesthetic qualities, etc.), but may also be used to build up thickness on undersized parts or to form objects by electroforming. The anode is made of the metal to be plated on the part. Both components are immersed in a solution called an electrolyte containing one or more dissolved metal salts as well as other ions that permit the flow of electricity. A power supply supplies a direct current to the anode, oxidizing the metal atoms that comprise it and allowing them to dissolve in the solution. At the cathode, the dissolved metal ions in the electrolyte solution are reduced at the interface between the solution and the cathode. [8]

The anode and cathode in the electroplating cell are both connected to an

external supply of direct current — a battery or, more commonly, a rectifier. The anode is connected to the positive terminal of the supply, and the cathode (article to be plated) is connected to the negative terminal. When the external power supply is switched on, the metal at the anode is oxidized from the zero valence state to form cations with a positive charge. [8]

Recently, electrodeposition process can easily create a 3D dendritic structure of metals. This method is simple but effective way to involve electrochemical deposition accompanying with hydrogen bubble generation. In this process, hydrogen bubble plays an important role as a dynamic negative template in the formation of the porous structure. The final products are three-dimensional free-standing foams of metals with highly porous dendritic walls. [9]

1.2 Semiconductor gas sensor

1.2.1. Working mechanism

The electrical conductivity and resistance of semiconductor materials such as SnO_2 , TiO_2 are changed by the adsorption/desorption of gas molecules on semiconductor materials surface. This phenomenon is occurred due to electric band-bending on surface. The sensing mechanism of SnO_2 toward CO gas is shown in Figure 1.3. [10] The SnO_2 crystals id n-type semiconductor materials having oxygen lattice defect as an electron donor. The oxygen defects (oxygen vacancy) in SnO_2 crystal are activated by increasing temperature and its mobility

increased. The adsorbed oxygen molecules on surface obtain electron from semiconductor materials and those adsorbed oxygen molecules on surface are negatively charged. This causes that the potential difference between surface and inside leads to the formation of space charge layer and potential barriers are formed between grains. (Figure 1.3(a)). When reduction gas such as CO flow to SnO₂, the adsorbed oxygen on SnO₂ surface react with CO therefore CO is oxidized to CO₂ and generated electrons flow into SnO₂, resulting electrical resistance decrease. (Figure 1.3(b)). On contrary, when oxidation gas such as NO_x flow to SnO₂, the number of adsorbed oxygen on SnO₂ surface increase therefore more electrons flow out from SnO₂ resulting electrical resistance increase. (Figure 1.3(c)) In this manner, the concentration of reduction/oxidation gas is proportional to the variation of electrical resistance and this electrical signal lead to gas detection.

The semiconductor-type gas sensing performance is evaluated in terms of sensitivity, selectivity, response time, reproducibility and stability.

Sensitivity is the variation of electrical resistance on exposure to target gases and this is expressed as.

$$S = \frac{R_a}{R_s}$$

From this equation, sensitivity is defined to the ratio of resistance in air to resistance in gas. The sensitivity is critical factor on gas sensing performance and,

in order to enhance gas sensing sensitivity, many efforts are underway to develop surface modification, heterostructuring, catalyst loading and so on.

Selectivity is defined to the sensing performance to detect specific target gas among various gases in atmosphere. When gas sensor is exposure to two kind of A and B gases at the same time, the selectivity of gas sensor toward B gas is expressed as.

$$Se = \frac{S(A)}{S(B)}$$

In this equation, S(A) and S(B) mean the sensitivity toward A and B gas each. Most metal oxide gas sensors tend to react to various gases therefore those selectivity is not good enough generally.

Response time is the time to drop to the resistance value in target gas from the stabilized resistance value in air. Therefore, the shorter response time means the faster reaction with gas and response time is considered as a critical factor to evaluate gas sensing performance. Most semiconductor gas sensor show very short response time within tens of seconds and it is reported that catalyst loading is effective way to shorten response time. [11,12]

Reproducibility and stability is a main hindrance for the practical implementation of semiconductor-type gas sensor. After a number of gas sensing test, sensing behavior should be consistent and reproducible. Generally, impurity humidity in air has adverse effect on reproducibility therefore heat treatment in

high temperature is considered as an effective way to stabilize phase and obtain stable gas sensing behavior [13]

1.1.2. SnO₂ gas sensor

The band diagram in case of O₂ molecules absorbed SnO₂ is shown in Figure 1.4. When O₂ molecule adsorb on the surface of SnO₂, new energy level is formed between Fermi level (E_f) and valance band (E_v) (Figure 1.4 (a)) and electrons re-distribution occurs from conduction band of SnO₂ to O₂ molecules due to lower energy level than Fermi level (E_f). After then, O₂ molecules is converted to O₂⁻ or O⁻ as obtaining electrons and the decreased electrons on the SnO₂ surface result in electronic field formation inside of SnO₂ due to positively charged donor. The intensity of electric field increase as the number of moved electrons increase and the electric field with high intensity prevent electron from moving to O₂ molecules. At the steady state, the Fermi level of SnO₂ surface is same as energy level of O₂ electrons and there is no electron movement. (Figure 1.4 (b)). In Figure 1.4 (c) the valance band, conduction band and donor level are bent upward in band structure and the length of band bending is depletion layer, called as Debye length (approximate 3nm in SnO₂)

1.3 Lithium-ion battery

Lithium-ion batteries are a type of rechargeable battery in which a lithium ion

moves between the anode and cathode. The lithium ion moves from the anode to the cathode during discharge and from the cathode to the anode when charging. They are currently one of the most popular types of battery for portable electronics, with one of the best energy-to-weight ratios, no memory effect, and a slow loss of charge when not in use. In addition to uses for consumer electronics, lithium-ion batteries are growing in popularity for defense, automotive, and aerospace applications due to their high energy density.

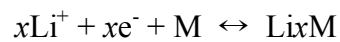
1.3.1. Reaction mechanism

The secondary batteries should have the system for repeated charge/discharge behavior. For this, easy insertion/exertion of metal-ion in electrode, structural stability during reaction and fast ion mobility in electrolyte are important factors to decide battery properties. In secondary battery systems, the metal ion inserted in electrode form charge neutrality with electrons passed to current collector and then the metal ions inserted in electrode play a role as an energy storage media.(Figure 1.5) [14] In addition, the reaction rate in system can be improved as metal ion can fast move toward electrode in electrolyte therefore the overall reaction rate in LIBs is determined by metal-ion mobility in electrolyte and electrode. In terms of capacity, the amount of inserted metal-ion in electrode for achieving charge neutrality determines energy storage capacity. In this manner, the kind of metal ion and electrode materials is a crucible factors on secondary

batteries performance and the Li-ion used battery is called lithium secondary batteries. In case of positive electrode materials, stable metal oxide is mainly used because lithium-ion exerts from the lattice structure of cathode materials. In case of negative electrode materials, the materials having similar standard redox potential with Li-ion is adapted in order to produce large potential and store stably the metal ion from positive electrode

1.3.2. SnO₂-based anode materials

The metal ion enabling to alloy with lithium ion is candidate as a anode (negative electrode) materials. This Li-M alloy is produced at specific potential during charge reaction and the lithium-ion is exerted from Li-M alloy during discharge reaction.



While Li-ion intercalation/deintercalation reaction is shown in commercially used graphite-base anode materials, the reversible alloying reaction is observed in other materials such as Si, Sn, Ge, Sb and so on. (Figure 1.6) [15]

Among the various interesting anode candidates, tin (Sn) has recently received considerable attention as a result of its high theoretical specific capacity (994 mAh g⁻¹), according to Li₂₂Sn₅[16]. Moreover, several Sn-based materials, such as tin dioxide (SnO₂)[10], tin disulfide (SnS₂)[11], tin diselenide (SnSe₂)[12], and intermetallic compounds (such as nickel (Ni-Sn)[13] and copper (Cu-Sn)[14])

have been suggested as well, all of which exhibit much higher capacity than the commercialized graphite anodes ($\sim 372 \text{ mAh g}^{-1}$). Although its cheap and abundant nature makes tin an attractive candidate, the application of tin as an anode is still far from commercialization. One of the critical issues is that these Sn-based anode materials commonly suffer from severe capacity fading during the insertion and extraction of lithium ions, which mainly results from the pulverization of active materials caused by the huge volume change of tin upon cycling. Therefore, elaborately tailoring the structure of Sn-based materials to effectively accommodate the volume expansion is one of the critical issues towards solving this problem.

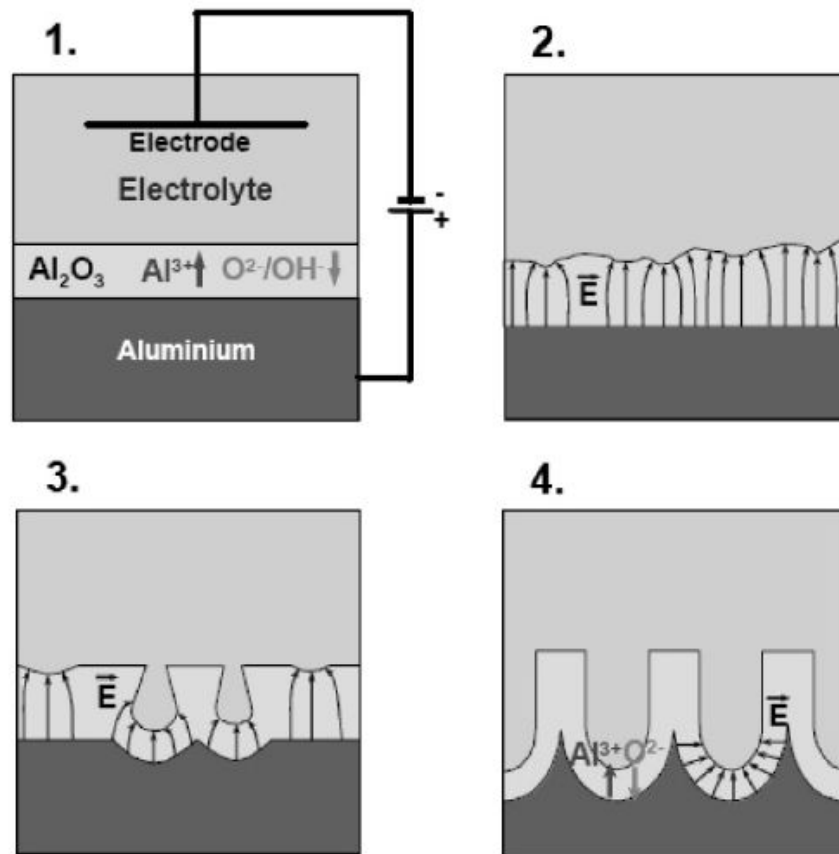


Figure 1.1 The pore formation at the beginning of the anodization. Regime 1: formation of barrier oxide on the entire area; regime 2: local field distributions caused by the surface fluctuations; regime 3: creation of pores by field-enhanced or/and temperature-enhanced dissolution; regime 4: stable pore growth

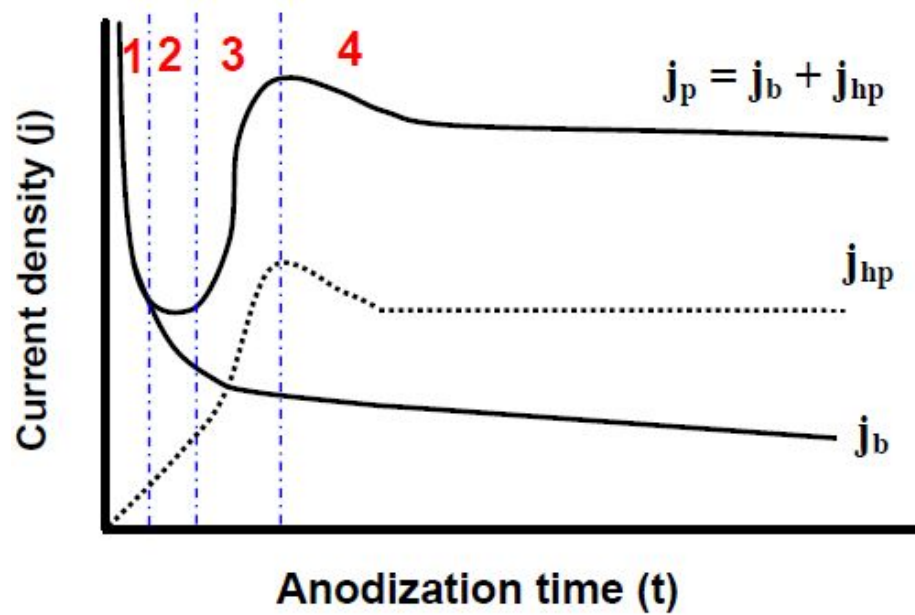


Figure 1.2 Schematic diagram of current density curve during the initial growth ($< 1h$) at constant voltage. j_b and j_p indicate the current density for the barrier film and the porous film formation, respectively. j_{hp} represents a hypothetical current density, which is the difference between j_p and j_b .

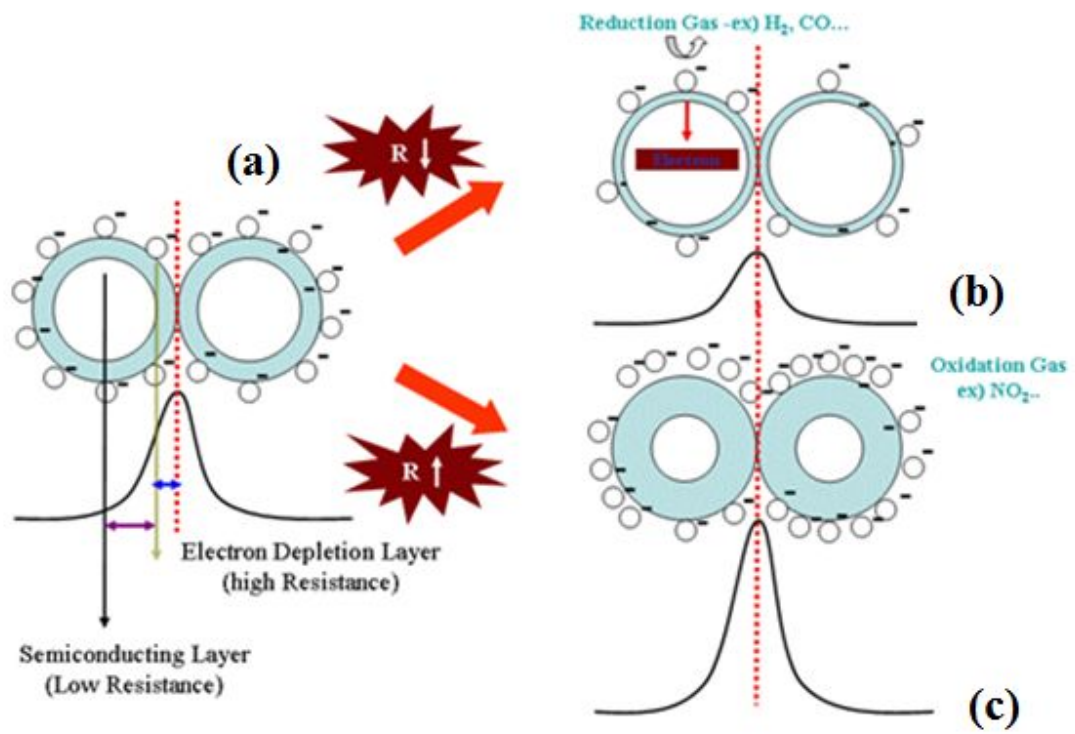


Figure 1.3 The mechanism of CO gas sensing in SnO_2 gas sensor

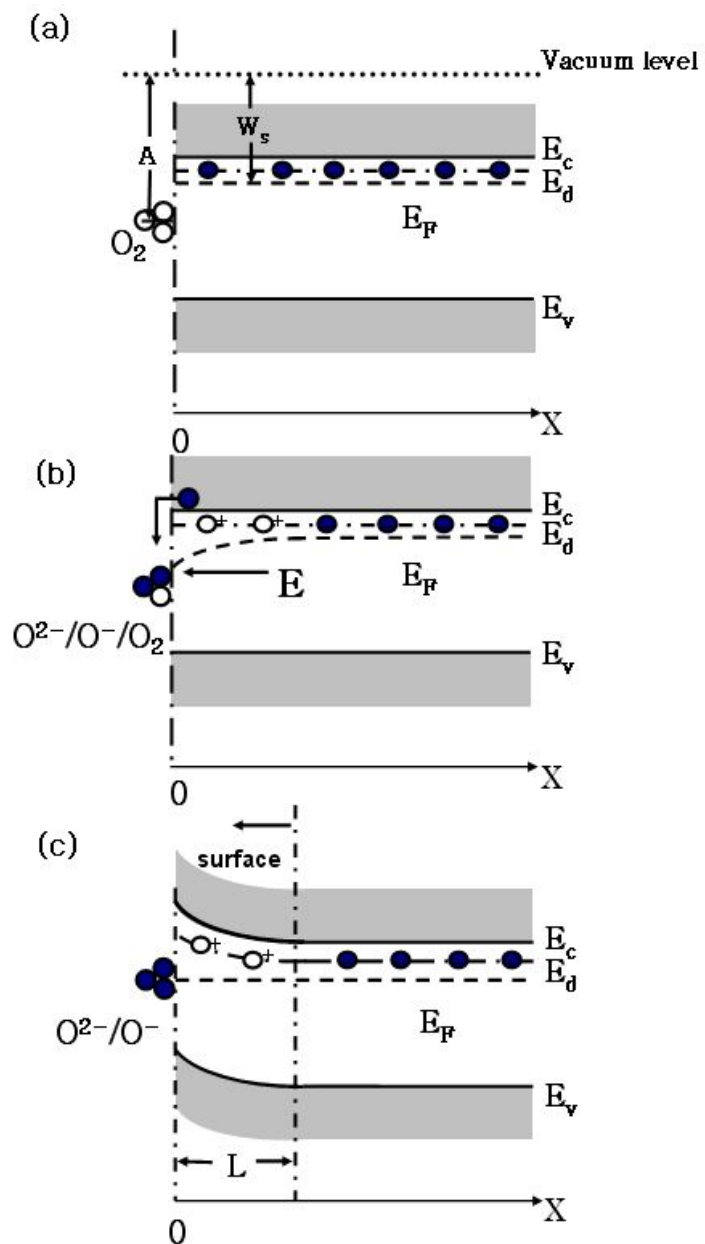


Figure 1.4 Band diagram of O_2 adsorption on the surface of n-type semiconductor SnO_2

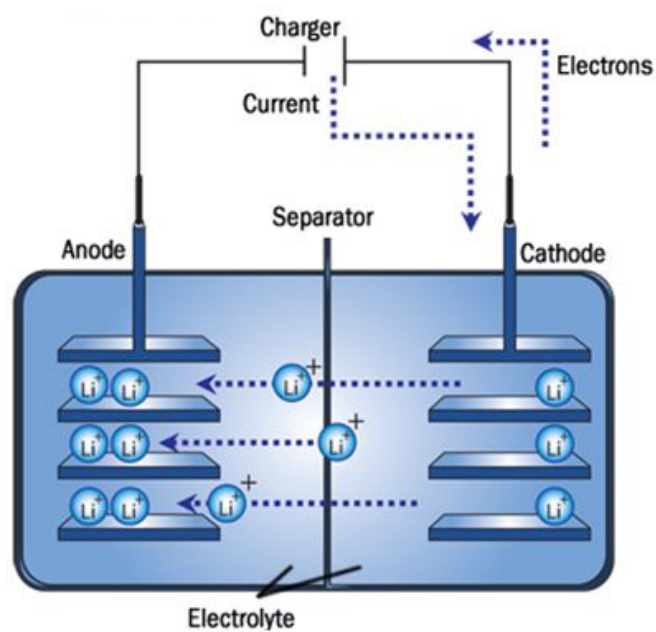


Figure 1.5 Lithium-ion rechargeable battery mechanisms

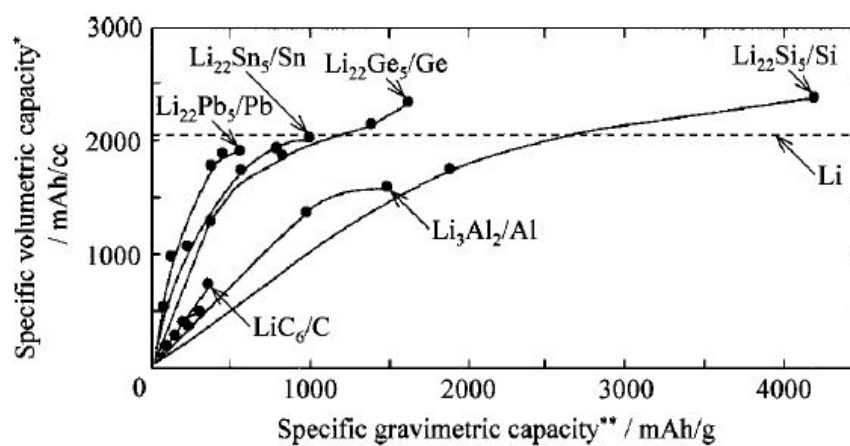


Figure 1.6 The specific capacity of group IV elements

1.4. Reference

1. V. P. Parkhutik and V. I. Shershulsky, *Journal of Physics D - Applied Physics*, 25 (1992) 1258.
2. B. Vanderlinden, H. Terryn, and J. Vereecken, *Journal of Applied Electrochemistry*, 20 (1990) 798.
3. K. Nielsch, "Hochgeordnete ferromagnetische Nano-Stabensembles: Elektrochemische Herstellung und magnetische Charakterisierung," Martin-Luther-Universität Halle-Wittenberg, 2002.
4. R. B. Wehrspohn and A. P. Li, K. Nielsch and F. Müller and W. Erfurth and U. Gösele(editors: K. R. Hebert and R. S. Lillard and B. R. MacDougall), Highly ordered alumina films: pore growth and applications (Oxide Films in The Electrochemical Society Proceeding Series), vol. PV 2000-4, pp. 271. Pennington, NJ: Marcel Dekker, 2000.
5. J. W. Diggle, T. C. Downie, and C. W. Couding, *Chemical Review*, 69 (1969) 365.
6. F. Li, "Nanostructure of anodic porous alumina films of interest in magnetic recording," The University of Alabama, 1998.

7. O. Jessensky, "Untersuchungen zum Porenwachstum in 6H-Siliziumkarbid und anodischem Aluminiumoxid," Martin-Luther-Universität at Halle-Wittenberg, 1997.
8. M. Stelter, H. Bombach, *Advanced Engineering Materials*, 6 (2004) 558
9. H.C Shin, J. Dong, M. Liu, *Advanced materials*, 15 (2003) 1610
10. J.H Lee, *Ceramist*, 8(2005) 45-53
11. R. K. Sharma, M. C. Bhatnagar, *Sensors and Actuators B* 56 (1999) 215.
12. Z. Jing, *Mater. Lett.*, 60 (2006) 3315.
13. N. Yamazoe, Y. Kurokawa, T. Seiyama, *Sensors and Actuators* 4 (1983) 283.
14. <http://electronics.howstuffworks.com/everyday-tech/lithium-ion-battery1.htm>
15. Noriyuki Tamura, z Ryuji Ohshita, Masahisa Fujimoto, Maruo Kamino, and Shin Fujitani, *Journal of The Electrochemical Society*, 150 (2003) A679.
16. M. Winter, J.O. Besenhard, M.E. Spahr, P. Novak, *Adv. Mater.* 10 (1998) 725.
17. I. Mochida, S.H Yoon, Y. Korai, K. Kanno, Y. Sakai, M. Komatsu, H. Marsh, F. Rodriguez-Reinoso, *Science of Carbon Materials*, Alicante, Spain: Publicaciones de la Universidad de Alicante (2000)
18. S. Otani, *Carbon* 3 (1965) 31

19. R.J Nemanich, S.A. Solin, *Phys. Rev. B* 20 (1979) 392.
20. S. Mathew, B. Joseph, B.R. Sekhar, B.B. Dev, *Nuclear Instruments and Methods in Physics Research Section B* 266 (2008) 3241
21. American institute of physics, *J. Chem. Phys.* 53 (1970) 1126

Chapter 2.

Synthesis of porous SnO₂ based Nanostructures for Gas Sensing Application

2.1. Introduction

Tin oxide (SnO_2) is a well-known semiconductor-type gas sensor material detecting inflammable and toxic gases.[1] The gas adsorption/desorption on the surface of sensor material changes its electric resistivity, which strongly depends on the thickness of depletion layer.[2-5] The surface area is one of the key factors to determine the gas sensing performance such as sensitivity, selectivity, and response-recovery time. Various SnO_2 nanostructures including nanotubes,[6] nanoribbons,[7] nanodiskettes,[8] and nanowires[9] were fabricated and applied to gas sensors because the high surface-to-volume ratio of nanostructures makes their electrical responses extremely sensitive to the species adsorbed on the surface.

In particular, it is widely accepted that nano-porous structure show great promise for gas sensor and the mechanism of gas diffusion for porous body to gas sensing characteristic has been clarified. Therefore, in order to apply it to gas sensor, a tremendous effort has been paid to synthesis a nano-sized porous structure on various ways such as sol-gel process[10], membrane[11], spray pyrolysis[12] and so on. However, little attention has been paid to the 1-D nano-porous SnO_2 structure compared to the other porous structures.[13-15] The self-ordered nano-porous structure is commonly fabricated by anodization and electrodeposition, which is a relatively simple, low cost, and high yield

electrochemical process.[16,17] These methods were successfully applied to several metals to develop the highly ordered porous oxide structures.[16-20] In case of anodization, the porous tin oxide has been fabricated using tin (Sn) foil,[21] but there was an unreacted tin left after anodizing and the integrity and pore structure of anodic oxide were collapsed during the subsequent annealing process because SnO_2 crystallization temperature is higher than Sn melting point ($T_m, \text{Sn}=250^\circ\text{C}$). In case of electrodeposition, the synthesis of 3-D porous metal oxides using this technique has not been explored because the metal cathode was also oxidized during the heat treatment for crystallization even though this facile and effective deposition technique has been applied to the various metals and alloys. [22-29]

To overcome these problems in both process, Sn film was deposited on the SiO_2/Si substrate by thermal evaporation and then electrochemical process was followed. In anodic oxidation process, the developed amorphous nano-porous anodic oxide was converted into crystalline SnO_2 film by subsequent annealing. In electrodeposition process, The porous Sn foam structure was successfully fabricated using this technique and it was converted into the SnO_2 foam after heat treatment without deteriorating the structural integrity and pore structure of metal foam. Gas sensor was fabricated using Pt-pattern on SnO_2 product and its gas sensing properties were investigated.

In addition, in order to give functionality on enhancing sensing selectivity toward H_2S , the formation of pn junction using heterostructure with CuO is applied. Hydrogen sulfide (H_2S) is one of the toxic and inflammable gases and the threshold for human tolerance is reported to be 20 ppb. There are continued efforts to detect the trace amount of H_2S through better design of new materials and innovative structures and architectures. CuO/ SnO_2 hybrid is recognized as one of the promising materials for the sensitive and selective detection of H_2S because the electric signals can be amplified using the establishment of resistive p-CuO/n- SnO_2 junction. Herein, SnO_2 /CuO porous structure was synthesized using impregnation methods after anodization process and co-electrodeposition each and its sensing mechanism were investigated.

2.2 Synthesis of Nanoporous SnO_2 via anodic oxidation and its gas sensing properties

2.2.1. Experimental procedure

Preparation of Sn thin film on Si/ SiO_2 substrate: $\text{SiO}_2(2\mu\text{m})/\text{Si}(100)$ substrates were cut into a 20 x 10 mm rectangular shape and then rinsed with acetone, ethanol, and distilled water, successively. SnO_2 thin films were deposited on both

substrates by an atomic layer deposition (ALD) using dibutyltin diacetate (DBTDA) as a Sn precursor. The time sequence for source pulse, first purge, oxygen pulse, plasma pulse, and second purge was 3, 12, 2, 10, and 12 s, respectively. The substrate temperature was maintained at 100 °C and the deposition was conducted for 300 cycles. Sn metal films were coated on SnO₂ films by a thermal evaporation. The tin shot (Kojundo Chemical, 99.999%) was used as a metal source for the thermal evaporation (MHS-1800). The tin shot (Kojundo Chemical, 99.999%) was used as a metal source. During thermal evaporation, the substrate temperature was maintained in the range of 70~100°C and the deposition was performed at the rate of 15 Å/s.

Anodic oxidation and Annealing: The anodic oxidation was performed in the electrolyte solution of 0.3 M oxalic acid (Sigma Aldrich, 99.8%) at 5°C for 90 s without stirring or N₂ bubbling. The constant voltage of 6 V was applied between working electrode and counter electrode (carbon plate) using a DC power supply (Fine-Power, F-100). All the anodic films were annealed in the range of 500~700°C for 1 h to enhance the crystallinity.

Analysis: The surface morphology and cross-section image of the films were examined by field emission scanning electron microscope (FESEM, JSM-7401F) and transmission electron microscope (TEM, JEM1010). The phases of the films were determined by X-ray diffraction (XRD, M18XHF-SRA) and X-ray

photoelectron spectroscopy (XPS, Model AXIS, KRATOS) with a Mg K-alpha radiation (1253.6 eV).

Gas sensing measurement: For the gas sensing measurements, a pair of comb-like Pt electrodes was formed on the porous SnO₂ films through a mask by sputtering. The gap between Pt electrodes was 0.2 mm and the width was 8 mm. Thereafter, Au lead wires were attached to them using a silver paste. All the sensors were annealed at 600°C for 1 h in air atmosphere in order to make the electrical contact between silver paste and Au lead wires. The sensor element was placed in a quartz tube located inside a tube furnace with gas inlet and outlet. The H₂, CO, and NH₃ gas sensing properties were determined by measuring the changes of electrical resistance between sample gas and reference gas (pure air) at temperatures from 200 to 500°C. The electrical resistance was measured using a multimeter (2000 multimeter, Keithley). In this study, the magnitude of gas response (S, sensitivity) was defined as the ratio (R_a/R_g) of the resistance in air (R_a) to resistance in sample gas (R_g). The response time ($t_{90\%}$) was defined as the time required for the sensor to reach 90% of the final signal. For comparison, the as-deposited Sn film was thermally oxidized at 700°C for 1 h at the heating rate of 1°C/min without anodizing step, and then, fabricated into a gas sensor in the same procedures as above. Another sensor was also fabricated using a commercially available SnO₂ powder (~325 mesh, Sigma Aldrich).

2.2.2. Results and discussion

Synthesis of nanoporous SnO₂ structure

The as-deposited Sn films were polycrystalline and the grain size was ~300 nm (Fig. 2.2.1(a)). The thickness of as-deposited films was ~400 nm with a columnar structure (Fig.2.2.1(b)). For anodic oxidation, the electrolyte concentration, applied voltage, reaction temperature, and anodizing time were optimized to achieve a good adhesion between anodic oxide and substrate with a nano-porous structure (0.3 M, 6 V, 5 °C, and 90 s, respectively). In this condition, the determined current density-time transient was a porous type film as shown in Fig.2.2.2. In order to investigate the growth of anodic tin oxide layer, the morphological changes in cross-sectional view is shown in Fig 2.2.3 according to the variation of anodizing time. The porous layer is grown and the thickness of tin metal layer decrease as anodic oxidation time increase. The nano-pores were not observed on the bare surface however, from the partially stripped surface, randomly distributed nano-sized pores of 50~80 nm could be seen indicating that nano-sized pores were closed. The nano-pores were not observed on the bare surface, but randomly distributed nano-sized pores of 50~80 nm could be seen from the partially stripped surface. From the cross sectional view (Fig. 2.2.3(d)), a relatively dense layer of 50~100 nm thick was found on the top of the film and the rest of anodic oxide was composed of the discrete vertical nano-channels, which

were disconnected by the parallel micron-sized pores. The top dense layer was formed at the early stage and existed persistently during anodizing as shown. It is believed that this layer is a barrier oxide, which is not so compact that the electrolyte penetrates and the anodic reaction occurs continuously underneath the barrier layer forming the nano-porous layer. The porous layer was composed of hundred nanometer-sized stacked layers separated by discontinuous gaps (or pores), which has been attributed to the vigorous gas evolution and faster oxide growth rate than that of anodic aluminum oxide [30,31].

The changes of surface morphology as increasing anodizing temperature were shown in Fig. 2.2.4. The tendency to create crack and dissolve tin increase as anodic oxidation temperature increase and the more porous inner layer is generated as the higher temperature is employed. More severe anodic conditions (high electrolyte concentration, high reaction temperature) have been applied to remove the top dense layer, but it was not successful except generating the micron-sized pin holes on the surface and deteriorating the film adhesion.

After annealing at 700°C for 1 h, the smooth surface of as-anodized films changed into the porous granular surface (Figure 2.2.5(a)). It appears that the top-most layer coalesced into the discrete spherical grains of ~40 nm during heat treatment. However, the microscopic features of the nano-sized pores and vertical nano-channels were still conserved after annealing indicating a high thermal stability of anodized films (Figure 2.2.5). The TEM micrograph clearly showed

the porous structure with irregular pore shapes (Figure 2.2.6). The channel diameter was ~ 50 nm and the wall thickness was ~ 20 nm. The surface area of scratched anodic films, determined by nitrogen absorption (BET), was $72 \text{ m}^2/\text{g}$. XRD pattern showed that as-deposited film by thermal evaporation was crystalline tin (Sn) and strongly (100) oriented (Figure 2.2.7(a)). Only Sn peak with low intensity was observed in the as-anodized film (Figure 2.2.7(b)) implying that amorphous anodic oxide was formed. The anodic oxidation could not be conducted completely due to the film adhesion and the presence of Sn can be attributed to the unreacted Sn close to the substrate. Based on the dark brown color and previous report,[32,33] the anodic oxide appears to be stannous oxide (SnO). The amorphous anodic oxide was partially crystallized at 500°C and fully transformed into crystalline SnO_2 at 700°C (Figure 2.2.7(c) and (d)). For the further phase analysis, XPS analysis was conducted shown in Figure 2.2.8. The binding energy of anodic tin oxide is corresponding to that of rutile SnO_2 and it means that the phase of as-anodized specimen was amorphous tin oxide with chemical stoichiometry ratio of 1(tin):2(oxygen) from both XRD pattern and XPS data. (Figure 2.2.7 and 2.2.8)

Gas sensing properties

A typical response transient of the nanoporous SnO_2 film sensor toward H_2 gas balanced with air measured at 400°C is shown in Figure 2.2.9. Upon injecting

a target gas, the resistance rapidly decreased by more than an order of magnitude. The recovery was slightly slow, but the sensing signal was quite stable and reversible even after switching the gases several times. The magnitude of the gas response (S) was estimated to be 52 toward 1.0% H_2 /air, which was substantially higher than that of the thermally oxidized film sensor ($S \sim 3$) and the commercial SnO_2 powder sensor ($S \sim 25$) and was comparable to that of the commercial sensor (FIS Inc.). The response time was ~ 3 s toward 1.0% H_2 /air and increased with decreasing H_2 concentration. (Figure 2.2.10)

The determined magnitude of gas response is shown in Figure 2.2.11 as a function of sensing temperature and H_2 concentration. The lowest operating temperature was 200°C due to a high resistance of the films and an equipment limitation (up to $\sim 10^8 \Omega$). The porous SnO_2 film sensor exhibited the highest gas response at 400°C , which is a typical characteristic of semiconductor-type gas sensors.^{3,20} The magnitude of the gas response increased almost linearly with increasing H_2 concentration from 200 to 10,000 ppm ($\log(\text{gas response})$ vs. $\log(\text{concentration})$).

The sensing properties of nano-porous SnO_2 film sensor toward NH_3 and CO gases were also investigated (Figure 2.2.12). The maximum gas responses for both gases were observed at 400°C similar to H_2 gas. The sensors reliably responded to NH_3 gas in the range of 20~200 ppm and to CO gas with a

fluctuation in the range of 100~1000 ppm. However, the magnitude of gas response for both gases was relatively lower, and thus the porous SnO₂ film sensors showed a high selectivity for H₂ against NH₃ or CO gas.

2.2.3. Conclusion

Nano-porous SnO₂ films with vertical nano-channels have been successfully prepared by anodic oxidation of Sn films on SiO₂/Si substrate deposited by thermal evaporation. Anodizing of Sn film in oxalic acid produced amorphous anodic oxide with nano-sized pores, and subsequent annealing at 700°C converted into crystalline SnO₂ with nano-channels of ~50 nm diameter maintaining a good adhesion to substrate. The Pt patterned nano-porous SnO₂ film sensor responded to H₂, NH₃, and CO gases and exhibited the highest gas response toward H₂.

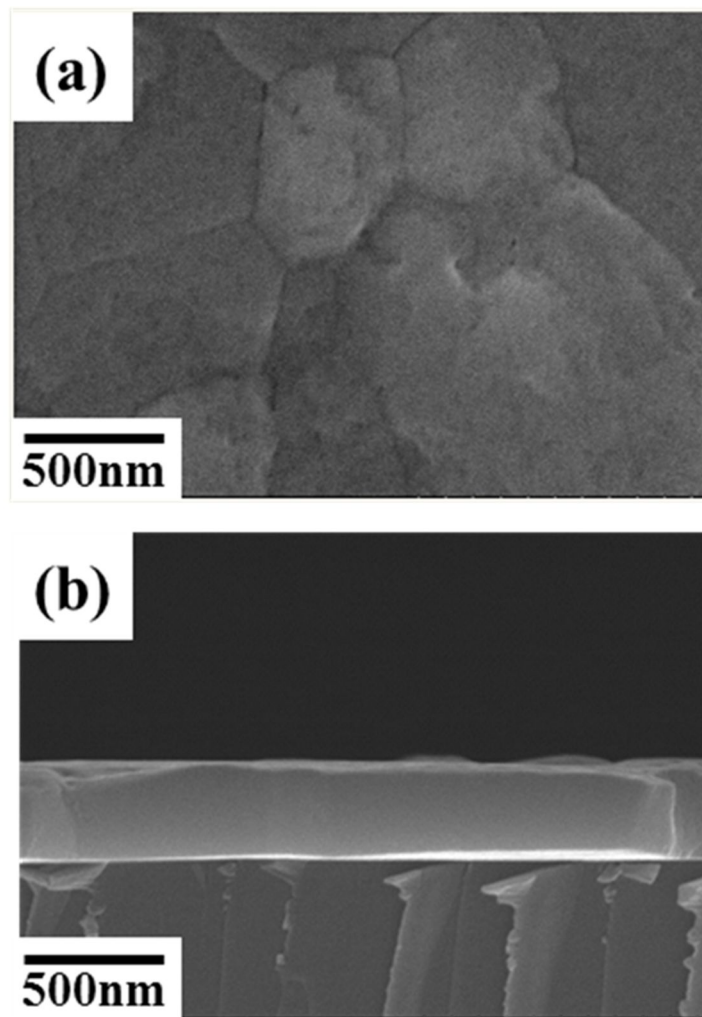


Figure 2.2.1 (a) Plain view of as-deposition Sn film on Si/SiO₂ substrate and (b) its cross-sectional view

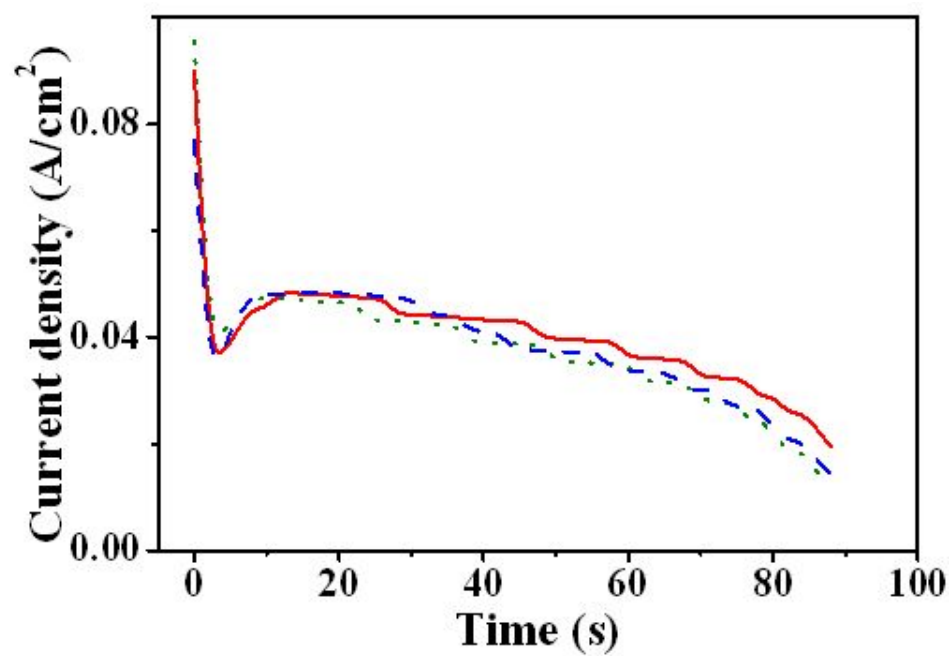


Figure 2.2.2 Current density-time transients at constant applied voltage of 6 V during anodizing of as-deposited Sn films.

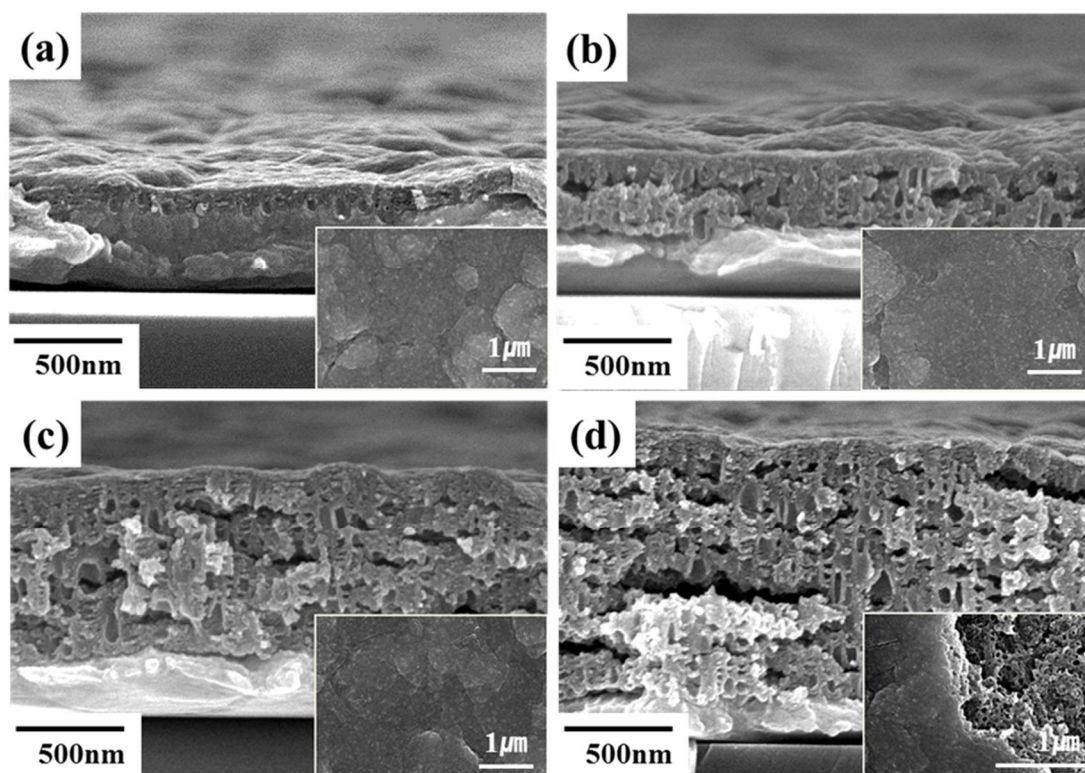


Figure 2.2.3 Plain and cross-sectional views of as-anodized films anodized at 50°C for (a) 15, (b) 30, (c) 60, and (d) 90 s.

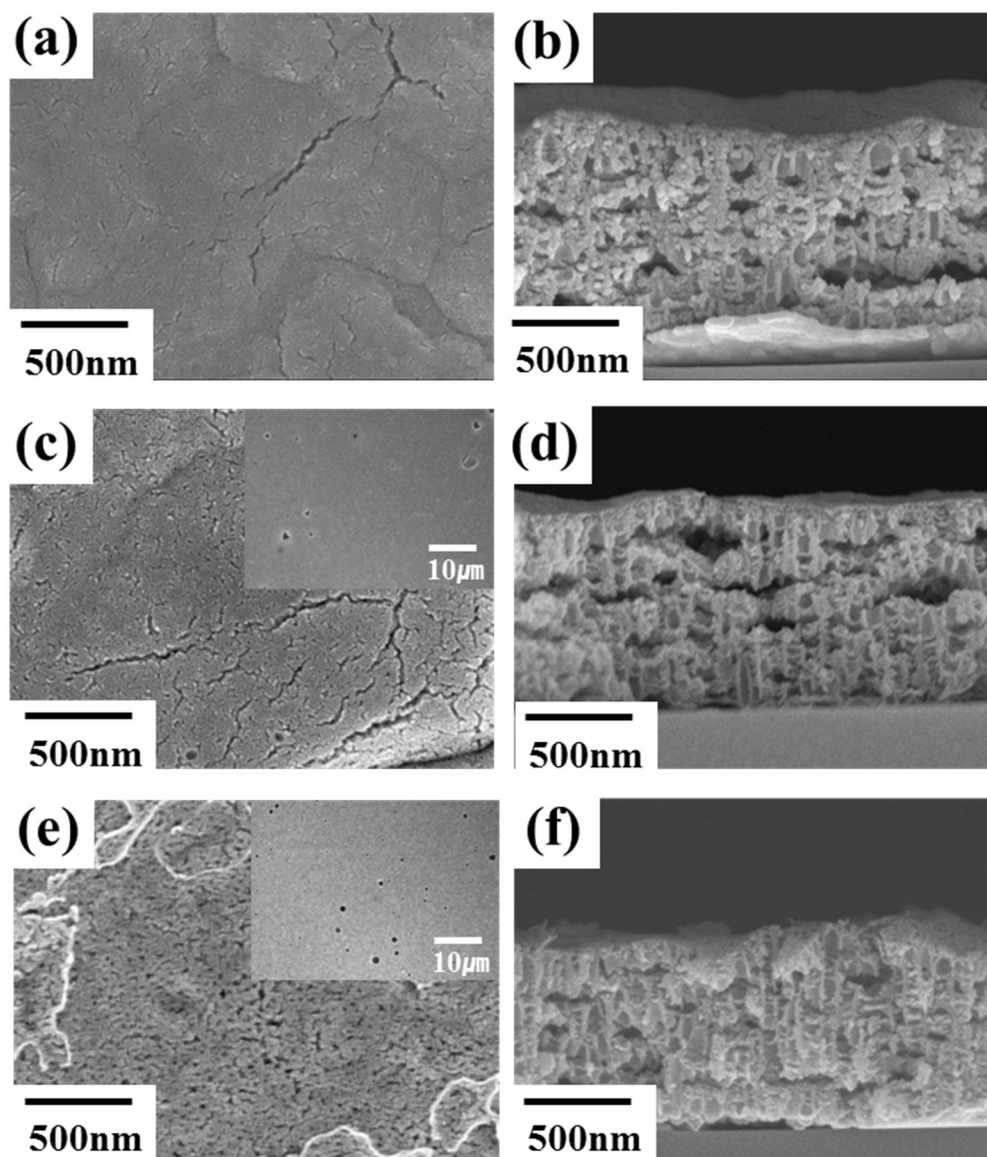


Figure 2.2.4 Plain and cross-sectional views of as-anodized films anodized for 15 sec at (a, b) 5, (c, d) 15, (e, f) 25 °C

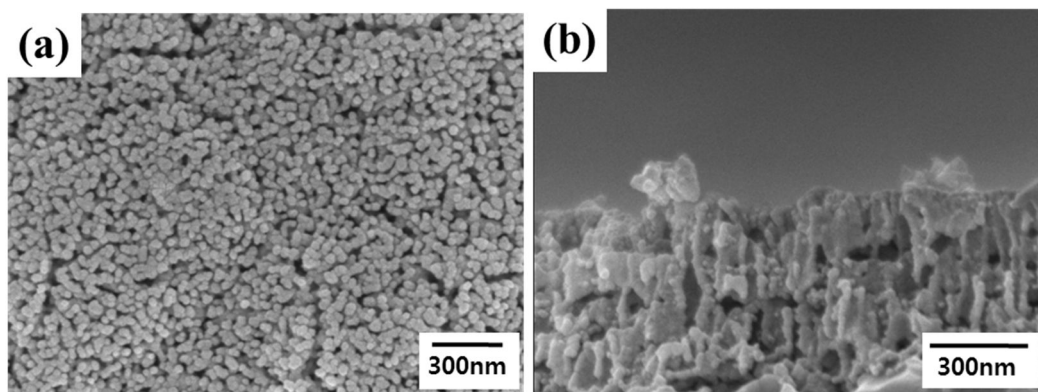


Figure 2.2.5 (a) Plain and (b) cross-sectional views of as-annealed films at 700°C for 1h

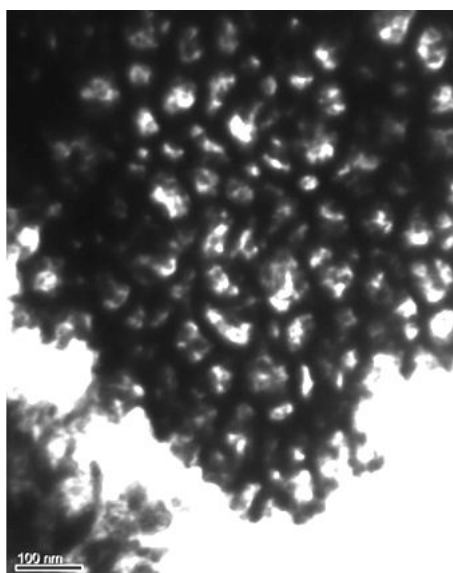


Figure 2.2.6 TEM image of as-annealed films

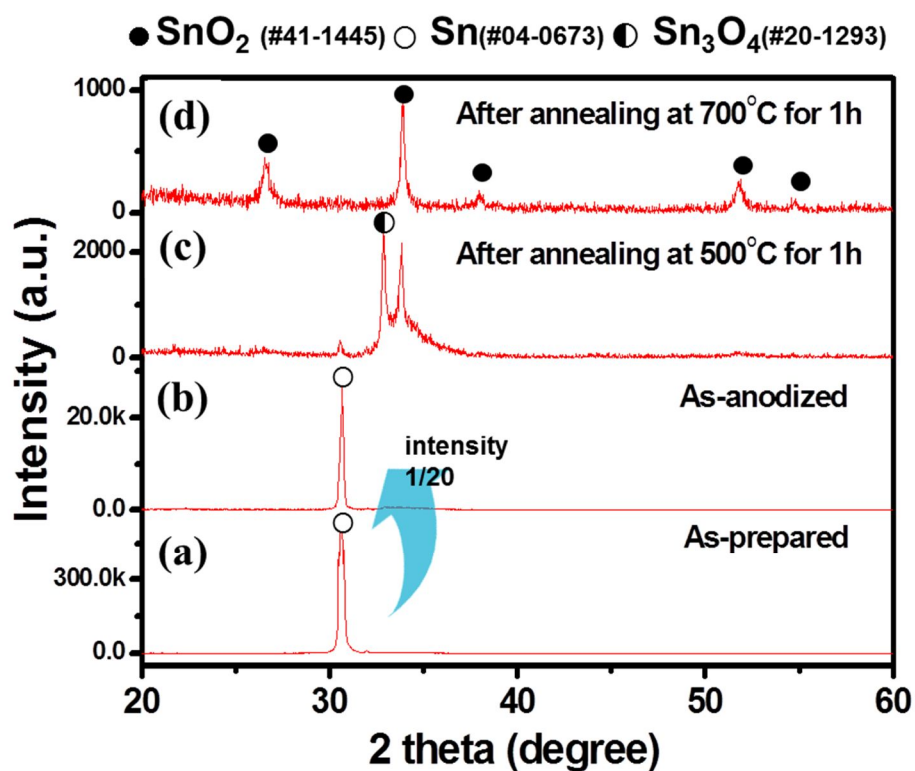


Figure 2.2.7 X-ray diffraction pattern of (a) as-prepared Sn film, (b) as-anodized film, (c) as-annealed film at 500°C for 1h, (d) as-annealed film at 700°C for 1h

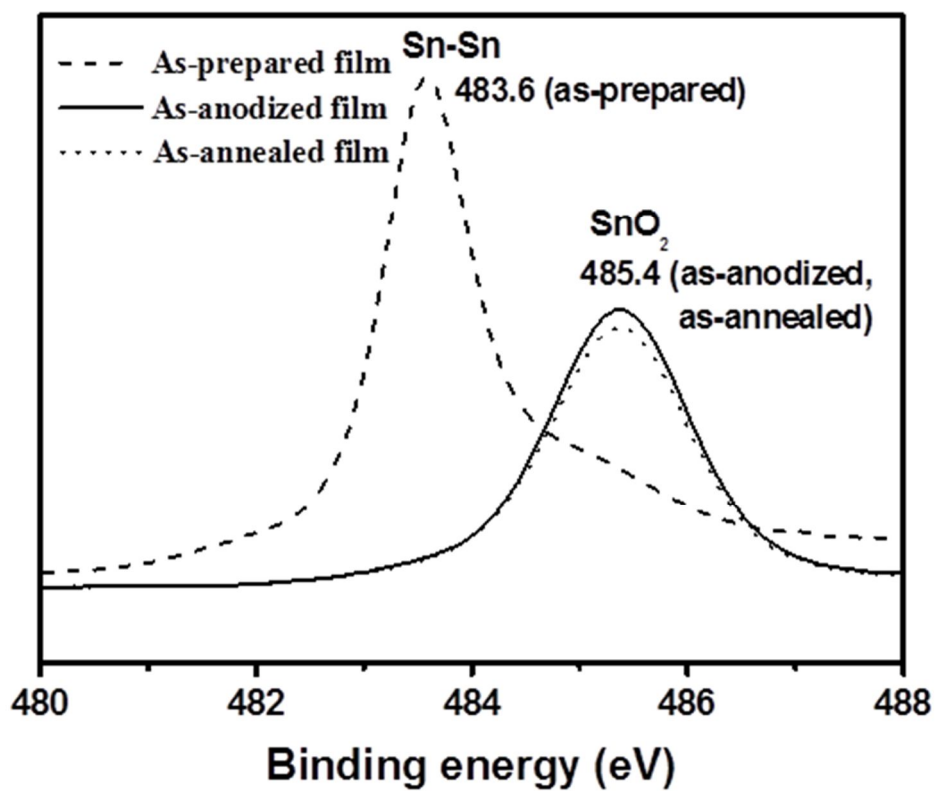


Figure 2.2.8 XPS spectra of as-prepared Sn film (dash line), as-anodized film (solid line) and as-annealed film (dot line)

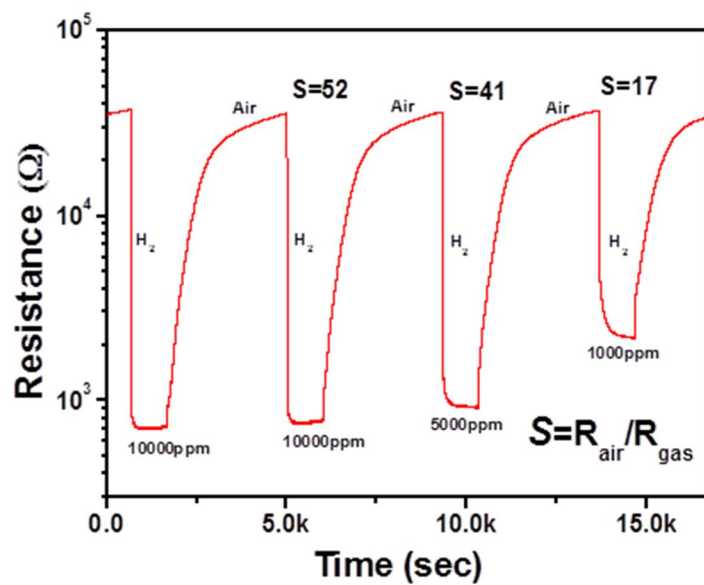


Figure 2.2.9 Gas sensing transient of nanoporous SnO₂ film at 400°C

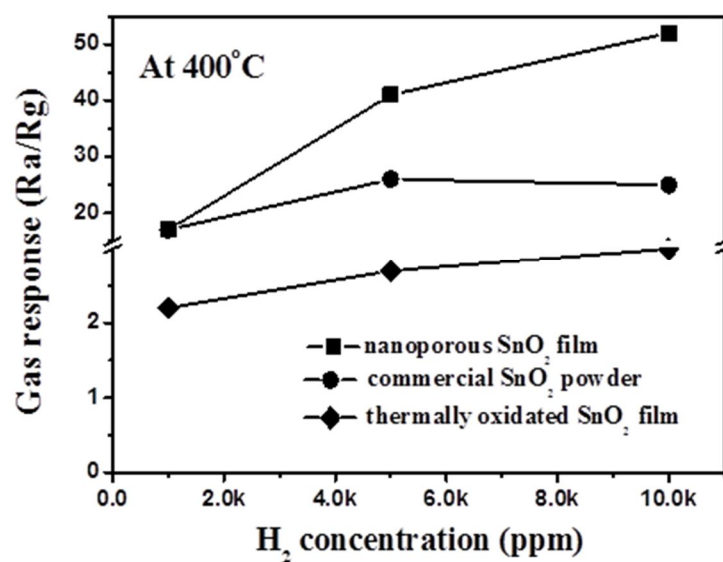


Figure 2.2.10 Gas response of nanoporous SnO₂ film at 400°C

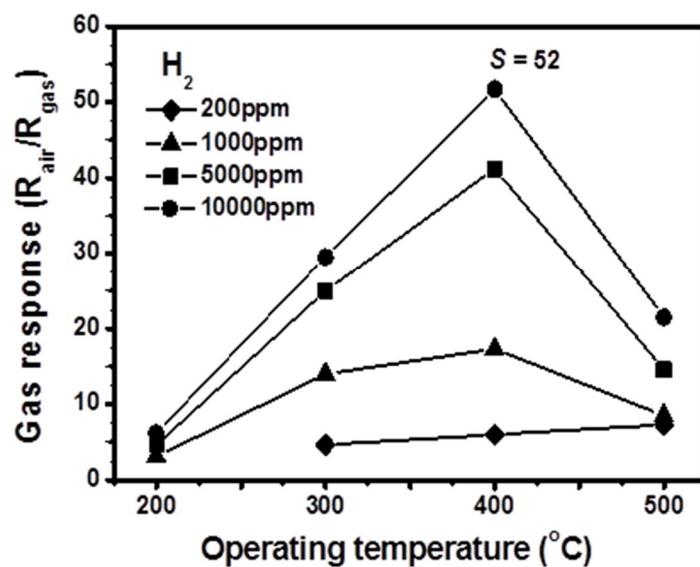


Figure 2.2.11 Gas response of nanoporous SnO₂ according to operating temperature and H₂ concentration

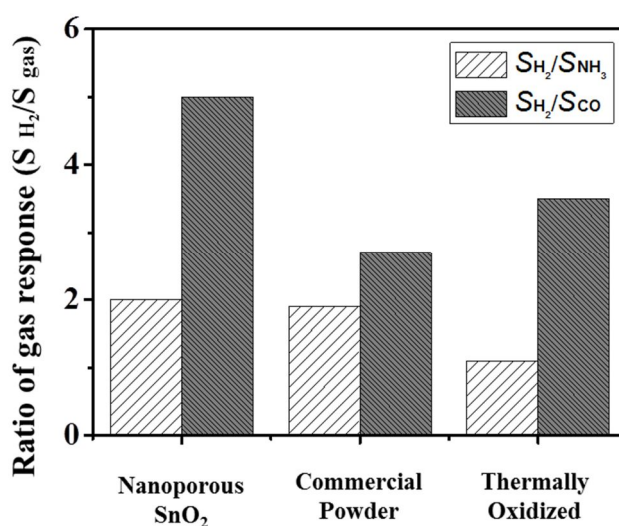


Figure 2.2.12 Gas response of nanoporous SnO₂ commercial SnO₂ powder, thermally oxidized SnO₂ sensor toward NH₃ and CO gases

2.3 Nanoporous SnO₂/CuO via anodic oxidation and reactive ion etching and its gas sensing mechanism

2.3.1. Experimental procedure

Nano-porous SnO₂ films were prepared by an anodic oxidation of Sn thin films deposited on SiO₂/Si substrates using a thermal evaporation and detailed experimental conditions for Sn coating and anodizing were shown in 2.2.1.

Reactive-ion etching process: A reactive ion etching (RIE) was employed to remove the non-porous barrier layer of SnO₂ anodic films and to widen the pore diameter. The etching was carried out in fluorocarbon-oxygen (CF₄-O₂) plasma with a power of 100 W for 5~10 min. The O₂ flow rate was fixed at 27 sccm and the CF₄ flow rate was varied from 10 to 30 sccm.

Impregnation process: Subsequently, as-etched nano-porous SnO₂ films were annealed at 700 °C for 1 h for crystallization. For CuO impregnation, a droplet of aqueous 0.01 M CuCl₂·2H₂O (99%, Kanto chemical) solution (0.5 ml) was dropped onto the as-annealed nano-porous SnO₂ film. After drying, the as-impregnated nano-porous SnO₂ films were heated at 600 °C for 1 h in order to transform the Cu-precursor to CuO.

Analysis: The surface and cross-sectional morphologies of the SnO₂ films were examined by field emission scanning electron microscopy (FESEM, S-4800, Hitachi) and transmission electron microscopy (TEM, JEM1010). The phases of the films were determined by X-ray diffraction (XRD, M18XHF-SRA). The chemical bonding information of the films was examined by X-ray photoelectron spectroscopy (XPS, Model AXIS, KRATOS) with a Mg K-alpha radiation (1253.6 eV). The core level XPS spectra for O1s, Sn3d, and Cu2p were measured, and energy calibration was achieved by setting the hydrocarbon C1s line at 284.6 eV.

Gas sensing measurements: A pair of Pt electrodes with 6 mm gap was formed by sputtering on the CuO-SnO₂ films through a mask and Au lead wires were attached to them using an Ag paste. Thereafter, all the sensors were fired at 600 °C for 1 h in order to make the electrical contact between Ag paste and Au lead wires. The sensor element was placed in a quartz tube located inside an electrical tube furnace with a gas inlet and outlet. A continuous flow-through measurement system was used, and the sample gases used were 0.2~100 ppm H₂S, 20~100 ppm H₂, 20~100 ppm CO, 20~100 ppm NH₃, and 20~100 ppm C₂H₅OH balanced with air. The gas sensing properties were determined by measuring the changes of electric resistance between sample gas and reference gas (pure air) at temperatures from 50 to 400 °C. The electrical resistance was measured by using a multimeter

(2002 multimeter, Keithley). In this study, the magnitude of the gas response (S) was defined as the ratio ($R_{\text{air}}/R_{\text{gas}}$) of the resistance in air (R_{air}) to that in sample gas (R_{gas}). For comparison, porous CuO-free SnO_2 sensor and CuO-loaded commercial powder SnO_2 sensor [34-36] were fabricated and the H_2S gas sensing properties of both sensors were evaluated

2.3.2. Results and discussion

Synthesis of nanoporous SnO_2 -CuO structure

The as-anodized specimen was synthesized with same experimental condition and its product was reproducible. For remove upper layer closing inner porous structure (Figure 2.2.3), reactive-ion etching process was adapted. The reactive ion etching (RIE) using fluorocarbon-oxygen ($\text{CF}_4\text{-O}_2$) plasma effectively removed the non-porous barrier layer and widened the pore diameter. The longer etching time reduced the anodic oxide thickness and pore wall thickness, and the higher CF_4 flow rate resulted in the local collapse of porous structure and covering the entrance of pore, which is probably to be attributed to formation of less volatile phase to deposit its by-product on top surface of films as shown in Figure 2.3.1. With the variation of etching time, the diameter of pores increased and the wall thickness was thinned as the etching time increased, whereas the

thickness of as-etched films decreased. (Figure 2.3.2) In the optimized etching conditions (etching time: 7 min, CF_4 flow rate: 10 sccm), nano-pores of 100~200 nm diameter and ~50 nm wall thickness were exposed on the surface of anodic oxide (Figure 2.3.3(a, c)). Unlike the circular pores in an ordered hexagonal array of anodic aluminum oxide [32,33], the pore shape of anodic tin oxide was rather irregular with a wide range of size distribution. It was apparent from the cross-sectional view that the top barrier layer was completely etched away and the discontinuous nano-channel structure was still maintained (Figure 2.3.3(b, d)). After annealing at 700 °C for 1 h, the pore wall was changed into granular due to sintering, but the microscopic features of the nano-sized pores and vertical nano-channels remained same indicating a high thermal stability of anodized films (Figure 2.3.3(b, d, f)). The CuO impregnated SnO_2 films exhibited the similar microstructural characteristics to as-annealed specimens except the slight increase of wall thickness. (Fig. 2.3.4)

XRD pattern showed that the amorphous anodic oxide was fully crystallized at 700 °C and only SnO_2 peaks were detected in as-annealed film (Figure 2.3.5(c)). In CuO impregnated SnO_2 film, no evidence of Cu-containing compound such as CuO was found (Figure 2.3.5(d)). The presence of Cu was confirmed by XPS analysis and the oxidation of Cu to CuO was ensured at 700 °C [37-41]. The amount of copper was approximately 3 wt% based on the EDS,

EPMA, and ICP-AES analyses. The structure of as-anodized and as-annealed films was further investigated by HR-TEM after scratching out from the substrate. The selected area electron diffraction pattern (SAED) and high resolution image indicated that as-anodized film was amorphous (Figure 2.3.6(a)). The spot and ring pattern observed in the SAED pattern of as-annealed anodic oxide revealed the randomly oriented polycrystalline nature, and the patterns were completely indexed to the rutile SnO_2 (JCPDS No. 41-1445). The high resolution TEM image clearly displayed the lattice fringes, indicating a high crystalline nature (Figure 2.3.6(b)).

Gas sensing measurements

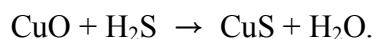
The response transient of nano-porous CuO-SnO_2 sensor toward H_2S gas balanced with air at 250 °C is shown in Figure 2.3.7. Upon injecting a sample gas (H_2S), the resistance decreased rapidly and recovered rather slowly with exposure to air, exhibiting a typical n-type semiconductor sensing behavior. The sensing signal was quite stable and reversible even after switching gases several times. The magnitude of the gas response (S) decreased almost linearly with decreasing H_2S concentration, and the detection limit was approximately ~0.2 ppm.

The temperature dependence of gas response in nano-porous CuO-SnO_2 sensor toward 20 ppm H_2S is shown in Figure 2.3.8 along with that of nano-porous CuO-free SnO_2 sensor and $\text{CuO-loaded commercial powder SnO}_2$ sensor.

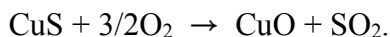
The gas response of nano-porous CuO-free sensor was relatively low, and maximum gas response of ~ 5 was observed at $350\text{ }^{\circ}\text{C}$ [42]. The CuO loading significantly enhanced the gas response toward H_2S and reduced the optimum sensing temperature, which resulted in the maximum gas response of ~ 39 at $250\text{ }^{\circ}\text{C}$. The determined gas response of nano-porous CuO-SnO₂ sensor was higher than that of CuO-loaded commercial powder SnO₂ sensor, which indicates that nano-porous structure with high surface area is beneficial to the enhanced gas response [43]. In addition, the gas response of nano-porous CuO-SnO₂ sensor to other representative reducing gases such as H_2 , CO, NH_3 , and $\text{C}_2\text{H}_5\text{OH}$, were examined at $250\text{ }^{\circ}\text{C}$. As shown in Figure. 2.3.9, the gas response toward these gases was extremely low either 20 or 100 ppm concentration, and thus, the nano-porous CuO-SnO₂ sensor exhibited a remarkably higher selectivity toward H_2S gas. The enhanced sensitivity and selectivity toward H_2S gas in nano-porous CuO-SnO₂ sensor can be understood in terms of the formation of resistive p-CuO/n-SnO₂ junction and the disruption of resistive junction by the sulfurization of CuO into metallic conductor CuS upon exposure to H_2S [34-36,39-41,44]. To confirm the hypothesis suggested by previous researchers [34-36,39-41,44], the chemical states of porous CuO-SnO₂ film before and after H_2S exposure were investigated by XPS.

The core level Cu2p and S2p spectra of nano-porous CuO-SnO₂ film are shown in Figure. 2.3.10. As-prepared nano-porous CuO-SnO₂ film exhibited a

single peak of Cu2p_{3/2} at 933.6 eV. The observed binding energy is consistent with the value for Cu in CuO [45], which indicated that CuO was successfully impregnated into the nano-porous SnO₂ film. After exposed to 100 ppm H₂S at 200 °C for 1 h, Cu2p_{3/2} peak shifted to lower energy of 931.8 eV and S2p signal appeared at 162.2 eV. These values are in good agreement with the values for the lattice copper and sulfur of CuS, respectively [45]. The formation of Cu₂S cannot be completely ruled out, but the sulfurization in the H₂S-containing atmosphere takes place and CuO converts to CuS by the following chemical reaction:



On the subsequent exposure to air, CuS was oxidized back to CuO and XPS spectra of as-prepared state were restored.



The change of binding energy (Sn3d_{5/2} and O1s) in nano-porous CuO-SnO₂ film determined by XPS is shown in Figure 2.3.11(a) as a function of H₂S exposure temperature. The as-prepared CuO-free SnO₂ exhibited a doublet of Sn3d at 495.2 (3d_{3/2}) and 486.8 (3d_{5/2}) eV and a single peak of O1s at 530.7 eV, which are in good agreement with the values for the lattice tin and oxygen of SnO₂, respectively [45]. The Sn3d_{5/2} and O1s peaks were observed at 486.1 and 529.9 eV, respectively, in as-prepared CuO-SnO₂ film and the binding energy was

lowered by as much as 0.7~0.8 eV. The binding energy downward shift in CuO-SnO₂ film was attributed to the formation of p-n junction between CuO (p-type) and SnO₂ (n-type) and resultant band bending and increase in work function of SnO₂ [35,36, 39-41]. When exposed to 100 ppm H₂S, the Sn3d_{5/2} and O1s peaks shifted upward with increasing the exposure temperature and reached the binding energies of CuO-free SnO₂ film at 200 °C and remained constant at higher temperature. The binding energy upward shift is associated with the conversion of CuO into CuS in the H₂S-containing atmosphere and the disruption of p-n junction due to the formation of metallic CuS. It was found that the complete conversion of CuO into CuS requires the heat treatment at least 200 °C. The variation of binding energy with CuO impregnation and H₂S exposure was reflected on the resistance and gas response (S) of the sensors. Thus, the resistances in 100 ppm H₂S (R_{H₂S}) are shown in Figure 2.3.11(b) as a function of H₂S exposure temperature for both CuO-free SnO₂ and CuO-SnO₂ films. The resistance of CuO-SnO₂ film was two or three orders of magnitude higher than that of CuO-free SnO₂ film due to the formation of resistive p-n junction. While the resistance of CuO-free SnO₂ film was relatively insensitive to temperature, the resistance of CuO-SnO₂ film decreased drastically up to ~250 °C, which is associated with the sulfurization of CuO. As a result, the maximum gas response toward H₂S was observed at 250 °C in CuO-SnO₂ film. The increase of resistance above 250 °C is related to the formation of Cu₂S, which is an ionic conductor with

higher resistivity than the metallic CuS. It is known that the crystal structure of CuS is changeable at 103 °C and transforms into Cu₂S above 220 °C [51].

2.3.3. Conclusion

The anodic oxidation of Sn thin films on SiO₂/Si substrate yielded the nano-porous SnO₂ with 1-D nano-channels, but the surface was covered with 50~100 nm thick non-porous barrier layer. The non-porous layer was successfully etched away using fluorocarbon-oxygen (CF₄-O₂) plasma, which resulted in the nano-porous SnO₂ films with 100~200 nm pore diameter and ~50 nm wall thickness. The developed nano-porous SnO₂ films on SiO₂/Si substrate are expected to be used in such applications as anodes for lithium-ion battery, dye sensitized solar cell (DSSC), chemical sensors, and templates for other nanostructures and could be integrated to CMOS chip-based devices. As an example, a gas sensor was fabricated after impregnating CuO into the nano-channels. The CuO-SnO₂ sensor showed an excellent sensitivity and selectivity toward H₂S gas, which was attributed to the formation and disruption of resistive p-CuO/n-SnO₂ junction depending on the atmosphere.

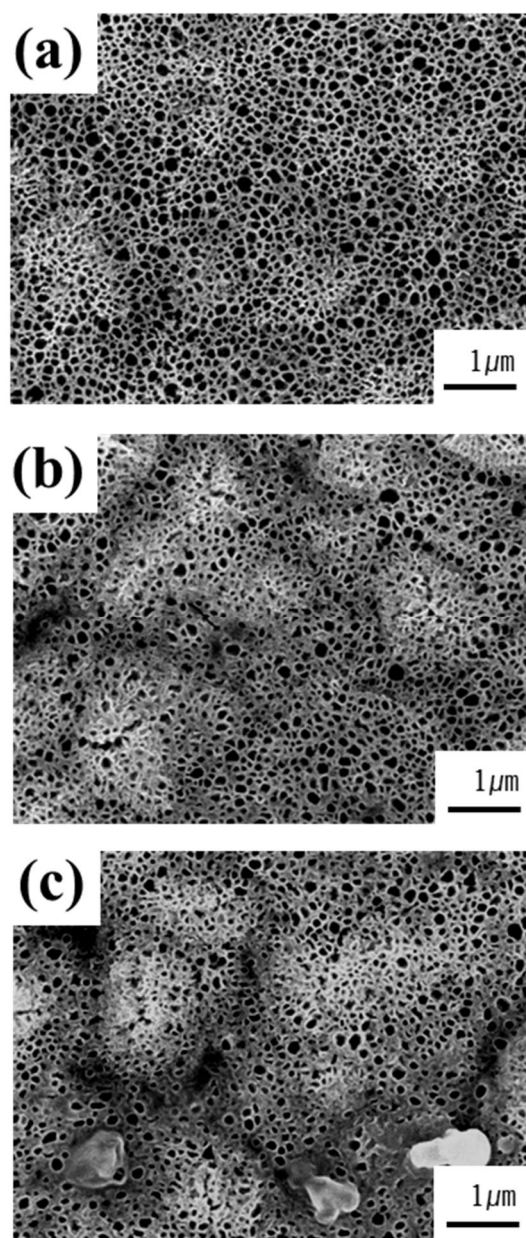


Figure 2.3.1 Morphology changes with the variation of CF_4 flow for 7 min; (a) 10, (b) 20, (c) 30 sccm

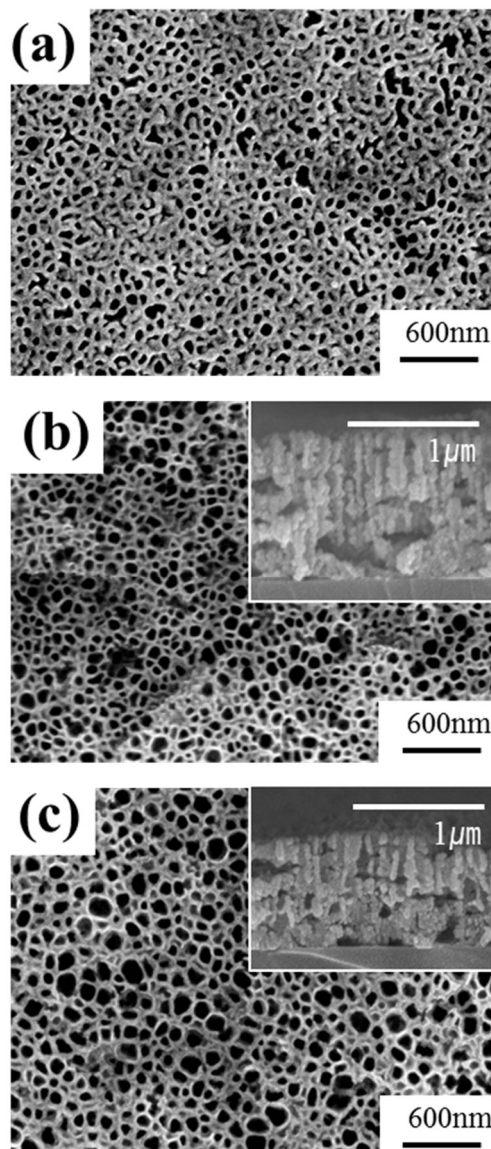


Figure 2.3.2 Morphology changes with the variation of etching time with 10 sccm of CF_4 ; (a) 5, (b) 7, (c) 10 min

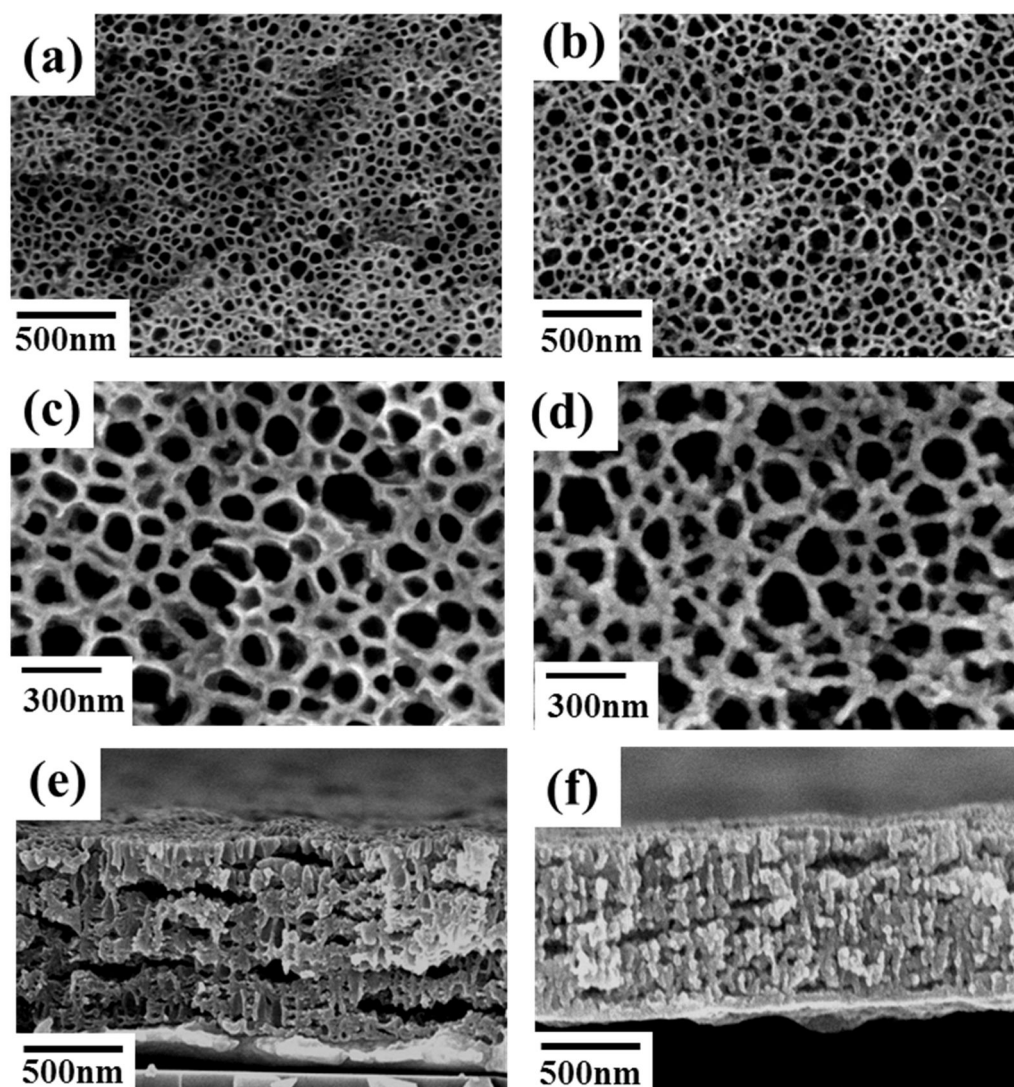


Figure 2.3.3 Plain and cross-sectional view of (a, c, e) as-etched film and (b, d, f) as-annealed film

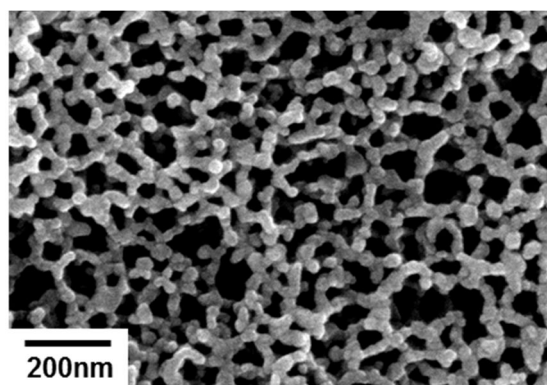


Figure 2.3.4 Plain view of as-CuO impregnated film

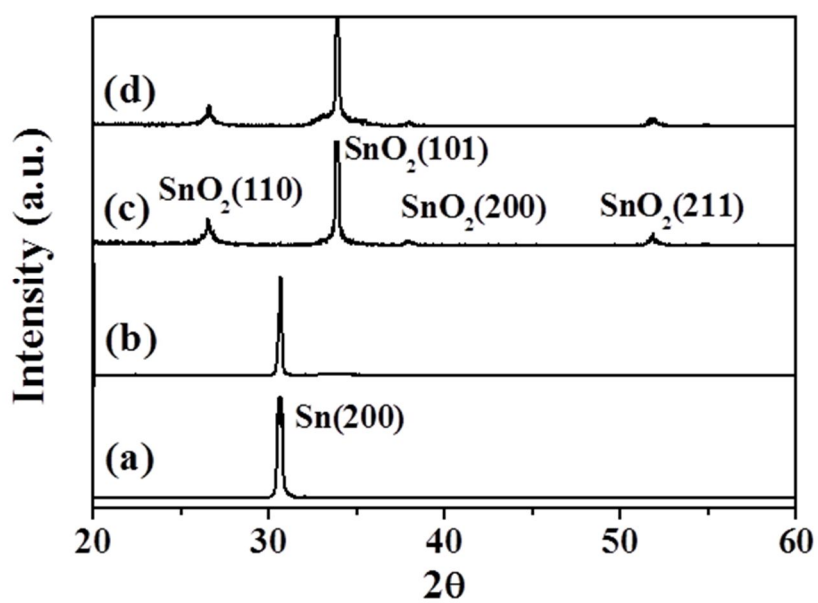


Figure 2.3.5 X-ray diffraction patterns; (a) as-Sn prepared film, (b) as-anodized film, (c) as-annealed film and (d) as-CuO impregnated film

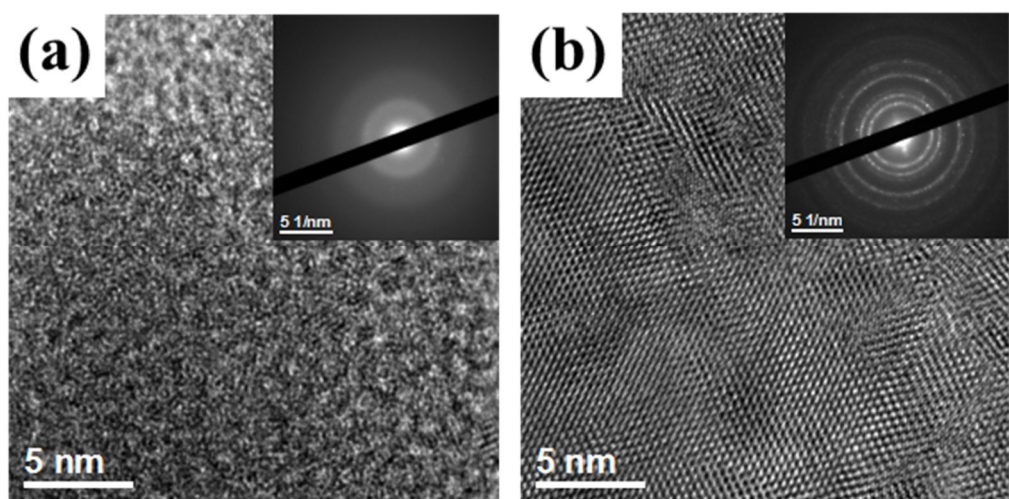


Figure 2.3.6 The selected area electron diffraction pattern (SAED) and high resolution image of (a, b) as-anodized film and (b) as-annealed film

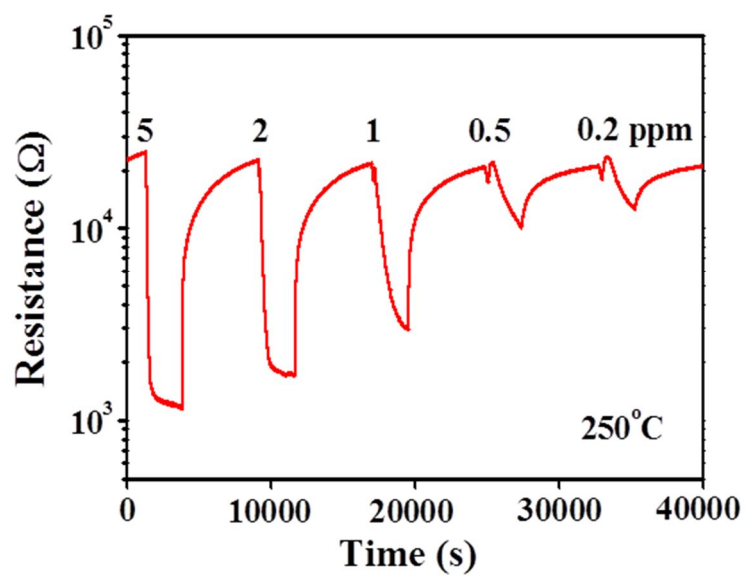


Figure 2.3.7 Gas sensing transient of nanoporous $\text{SnO}_2\text{-CuO}$ film toward H_2S at 250°C

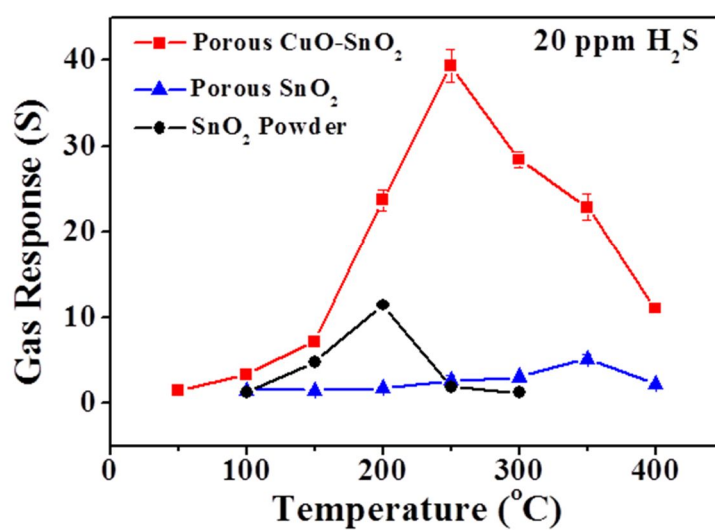


Figure 2.3.8 Temperature dependence of gas response in nanoporous $\text{SnO}_2\text{-CuO}$ sensor toward 20 ppm H_2S

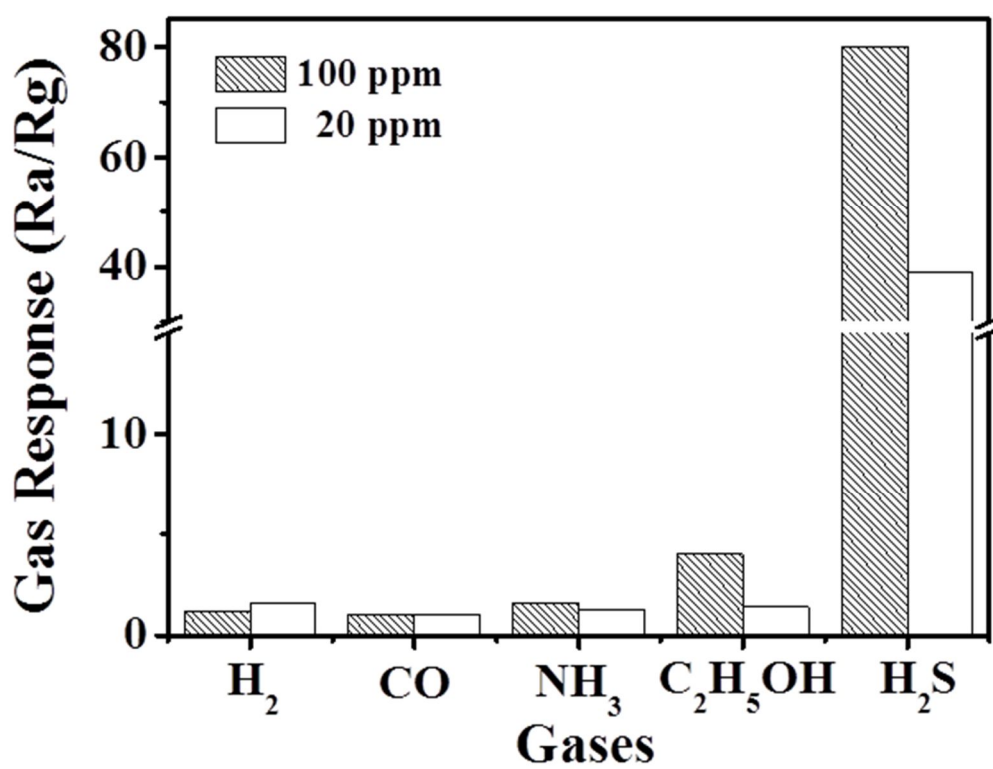


Figure 2.3.9 Gas response of nano-porous CuO-SnO₂ sensor to H₂, CO, NH₃, C₂H₅OH and H₂S at 250 °C

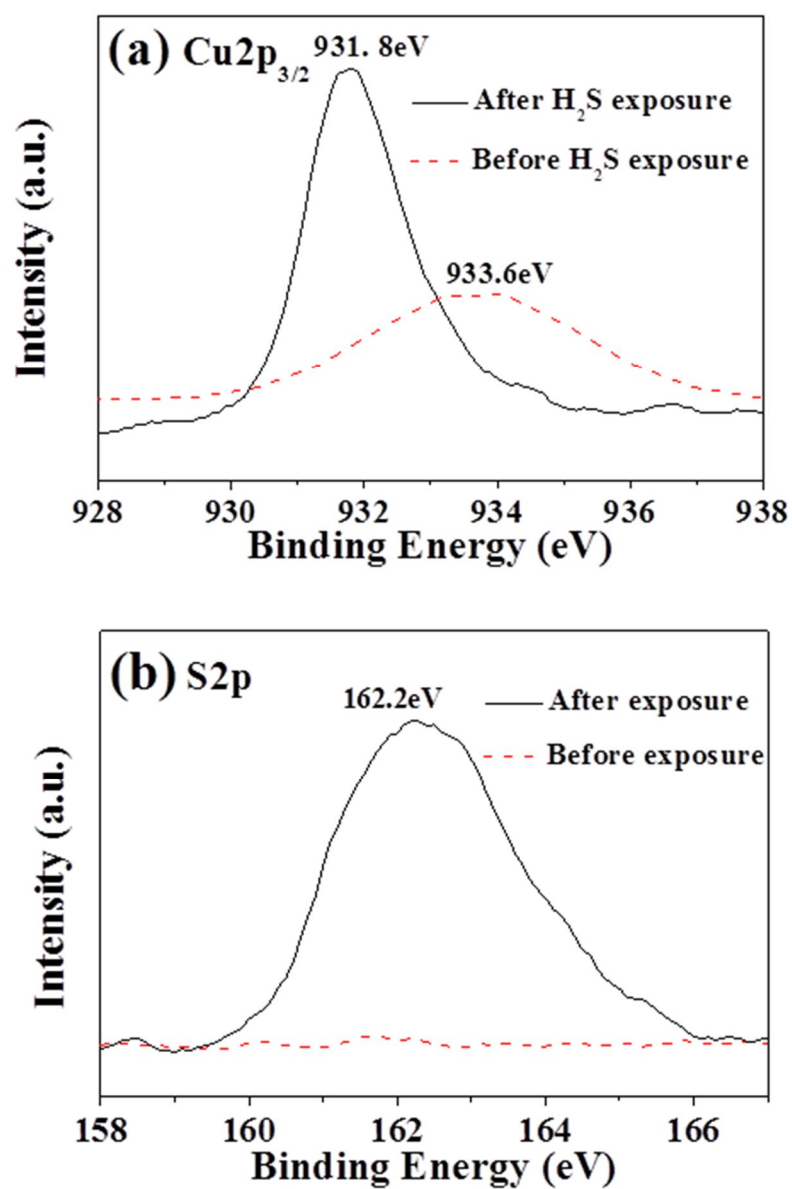


Figure 2.3.10 The (a) Cu2p and (b) S2p XPS spectra of nano-porous CuO-SnO₂ film before and after H₂S exposure at 250°C

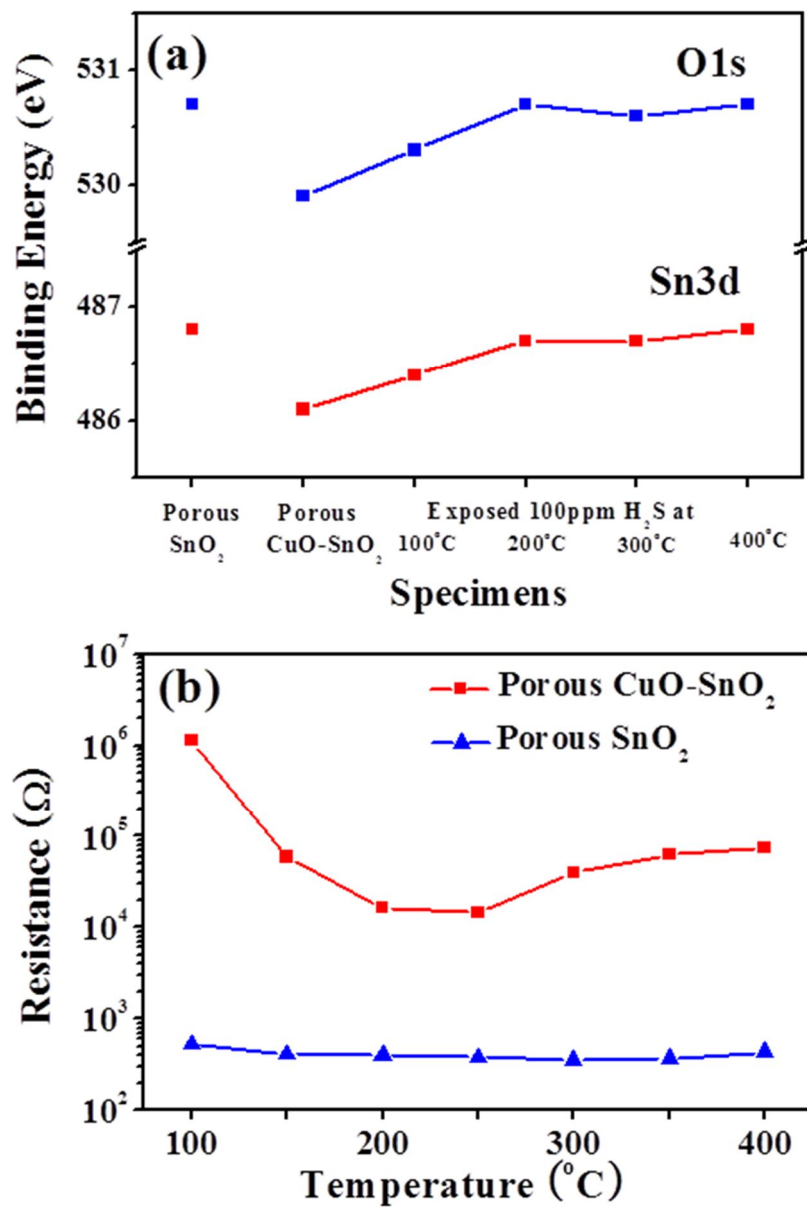


Figure 2.3.11 (a) Bind energy shift of Sn3d_{5/2} and O1s and (b) electrical resistance changes as increasing reaction temperature with H₂S

2.4 Synthesis of porous SnO₂ dendrite via electrodeposition and its gas sensing property

2.4.1. Experimental procedure

Porous SnO₂ dendrites structure were prepared by an anodic oxidation of Sn thin films deposited on SiO₂/Si substrates using a thermal evaporation and detailed experimental conditions for Sn coating were shown in 2.2.1.

Electrochemical deposition process and annealing: In order to form the porous Sn foam, the electrochemical deposition was performed on Sn/SnO₂ coated substrates in the electrolyte containing 1.5 M sulfuric acid (Kanto chemicals, 96%) and 0.15 M tin sulfate (Sigma-Aldrich, 98%). The coated substrate was used as a cathode and SUS was used as an anode and the distance between two electrodes was kept at 35 mm. The deposition was carried out at a constant current (0.67~2 Acm⁻²) using a DC power supply (Fine-Power, F-100) for 5~15 s. For crystallization, the fabricated Sn foams were annealed at 700 °C for 1 h in air.

Analysis: The surface and cross-sectional morphologies of the films and foams were examined by scanning electron microscopy (SEM, JSM-5600, JEOL). The phases of the specimens were determined by X-ray diffraction (XRD, M18XHF-

SRA) with Cu K α radiation.

Gas sensing measurement: A pair of Pt electrodes with 6 mm gap was formed by sputtering on the porous SnO₂ foam through a mask and Au lead wires were attached to them using an Ag paste. Thereafter, all the sensors were fired at 600 °C for 1 h in order to make the electrical contact between Ag paste and Au lead wires. The sensor element was placed in a quartz tube located inside an electrical tube furnace with a gas inlet and outlet. A continuous flow-through measurement system was used, and the sample gases used were 100 ppm H₂, CO, NH₃, NO₂, and 10~100 ppm C₂H₅OH balanced with air. The gas sensing properties were determined by measuring the changes of electric resistance between sample gas and reference gas (dry air) at temperatures from 200 to 450 °C. The electrical resistance was measured by using a multimeter (2002 multimeter, Keithley). In this study, the magnitude of the gas response (S) was defined as the ratio (R_{air}/R_{gas}) of the resistance in air (R_{air}) to that in sample gas (R_{gas}). For comparison, SnO₂ powder sensor was fabricated using a commercial SnO₂ powder and the C₂H₅OH gas sensing properties were evaluated.

2.4.2. Results and discussion

Synthesis of porous SnO₂ dendrite structure

The electrodeposition process yielded the open porous Sn foam as shown in Figure 2.4.1. The pore size and wall thickness of the foam increased with increasing the deposition time due to the coalescence of liberated hydrogen bubbles from the substrate (Figure 2.4.1(a)~(c)). The foam wall was composed of numerous dendrites and the dendritic branches were three-dimensionally interlocked forming the highly porous, self-supporting 3D network structure (Figure 2.4.1(d)). The trunks and branches in the dendritic structure were in the order of tens of micrometers. The cross-sectional image revealed that the Sn film deposited by thermal evaporation, which acted as a current path during electrodeposition, remained intact and the dendrites in the Sn foam were strongly bonded to the film (Figure 2.4.1(e)). The SUS 304 stainless steel was also employed as a cathode after SnO₂ deposition and the porous Sn foams with similar dendritic morphology were developed (Figure 2.4.2). Copper has been used as a substrate to fabricate the Sn foam, and it appears that the substrate had little effect on the foam structure. [46,47]

The topotactic thermal oxidation was used to convert the metallic Sn foam into the corresponding oxide foam without losing the shape and integrity of porous structure.[48] For this, a slow heating rate of 1 °C/min was employed, which allowed to grow a thin supporting oxide skin on the surface before melting (point of Sn=232 °C tin) and preserve the structural integrity.[48] The

morphology of the oxide foam after heat treatment at 600 °C for 1 h is shown in Figure 2.4.3. The macro-porous structure was maintained during thermal oxidation and the pore size and wall thickness remained almost same (Figure 2.4.3(a)). The trunks and branches in the wall were slightly distorted, but the dendritic structure was also preserved indicating a high thermal stability of synthesized foam (Figure 2.4.3(b)). The wavy (or granular) surface of the dendrites is due to uneven oxidation and sintering. From the cross-sectional view (Figure 2.4.3(c)), 3-dimensionally interlocked porous oxide foam of ~100 µm thick was confirmed and strongly adhered to the substrate. The Sn film also remained the same after converting to the oxide film (inset of Figure 2.4.3(c)). At high heating rate (fast oxidation) of 10 °C/min, a significant structural deformation and agglomeration was observed, and the branches in dendritic structure were shorter and thicker than one annealed with a slow heating rate (Figure 2.4.3(d)).

The phase change during thermal oxidation was examined by XRD on the Sn foam heat-treated from 200 to 600 °C at a step of 100 °C (Figure 2.4.4) and cooled down to room temperature. As-deposited foam was a crystalline tetragonal Sn (JCPDS No. 04-0673). No phase change was observed at 200 °C and the formation of the thin oxide skin layer, suggested in the previous study [48], was not confirmed. An intermediate phase, romarchite SnO (JCPDS No. 06-0395), appeared at 300 °C, and another intermediate phase, triclinic Sn₃O₄ (JCPDS No.

16-0737), was found at 400 °C. The peaks for Sn were still observed at 500 °C implying that tin exists as a molten tin confined to the interior surrounded by outer oxide layer. At 600 °C, all the diffraction peaks were indexed as cassiterite SnO₂ (JCPDS No. 41-1445), and no peak for Sn, SnO, and Sn₃O₄ was detected. Thus, the stoichiometric ratio of oxygen to tin increased with annealing temperature and the thermodynamically stable oxide, SnO₂, was realized above 600 °C. It was reported that the oxidation process of Sn is kinetically controlled and the oxygen ion diffusion through the various oxide layers is rate-determining process. [48]

Gas sensing measurement

The response transient of porous SnO₂ foam sensor toward ethanol gas balanced with air at 300 °C is shown in Figure 2.4.5. Upon injecting a C₂H₅OH gas, the resistance decreased rapidly and recovered rather slowly with exposure to air, exhibiting a typical n-type semiconductor sensing behavior. The resistance of the sensor in air was in the range of 50~60 MΩ at 300 °C. The sensor showed a stable response down to 10 ppm C₂H₅OH and the magnitude of the gas response (S) decreased almost linearly with decreasing the C₂H₅OH concentration.

The gas response of porous SnO₂ foam gas sensor toward 10~100 ppm C₂H₅OH is shown in Figure 2.4.6(a) as a function of operating temperature. The foam sensor responded to C₂H₅OH gas in the temperature range of 200~500 °C. The maximum gas response (S=12) toward 100 ppm C₂H₅OH was observed at

300 °C and it was shifted to lower temperature with decreasing the C₂H₅OH concentration. (gas response and optimum temperature comparison) [50-56] The response time (t_{90%}) was defined as the time required for the sensor to reach 90% of the final signal and plotted in Figure 2.4.6(b).

The response time was in general shortened with increasing C₂H₅OH concentration, and the minimum response time was found between 250 and 300 °C, which coincide with the maximum gas response. Thus, the foam sensor exhibited the response time less than 3 s toward 100 ppm C₂H₅OH above 250 °C. 57 Below 250 °C, the response time significantly increased in all C₂H₅OH concentrations possibly due to the low adsorption kinetics. In order to confirm the low temperature detection and fast response of the porous SnO₂ foam sensor, the commercial SnO₂ powder sensors with same electrode geometry was fabricated, and the C₂H₅OH sensing performance was evaluated (Figure 2.4.7). The SnO₂ micro-powder sensor exhibited the similar magnitude of gas response above 300 °C, but the gas response could not be measured below 250 °C due to a high resistance and an equipment limitation (up to ~10¹² Ω). The response time of the micro-powder sensor was longer than 20 s in the measured temperature range, which was an order of magnitude longer than that of foam sensor. In addition, the ethanol sensing behavior of commercial SnO₂ nanopowders also showed even higher resistance in air therefore a gas sensing behavior was observed down to

400°C and unstable. This is because the generated electrons from gas reaction should get through a number of interfaces between particles and grain boundary throughout a large gap of parallel electrode geometry, which are more than those of porous SnO₂ foam with dendritic shaped grain.

In case of porous SnO₂ foam sensor, the fast response in overall ethanol concentration was observed even in relatively low operating temperature and it leads from that three-dimensionally interconnected open porous structure of the SnO₂ foam sensor enables the rapid gas diffusion resulting in the fast and stable gas response shown in low range of electrical resistance. The gas response of porous SnO₂ foam sensor toward 100 ppm H₂, CO, NH₃, and NO₂ were investigated at 300 °C (Figure 2.4.8). The foam sensor responded to the H₂, CO, and NH₃ gases with a short response time, but the magnitude of gas response was significantly lower than that of C₂H₅OH. On the other hand, the NO₂ response was appreciable, but the response time was too long (>100 s). The higher gas response toward ethanol in SnO₂-based sensors compared to other reducing gases has been attributed to the higher reactivity of ethanol in this temperature range and more electron generation when the same number of gas molecules react with the surface-adsorbed oxygen species. [58,59] The long-term stability of porous SnO₂ foam sensor was examined by repeating the sensing measurement at 300 °C. The sensing signal was quite stable and reversible during the measurement. After

30 cycles toward 10 ppm $\text{C}_2\text{H}_5\text{OH}$, the resistances both in air and sample gas decreased by 10% of the initial ones, but the magnitude of gas response remained almost same indicating the relatively stable sensing behavior of the foam sensor. (Figure 2.4.9)

2.4.3. Conclusion

The electrochemical deposition using Sn thin film as a cathode on SiO_2/Si substrate yielded the three-dimensional Sn porous structure and its pore wall consisted of dendrite structures. For the crystallization to SnO_2 , the heat treatment was carried out at 700°C with slow ramping rate, $1^\circ\text{C}/\text{min}$. Then, it was confirmed that highly porous dendritic structures were conserved after heat treatment even Sn has low melting point, 232°C . The developed three-dimensional SnO_2 foams on SiO_2/Si substrate are expected to be used in such applications as anodes for lithium-ion battery, fuel cell, chemical sensors, and membrane for filtering. As an example, a gas sensor was fabricated and showed an excellent sensitivity, fast response and high selectivity toward ethanol gas thanks to the effective and rapid gas diffusion onto the entire gas sensing materials, indicating which porous structures are advantageous to enhance the gas sensing properties.

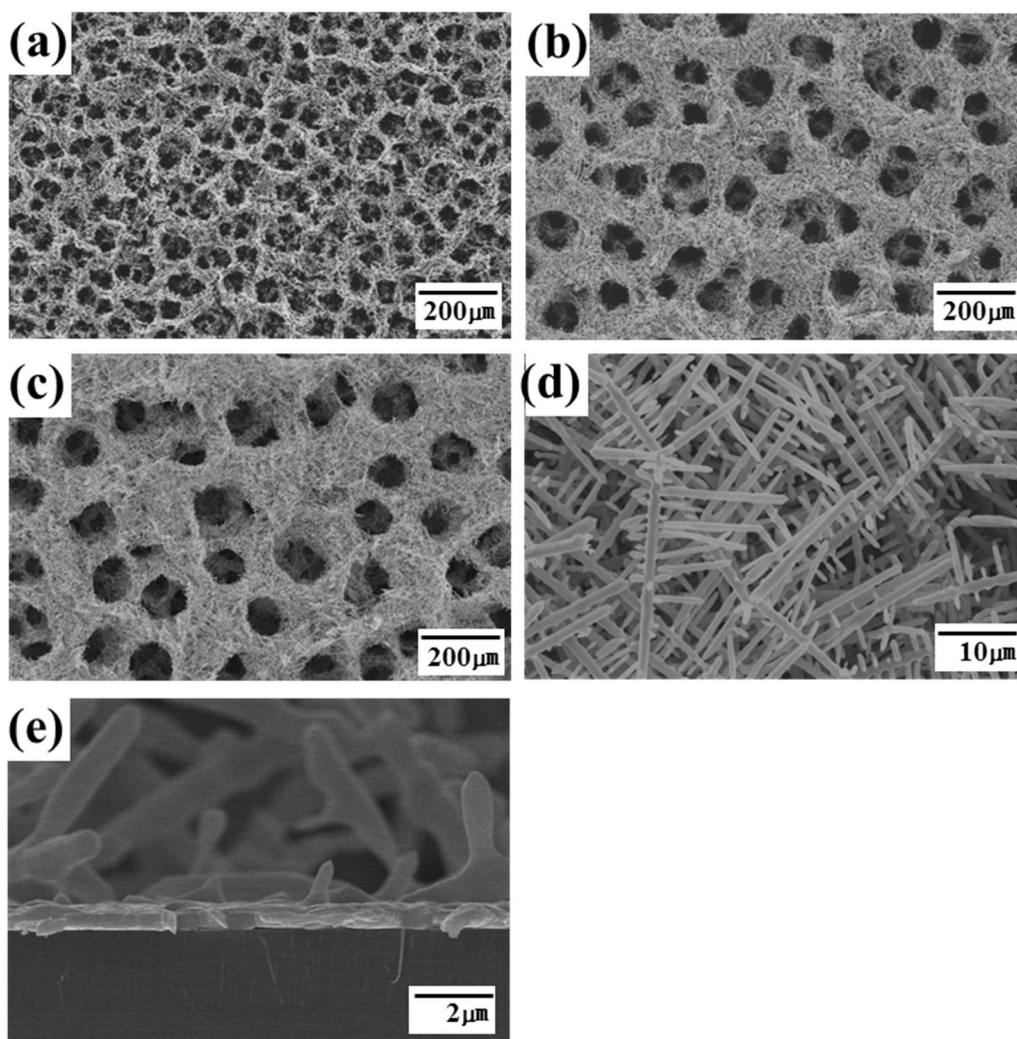


Figure 2.4.1 SEM micrographs of Sn foam deposited on SiO₂ applying cathodic current density of 2 A cm⁻² for (a) 5 sec, (b) 10 sec, (c) 15 sec and (d) detailed microstructure of (c), cross sectional view of interface between Sn deposits and substrate (e)

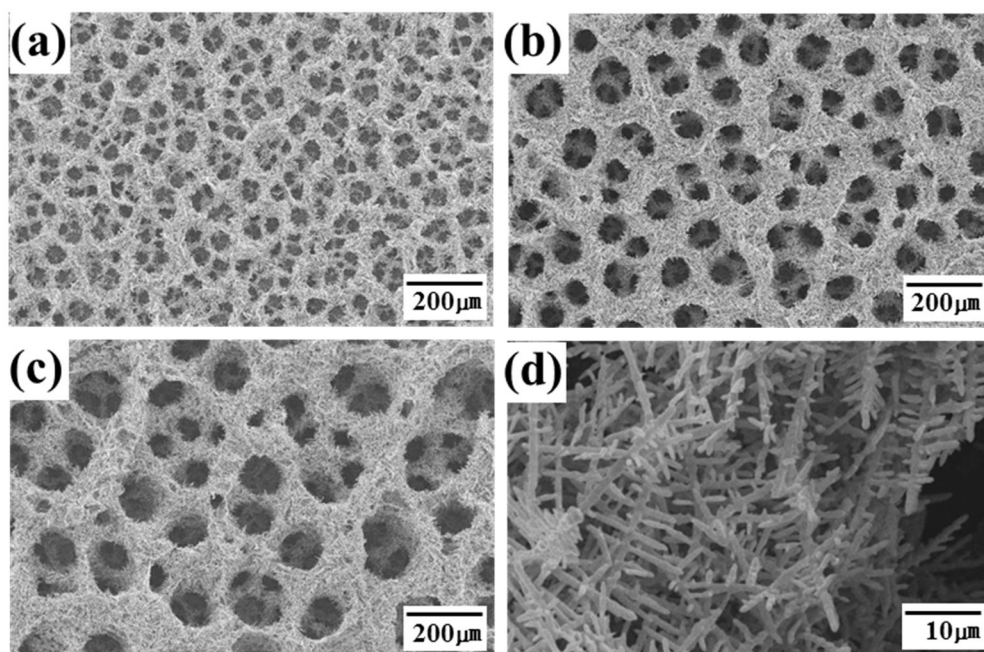


Figure 2.4.2 SEM micrographs of Sn foam deposited on SUS applying cathodic current density of 2Acm^{-2} for (a) 5sec, (b) 10sec, (c) 15 sec and (d) detailed micrograph of (c)

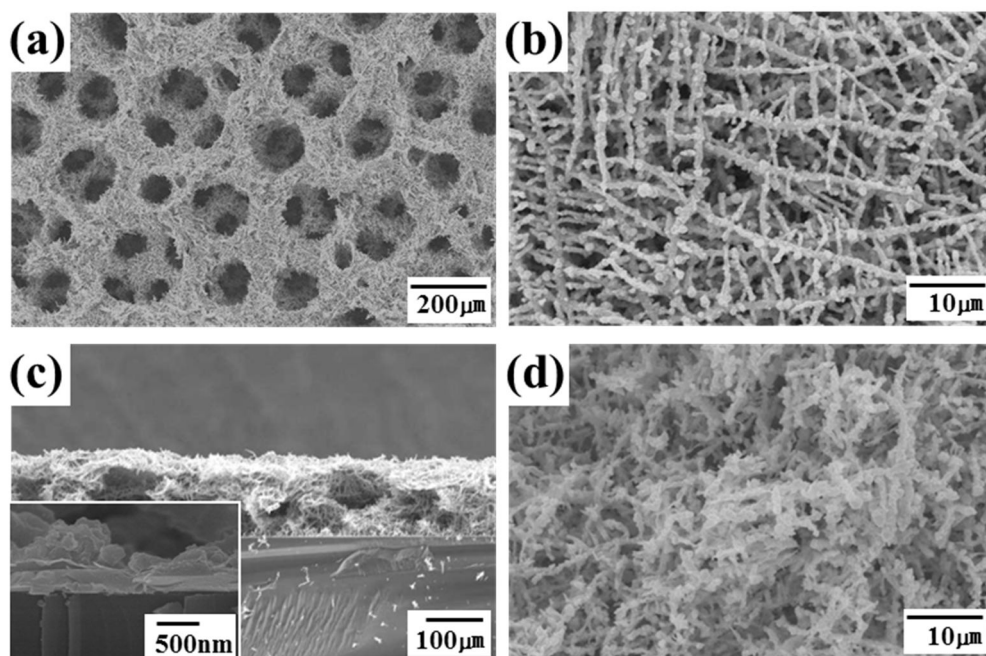


Figure 2.4.3. SEM micrographs of SnO_2 foam on SiO_2 annealed at 600°C for 1h with $1^\circ\text{C}/\text{min}$: Plain view (a, b) and its cross sectional view (c), and plain view (d) annealed at 700°C for 1h with $10^\circ\text{C}/\text{min}$

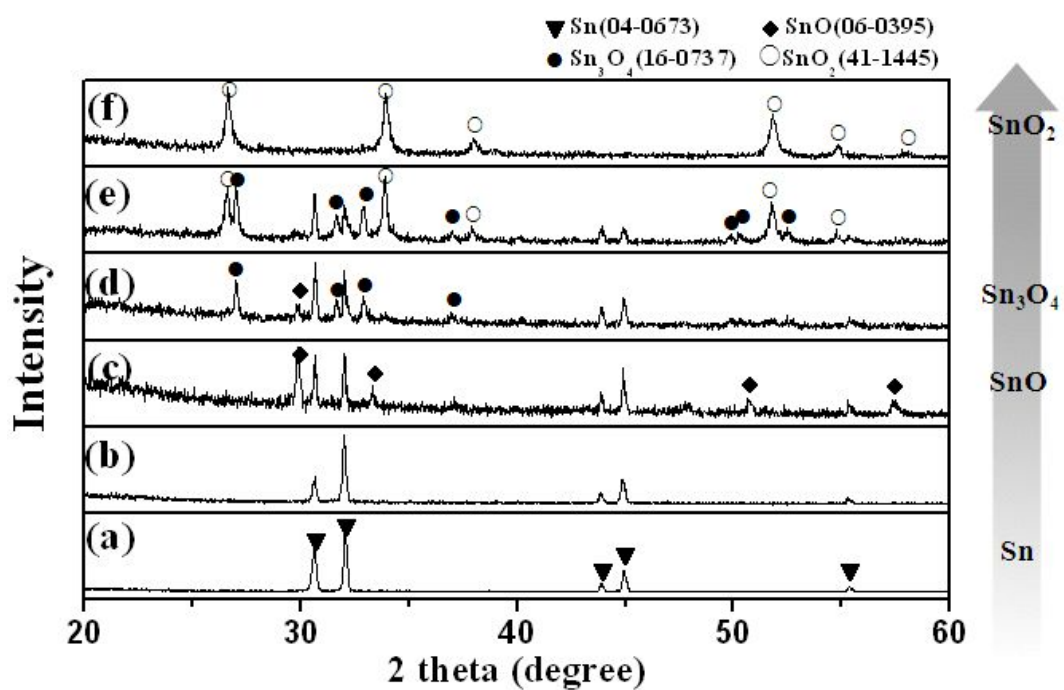


Figure 2.4.4. XRD patterns of Sn foam deposited on SiO₂ (a) and treated at (b) 200 °C, (c) 300 °C, (d) 400 °C, (e) 500 °C, (f) 600 °C

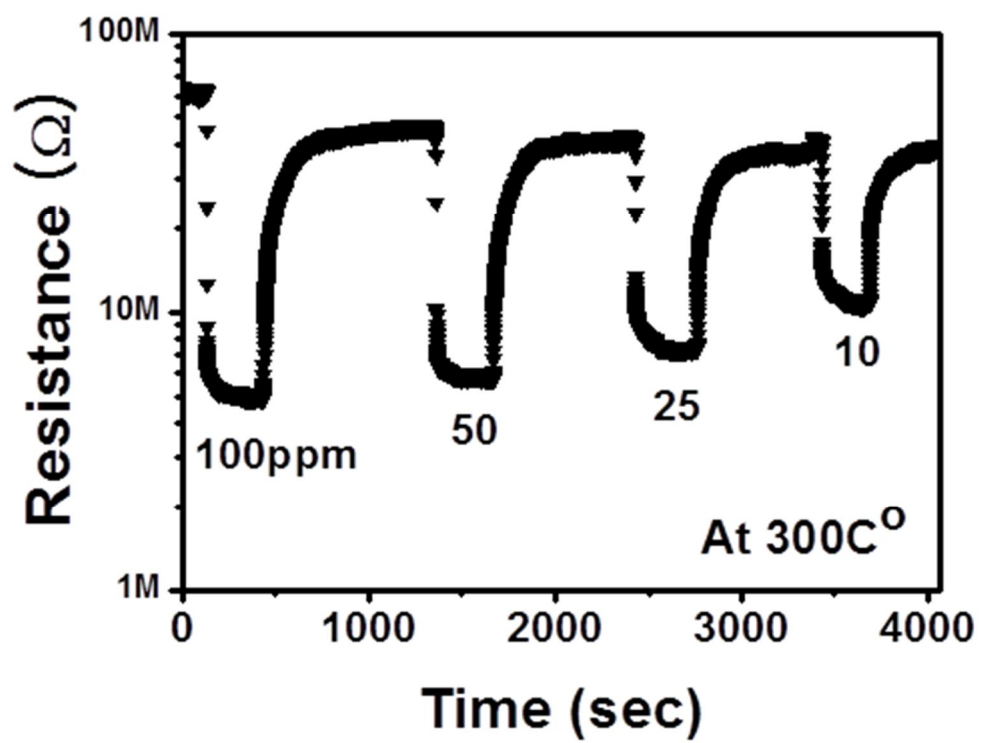


Figure 2.4.5. Response transient of porous SnO₂ foam sensor toward ethanol at 300°C

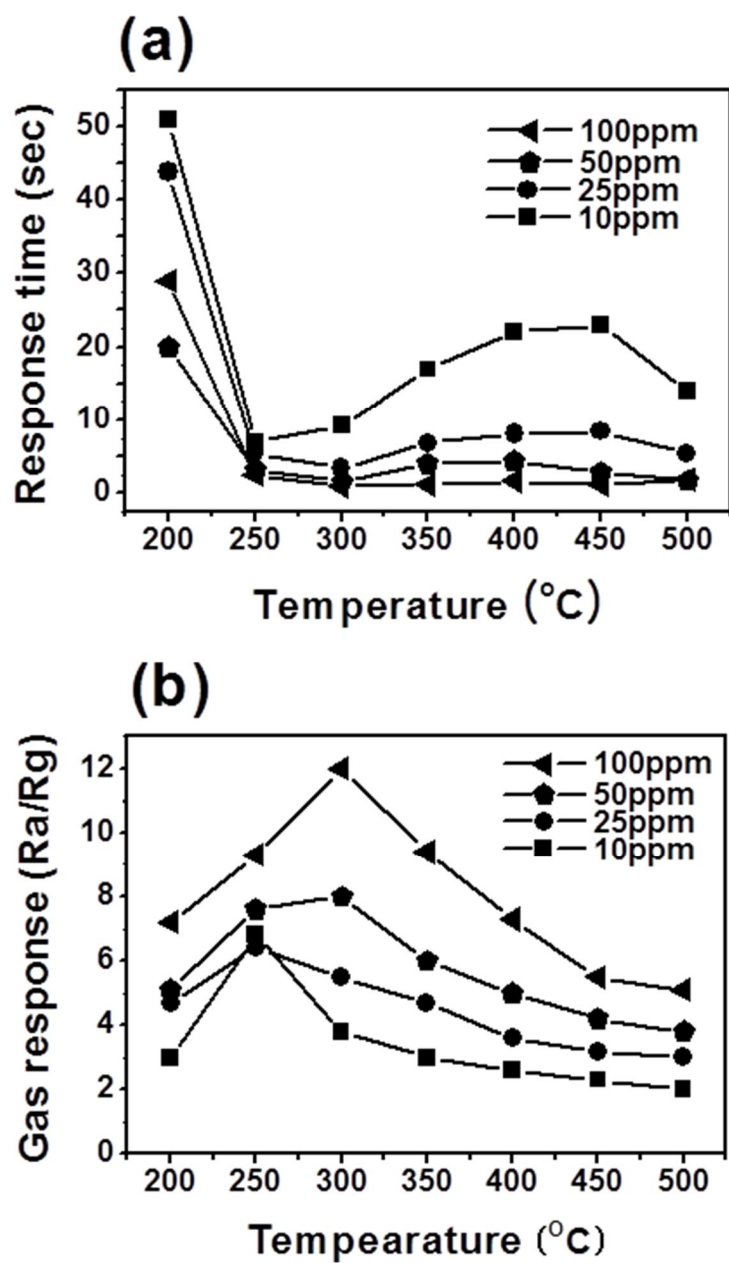


Figure 2.4.6. Response time (a) and gas response (b) of porous SnO_2 foam toward ethanol as a function of operating temperature

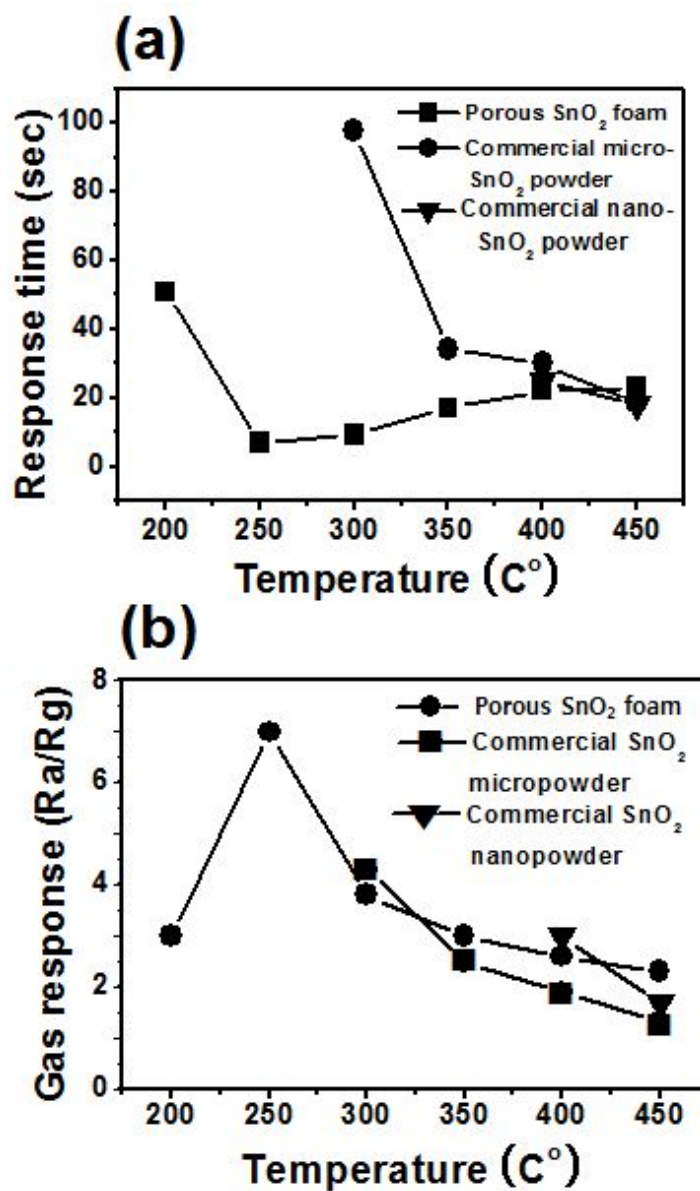


Figure 2.4.7. Response time (a) and gas response (b) toward 10ppm ethanol: Comparison between those of porous SnO₂ foam and commercial SnO₂ powder.

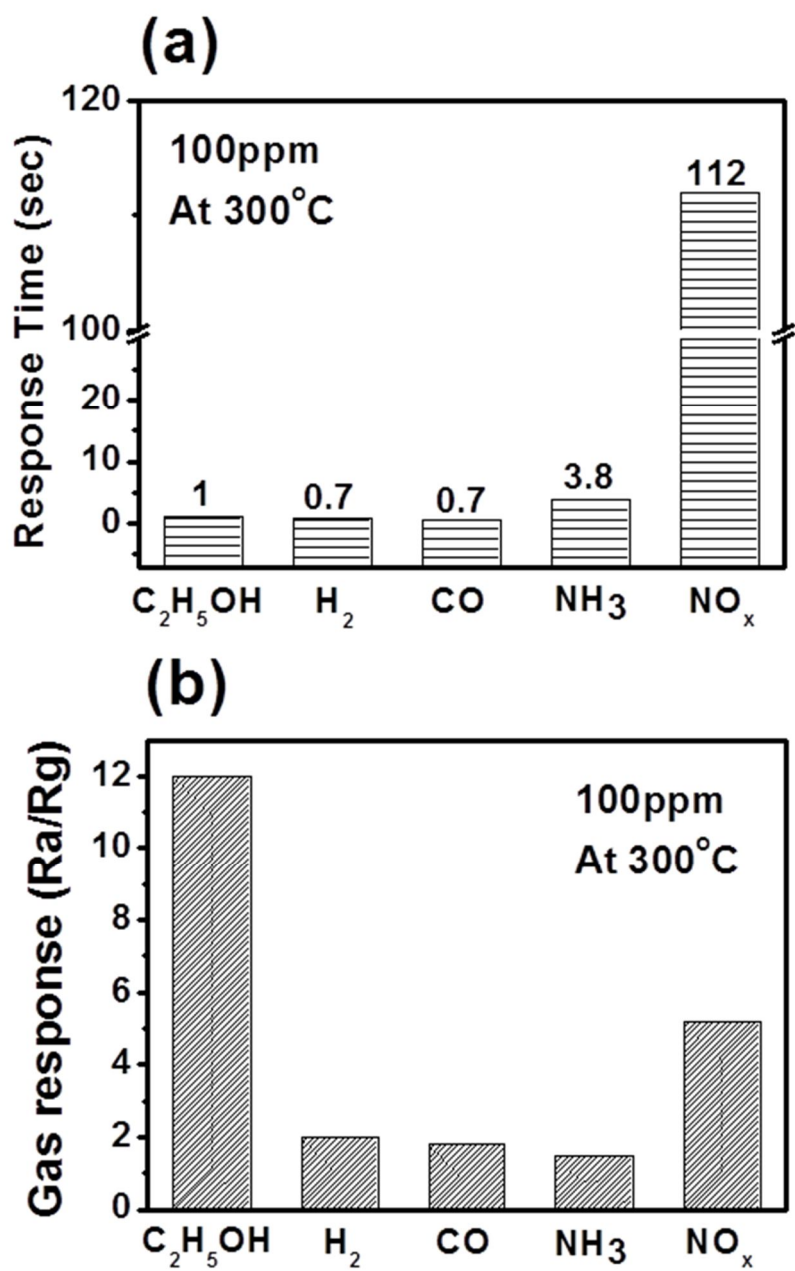


Figure 2.4.8. Response time (a) and gas response (b) of porous SnO_2 foam toward various gases.

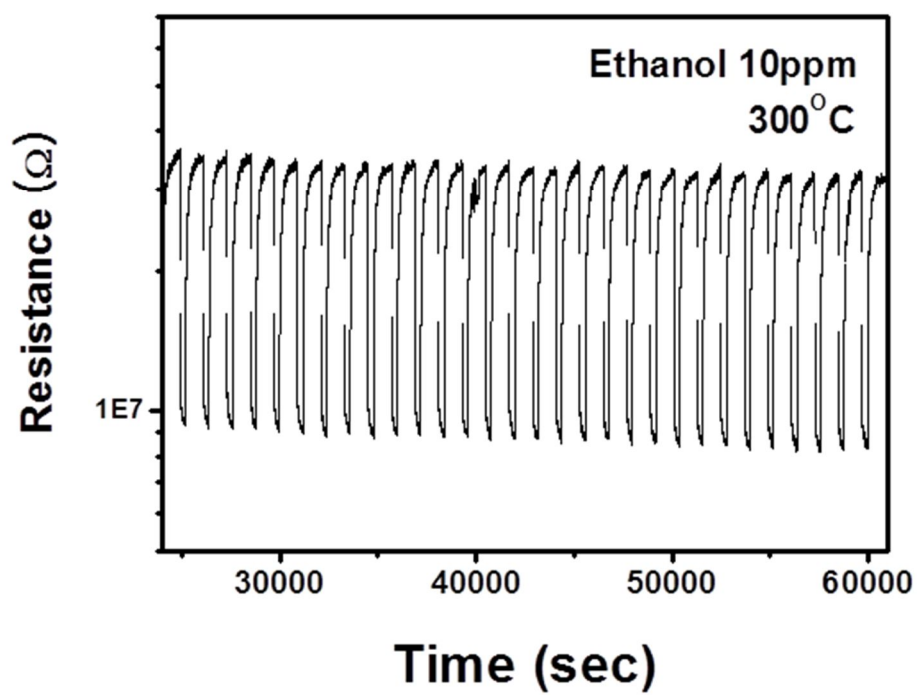


Figure 2.4.9. Changes of gas response during 30 cycle exposure toward 10 ppm ethanol at 300°C

2.5 3-D nanoporous SnO₂/CuO hybrid dendrite via co-electrodeposition and its gas sensing property

2.5.1. Experimental procedure

2.5.1.1 Synthesis of nanoporous Cu₆Sn₅@Sn and its synthesis mechanism

The electrochemical deposition was carried out on copper foil in the aqueous electrolytes containing 1.5 M sulfuric acid (Kanto Chemicals), tin sulfate (SnSO₄) (Sigma-Aldrich), and copper sulfate (CuSO₄ · 5H₂O) (Deajung Chemicals). The composition of CuSO₄ · 5H₂O and SnSO₄ was varied from 0 to 0.15 M. The graphite was used as an anode, and the distance between two electrodes was kept at 35 mm. The deposition was carried out at a constant current of 3 A cm⁻² using a DC power supply (F-100, Fine-Power) for 10 s at room temperature.

The phases of the specimens were determined by X-ray diffraction (XRD, Bruker D8-Advance) with Cu K α radiation. The morphology and composition of electrodeposited foams were characterized by field emission scanning electron microscopy (SEM, JSM-5600, JEOL) and transmission electron microscopy (TEM, Tecnai F20, FEI) equipped electron energy loss spectroscopy (EELS,

Gatan). Electrochemical measurements were conducted using an EG&G potentiostat/galvanostat (model 273) with a saturated calomel electrode (SCE) as a reference electrode and a platinum sheet as a counter electrode.

2.5.1.2 Synthesis of SnO₂/CuO nano-hybrid foams and their gas sensing properties

Nanoporous SnO₂ dendrites structure were prepared by an anodic oxidation of Sn thin films deposited on SiO₂/Si substrates using a thermal evaporation and detailed experimental conditions for Sn coating were shown in 2.2.1.

The electrochemical deposition was performed on Sn/SnO₂-coated substrate in the electrolyte containing 1.5 M sulfuric acid (Kanto Chemicals, 96%), 0.14 M tin sulfate (Sigma-Aldrich, 98%), and 0.01 M copper sulfate (Daejung Chemicals, 98%). The electrodeposition was carried out at a constant current of 0.667 Acm⁻² for 10 s. For oxidation, the synthesized foam was annealed at 700 °C for 1 h in air with a heating rate of 1 °C/min. The surface morphologies of the foams were examined by scanning electron microscopy (SEM, JSM-5600, JEOL). The phases of the specimens were determined by X-ray diffraction (XRD, M18XHF-SRA). For the gas sensing measurements, a pair of Pt electrodes with 6 mm gap was formed on the synthesized foam by sputtering and then annealed at 600 °C. The gas sensing properties were determined by measuring the changes of electric resistance between sample gas (H₂S, H₂, C₂H₅OH, CO, NH₃, NO_x) balanced with

air and reference gas (dry air) at 150 to 400 °C. The magnitude of gas response (S) was defined as the ratio (R_{air}/R_{gas}) of the resistance in air (R_{air}) to that in a sample gas (R_{gas}). The response time ($t_{90\%}$) was defined as the time required for the sensor to reach 90% of the final signal.

2.5.2. Results and discussion

2.5.2.1 Synthesis of nanoporous Cu_6Sn_5 @Sn and its synthesis mechanism

The surface morphology of the electrodeposited foams is shown in Figure 2.5.1. All the deposits showed the open porous foam structure with the spherical pores of a few hundred micrometers. However, the details of the foam walls are quite different depending on the electrolyte composition. The foam wall, fabricated in the single CuSO_4 electrolyte (0.15 M), exhibited the ramified structure similar to the previous reports [60,61]. The ramified copper had numerous corn-shaped branches (Figure 2.5.1(a)). The addition of SnSO_4 into CuSO_4 electrolyte changed the morphology of foam wall from ramified structure to agglomerated particle structure (Figure 2.5.1(b)). The size of the particles was several hundred nanometers and the phase was a single phase Cu_6Sn_5 (Figure 2.5.2(b)). Thus, the single phase Cu_6Sn_5 was formed in the slightly Sn-rich condition ($\text{CuSO}_4\text{:SnSO}_4=0.1\text{:}0.12$). With further increase of SnSO_4 content ($\text{CuSO}_4\text{:SnSO}_4=0.025\text{:}0.14$ M), the foam wall became dense and was composed

of numerous nano-sized dendrites, which were three-dimensionally interlocked forming porous 3D network structure (Figure 2.5.1(c)). The XRD pattern indicated that the foam was a mixture of Sn and Cu_6Sn_5 (Figure 2.5.2(c)). In the single SnSO_4 electrolyte (0.15 M), similar dendritic structure was obtained, but the foam wall was less dense (Figure 2.5.1(d)). The trunks in the dendrites were of the order of tens of micrometers [62]. As-deposited foam was a crystalline tetragonal β -Sn (Figure 2.5.2(d)). The copper and tin foams were thoroughly investigated in the previous work [60,61] and further study was focused on the Sn/ Cu_6Sn_5 foam with nano-sized dendrites obtained in the electrolyte of $\text{CuSO}_4\text{:SnSO}_4=0.025\text{:}0.14$ M (Figure 2.5.1(c)).

The high magnification SEM image of Sn/ Cu_6Sn_5 foam revealed that the dendrites were relatively small and less straight compared to those of Sn foam (Figure 2.5.3(a)). The length and diameter of the dendrites were approximately 300 and 30 nm, respectively. The surface was irregular (not smooth) and the numerous granular particles were found, which appeared to be embedded or attached to the dendrites. The detailed feature of the dendrites was investigated by TEM after stripping off from the Cu substrate. Consistent with SEM observation, the surface of the dendrites was uneven and wavy (Figure 2.5.3(b)). A close examination of TEM image indicated that the dendrites had the different contrast and the dark colored granular particles were observed inside the dendrites. The

EELS mapping revealed that Sn was distributed throughout the dendrites with a lower intensity in the dark colored granules (Figure 2.5.3(c)). Instead, Cu was present discontinuously and rich in the dark colored particles (Figure 2.5.3(d)). Based on the XRD shown in Figure 2.5.4 and TEM results, it can be inferred that the dark colored granules are Cu_6Sn_5 , which located in the interior of Sn dendrites and the formation of Cu_6Sn_5 alloy during the electrochemical deposition results in the nano-sized $\text{Cu}_6\text{Sn}_5@\text{Sn}$ dendrites with uneven and wavy surface.

To further investigate the formation of $\text{Cu}_6\text{Sn}_5@\text{Sn}$ nanodendrites, the cathodic linear sweep voltammetry (LSV) of the electrodeposition was carried out and the corresponding voltammograms are shown in Figure 2.5.5. The electrode potential was swept from -0.1 to -1.0 V (vs. SCE) at the potential sweep rate of 10 mV s^{-1} . The curve 1 obtained in 0.15 M CuSO_4 electrolyte exhibited a peak at -0.2 V (vs. SCE), which corresponds to the reduction of copper. The curve 2 obtained in 0.15 SnSO_4 electrolyte showed that the reduction of tin started at a potential of approximately -0.55 V (vs. SCE). A comparison of curves 1 and 2 indicates that the current density increased more rapidly in case of tin deposition than in copper deposition as the potential became more negative than -0.65 V (vs. SCE). The curve 3 obtained in the condition for the synthesis of $\text{Cu}_6\text{Sn}_5@\text{Sn}$ nanodendrites ($\text{CuSO}_4:\text{SnSO}_4=0.027:0.15 \text{ M}$) appears to be a combination of curves 2 and 3. The copper reduction peak at -0.23 V (vs. SCE) diminished due to a low CuSO_4

concentration. In the potential range of -0.53~-0.9 V (vs. SCE), slow decrease of current density and short diffusion limited plateau were observed, indicating that tin reduction and Cu_6Sn_5 formation occurred simultaneously. As further increasing CuSO_4 concentration in electrolyte, two reduction peaks at -0.23 and -0.55 V (vs. SCE) and long diffusion limited plateau from -0.55 to -0.9 V (vs. SCE) were observed in the electrolyte of $\text{CuSO}_4\text{:SnSO}_4=0.125\text{:}0.15$ M (curve 4) where a single phase Cu_6Sn_5 alloy was formed.

The XRD patterns showed that Sn, Cu_6Sn_5 , and $\text{Cu}_{20}\text{Sn}_{10}$ phases were formed at -0.55 V (vs. SCE) and they were completely transformed into Cu_6Sn_5 phase at -0.78 V (vs. SCE) when deposited in the electrolyte of $\text{CuSO}_4\text{:SnSO}_4=0.125\text{:}0.15$ M for 3 min (Figure 2.5.6(a, b)). Thus, the plateau in the range from -0.55 to -0.9 V (vs. SCE) is attributed to the formation of Cu_6Sn_5 . It can be inferred that the Cu_6Sn_5 formation leads to lower the current density (less negative) and slow down the deposition rate. (Figure 2.5.7) Both Sn and Cu_6Sn_5 phases were detected in the foams deposited at -0.53 and -0.78 V (vs. SCE) for 3 min, but the peak intensity for Sn increased at -0.78 V (vs. SCE) largely increased. (Figure 2.5.6(c, d)) Also, the EDS spectra showed that the increased amount of Sn was present in the foam deposited at -0.78 V (vs. SCE) from 64 to 88 wt. %. (Figure 2.5.8) At the applied potential of -0.78 V (vs. SCE), the current density increased more rapidly and thus, the deposition rate was faster in the electrolyte for curve 3 than that for curve 4.

(Figure 2.5.7) This means that the formation of Cu_6Sn_5 alloy leads to slower deposition rate and the growth of Sn dendrite was controlled by the embedment of Cu_6Sn_5 alloy during co-electrodeposition of Sn and Cu.

2.5.2.2 Synthesis of SnO_2/CuO nano-hybrid foams and their gas sensing properties

The open porous foams were formed during electrodeposition on Si/ SiO_2 substrate (Figure 2.5.9) and the pore diameter was 50~100 μm . The foam wall was composed of numerous dendrites, which were three-dimensionally interlocked forming 3D network structure (Figure 2.5.9(a)). The length and diameter of the dendrites were 300~400 and 30~50 nm, respectively. The overall morphology was similar to the Sn foams fabricated in the similar condition [63], but the size of the dendrites was much smaller and less straight. Thus, the electrodeposition in the presence of Cu precursor yielded more dendrites (higher number density) with a short length and produced much denser foam wall. The ratio of Cu/Sn in the foam determined by EDS was 0.18 in wt. %. The morphology of the oxide foam after thermal oxidation at 700 $^\circ\text{C}$ for 1 h is shown in Figure 2.5.9(c). The macro-porous structure was unchanged during heat treatment, and the pore size and shape remained almost same. A slow heating rate of 1 $^\circ\text{C}/\text{min}$ permits to grow a thin supporting oxide surface layer before melting and convert into the corresponding oxide foam without losing the structural

integrity [64]. The dendritic structure in the pore wall was also preserved (Figure 2.5.9(d)), and the dendrites became slightly thicker due to oxidation. The high magnification STEM image shows that the individual dendrite had the wavy surface due to uneven oxidation and sintering, and there were bright-colored spots (high atomic number) (Figure 2.5.9(e)). The EDS mapping indicates that both Sn and Cu were concentrated on those spots, but both elements were found throughout the dendrite (Figure 2.5.9(f, g)). The dendrite was a nano-hybrid of tin oxide and copper oxide, but the nature of nano-hybrid is still under investigation.

The phase changes during thermal oxidation of Sn-Cu foams are shown in Figure 2.5.10. As-synthesized foams were the mixture of crystalline Sn and Cu_6Sn_5 (Figure 2.5.10(a)), and thus, Cu was present in the alloy form. After annealing at 700 °C, tin oxide (SnO_2) and copper oxide (CuO) were formed, but Cu_6Sn_5 was still remained. It was reported that Sn foams were completely oxidized into SnO_2 above 600 °C through intermediate oxidation states (Figure 2.5.10(b)) [64,65]

The response transient of SnO_2/CuO nano-hybrid foam sensor toward H_2S at 250 °C is shown in Figure 2.5.11(a). Upon injecting the 20 ppm H_2S gas, the resistance of the sensor decreased by more than two orders of magnitude, and it slowly recovered with exposure to air, exhibiting a typical n-type semiconductor sensing behavior. The foam sensor showed a stable response down to 4 ppm H_2S ,

and the magnitude of the gas response (S) decreased linearly with decreasing the H_2S concentration. The foam sensor responded to H_2S in the temperature range of 150~400 °C (Figure 2.5.11(b)) and showed a typical temperature dependence of gas response as a semiconductor-type gas sensor [66]. The maximum gas response ($S=574$) toward 20 ppm H_2S was observed at 250 °C. The observed magnitude of gas response was the comparable to that reported previously [67-69]. The long-term stability of SnO_2/CuO nano-hybrid foam sensor was examined by repeating the sensing measurement at 250 °C (Figure 2.5.11(c)). The resistance in air decreased slightly during the first several cycles, but the sensing signal became stable and reversible afterwards. Thus, the foam sensor exhibited the quite stable sensing behavior over cycles. In case of Sn dendrites structure without Cu, the diameter of dendrite branch was approximately 1 μm with 7 m^2/g of Brunauer-Emmett-Teller (BET) surface area [65] and its value of gas response was below 3 in the range of 200~400 °C in H_2S of 20ppm. Although the nanodendrite Sn-Cu alloy exhibited higher surface area of 11 m^2/g , it is thought that the heterostructuring with CuO is dominant factor in terms of lowering optimum temperature and the enhanced value of gas response.

The gas responses of SnO_2/CuO nano-hybrid foam sensor toward 20 ppm of H_2 , CO, NH_3 , NO_x , CH_5OH , and H_2S were compared at 250 °C (Figure 2.5.12). The foam sensor responded to all the gases investigated, but the magnitude of gas

response (S) toward H_2 , CO , NH_3 , NO_x , and CH_3OH was significantly (two orders of magnitude) lower than that for H_2S (Figure 2.5.12(a)). Thus, the foam sensor exhibited the remarkably higher selectivity toward H_2S . The enhanced sensitivity and selectivity toward H_2S gas in SnO_2/CuO nano-hybrid foam sensor can be understood in terms of high surface area, formation of resistive p-CuO/n- SnO_2 junction, and disruption of resistive junction by the sulfurization of CuO into metallic conductor CuS upon exposure to H_2S [62,66]. The response time ($t_{90\%}$) toward H_2S was short compared to the other gases (Figure 2.5.12(b)), but the overall gas response was relatively long, which can be attributed to the large electrode gap (6 mm) in the present sensor and relatively low operating temperature. The large electrode gap was used to minimize the Pt catalyst effect in gas sensing properties. [70]

2.5.3. Conclusion

The branch diameter of wall structures in electro-deposited foam has been successfully controlled below 50nm with adding a small amount of copper element in electrolyte for tin deposition leading to form Cu_6Sn_5 alloy during Sn deposition. This represents a novel way of generating porous dendrite structures with even finer branches with nano-scale diameter. It is confirmed that Cu_6Sn_5 alloy is located inside of Sn nanodendrite branches and it was proposed that the alloy phase formation in co-electrodeposition leads to control the deposition

kinetics effectively and generate size-down to nanoscale. The heat treatment with a slow heating rate converted from metal into CuO/SnO₂ foam preserving the integrity and pore structure. A gas sensor was fabricated using the porous nano-dendrites CuO/SnO₂ foam and the sensor exhibited superior gas sensing performance toward H₂S with high gas response and fast gas reaction compared to other gases. This selective detection is understood in the frame of the advantage of nanostructure and the chemical reaction between H₂S and CuO and the behavior related on p-n junction.

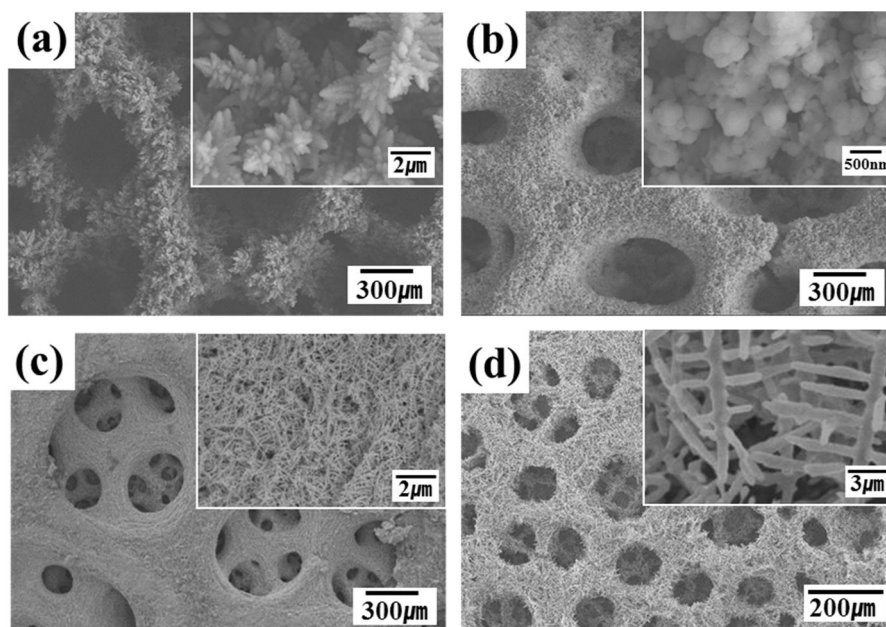


Figure 2.5.1 Surface morphology of porous foams electrodeposited in 1.5M H₂SO₄ electrolyte of different composition; (a) 0.15 M CuSO₄ • 5H₂O, (b) 0.1 M CuSO₄ • 5H₂O, 0.12 M SnSO₄, (c) 0.025 M CuSO₄ • 5H₂O, 0.14 M SnSO₄, (d) 0.15 M SnSO₄

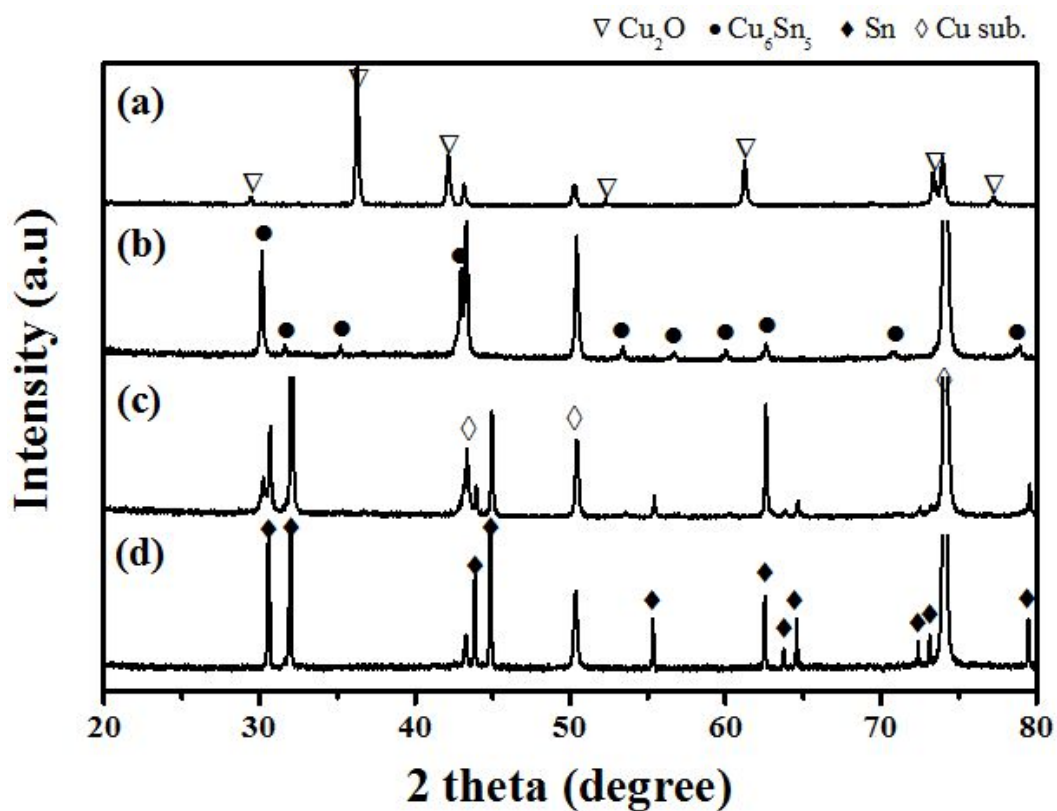


Figure 2.5.2 X-ray diffraction pattern of porous foams electrodeposited in 1.5M H_2SO_4 electrolyte of different composition; (a) 0.15 M $\text{CuSO}_4 \cdot 5\text{H}_2\text{O}$, (b) 0.1 M $\text{CuSO}_4 \cdot 5\text{H}_2\text{O}$, 0.12 M SnSO_4 , (c) 0.025 M $\text{CuSO}_4 \cdot 5\text{H}_2\text{O}$, 0.14 M SnSO_4 , (d) 0.15 M SnSO_4

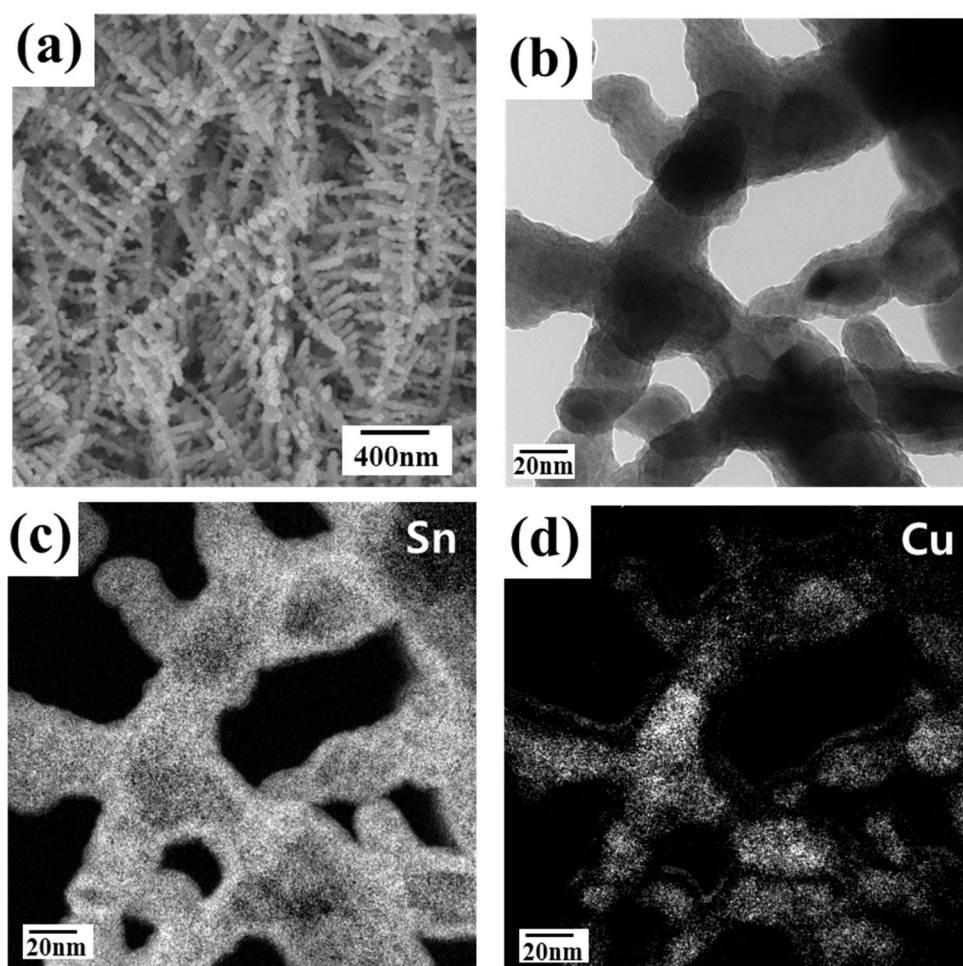


Figure 2.5.3 (a) High magnification image and (b) TEM image of synthesized nanodendrites, (c) tin and (d) copper element mapping images using EELS of (b).

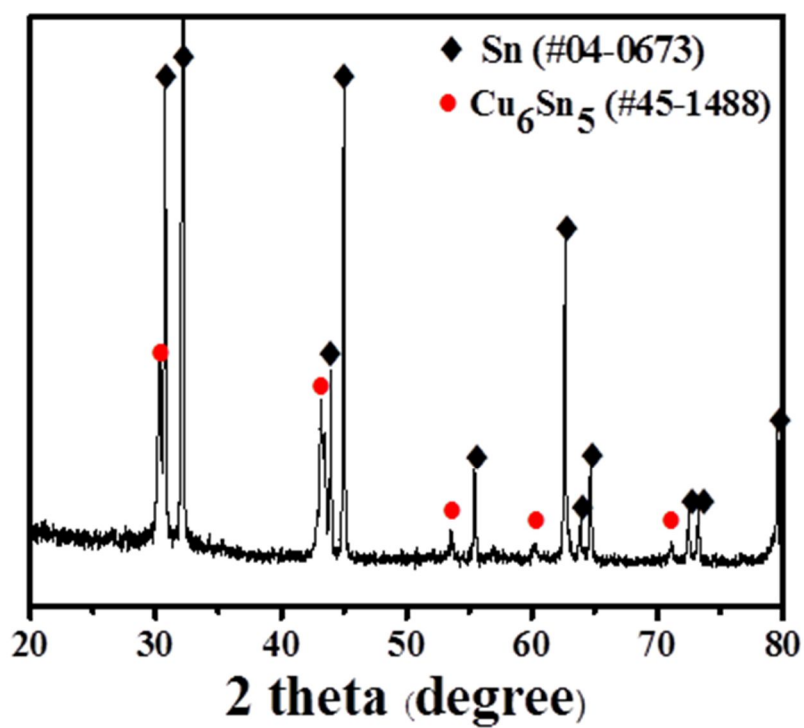


Figure 2.5.4. X-ray diffraction pattern of stripped nanodendrite foam from Cu foil

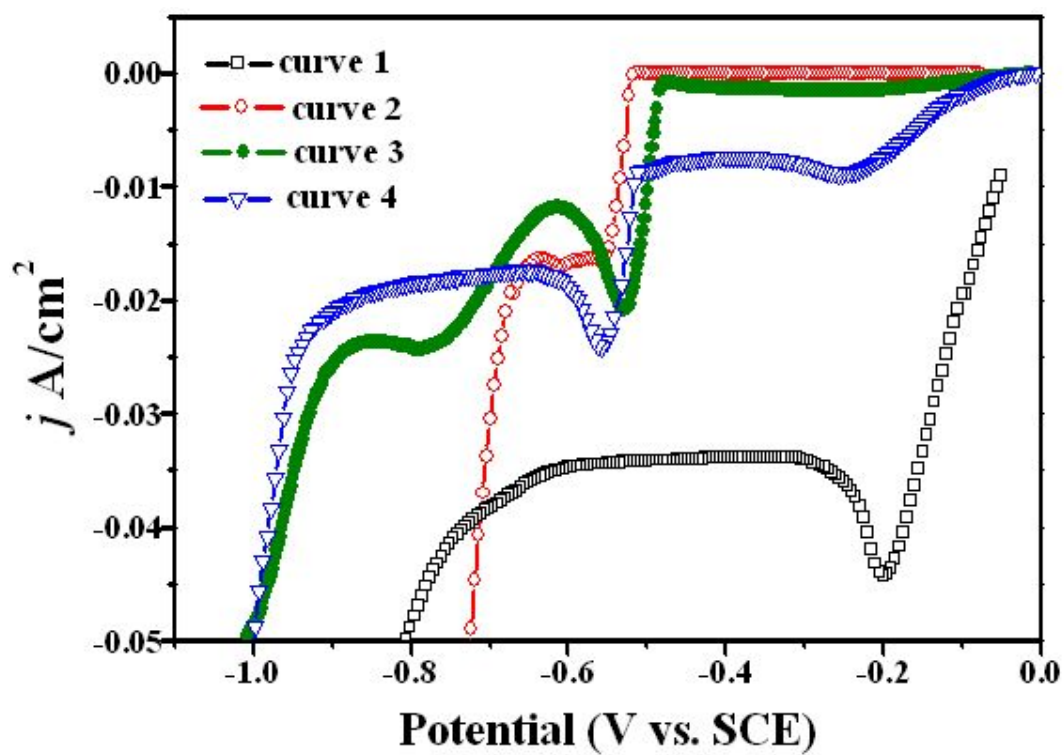


Figure 2.5.5 The cathodic linear sweep voltammetry of electrodeposition in 1.5M H₂SO₄ electrolyte of different composition; (1) curve 1: 0.15 M CuSO₄ · 5H₂O, (2) curve 2: 0.15 M SnSO₄, (3) curve 3: 0.125 M CuSO₄ · 5H₂O, 0.15 M SnSO₄, (4) curve 4: 0.027 M CuSO₄ · 5H₂O, 0.15 M SnSO₄.

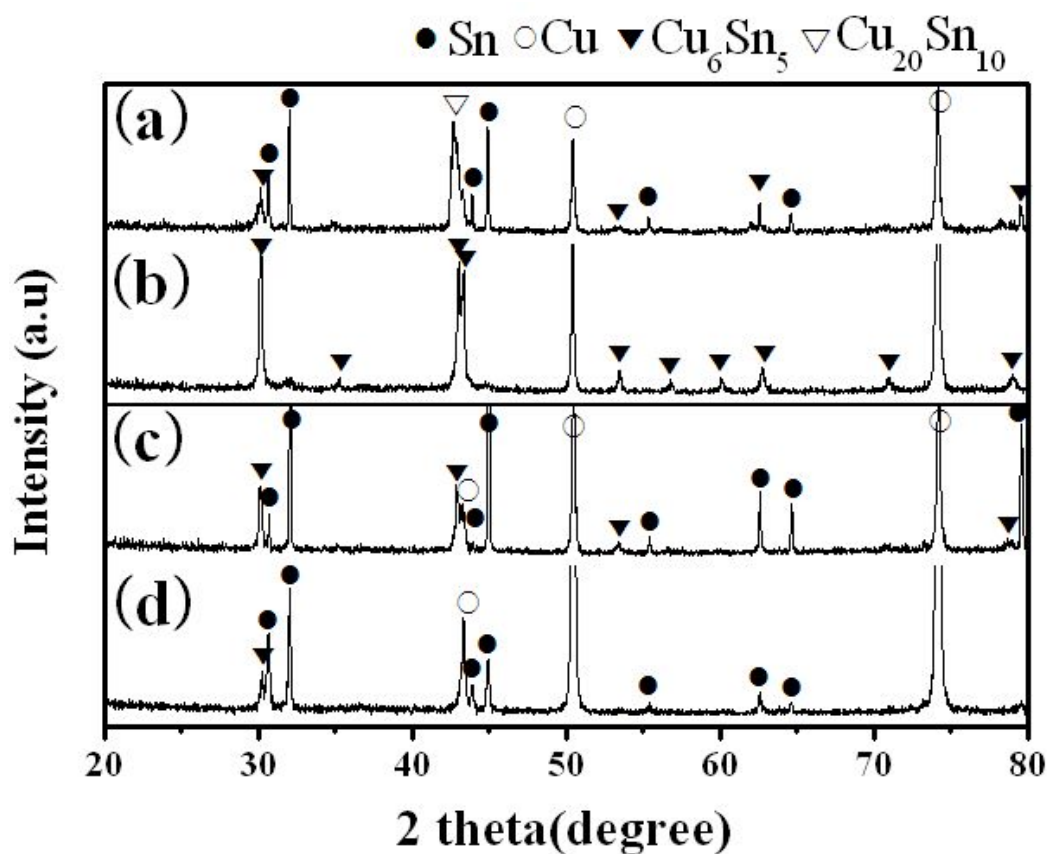


Figure 2.5.6 Phase analysis of deposits synthesized in the electrolyte of different electrolyte composition; 0.125 M CuSO₄ · 5H₂O, 0.15 M SnSO₄ at (a) -0.53V and (b) -0.78V, 0.027 M CuSO₄ · 5H₂O, 0.15 M SnSO₄ at (c) -0.53V and (d) -0.78V.

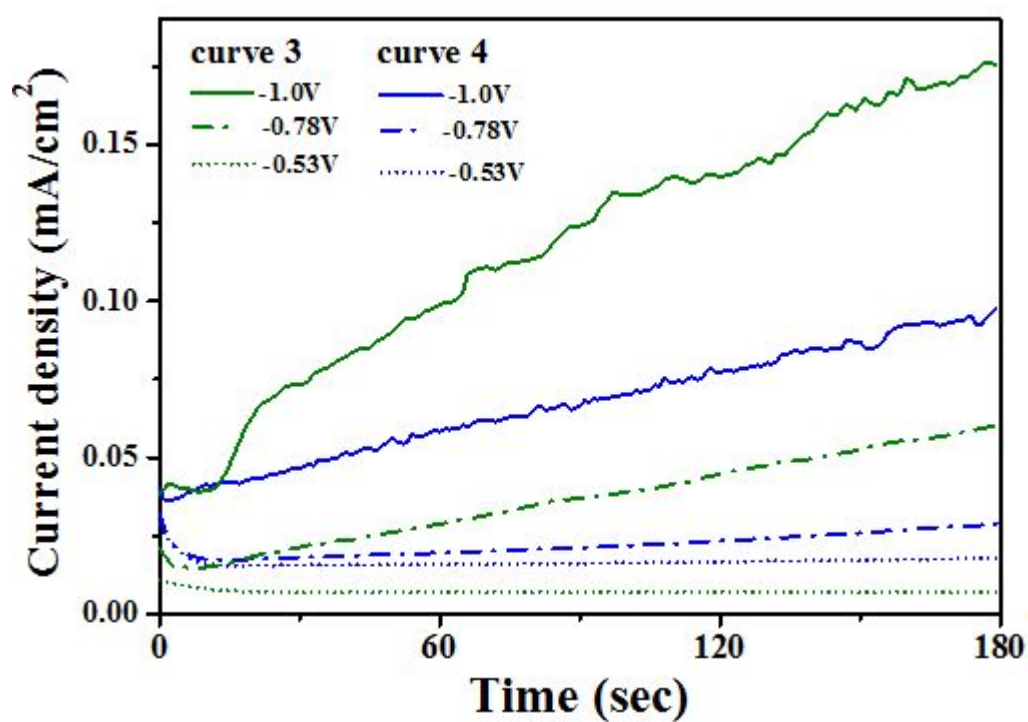


Figure. 2.5.7 Current transient in electrolyte at -0.53, -0.78 and 1 V vs. SCE in different electrolyte composition of curve 3 ($\text{CuSO}_4\text{:SnSO}_4=0.027\text{:}0.15$ M) and curve 4 ($\text{CuSO}_4\text{:SnSO}_4=0.125\text{:}0.15$ M)

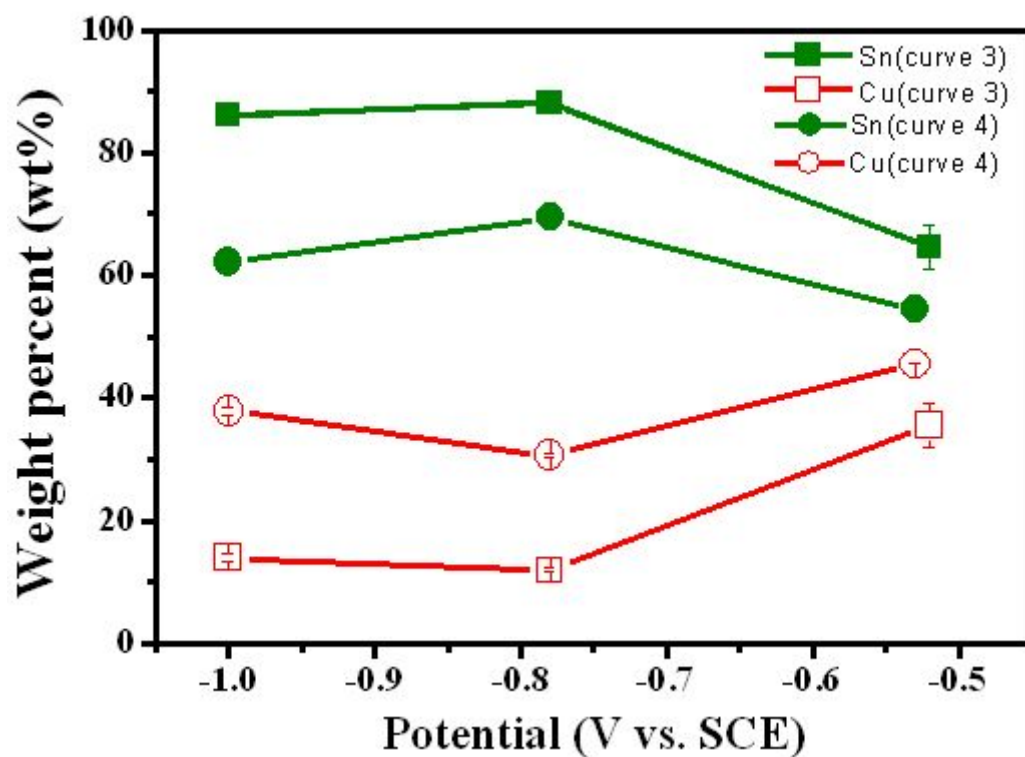


Figure 2.5.8 EDS spectra of synthesized deposits at -0.53, -0.78 and 1 V vs. SCE in different electrolyte composition of curve 3 ($\text{CuSO}_4\text{:SnSO}_4=0.027\text{:}0.15$ M) and curve 4 ($\text{CuSO}_4\text{:SnSO}_4=0.125\text{:}0.15$ M)

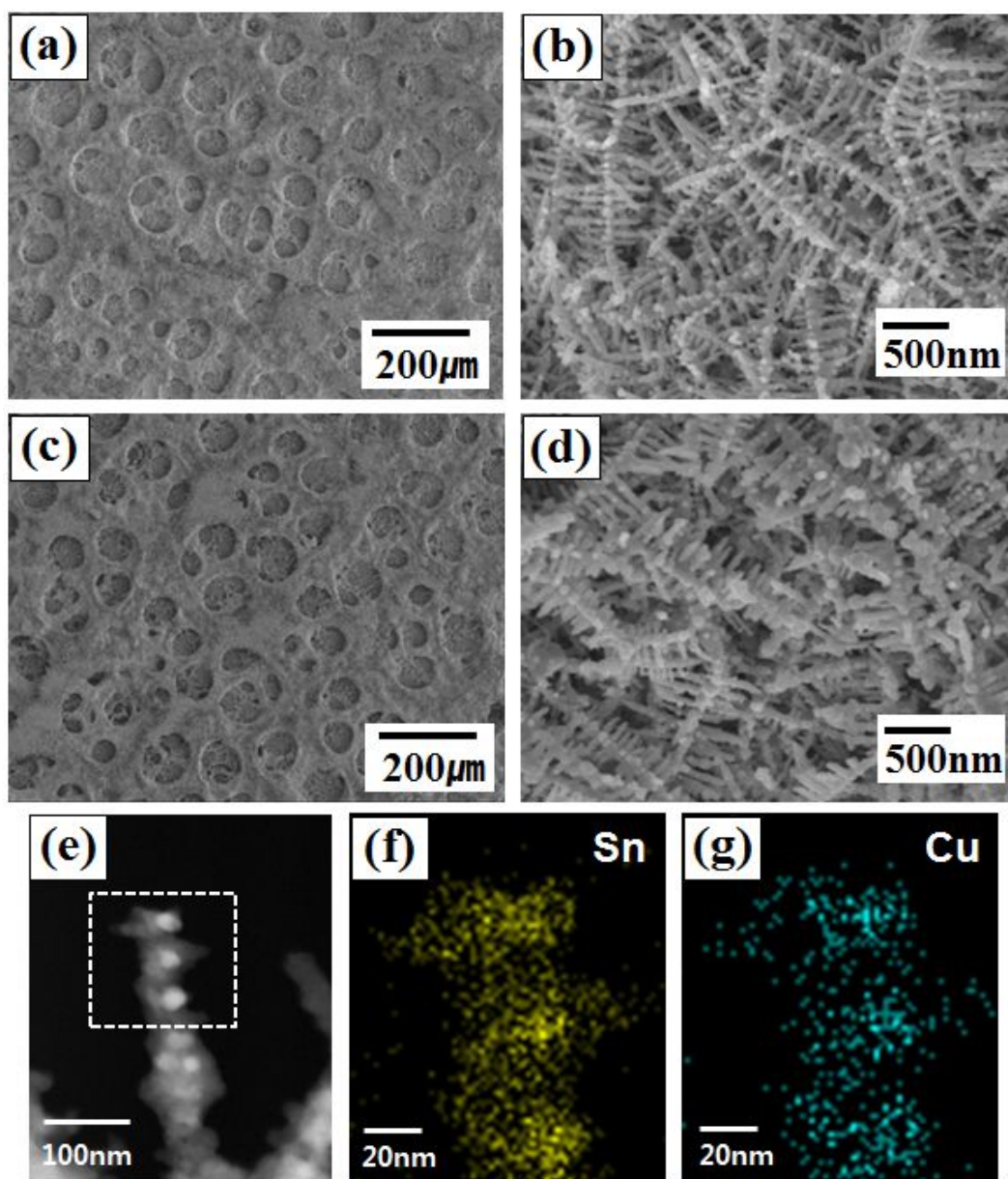


Figure 2.5.9 SEM micrographs of the as-synthesized deposits on SiO₂/Si substrate by (a, b) electrochemical deposition, (c, d) the as-annealed films and (e~g) its STEM images with EDS mapping.

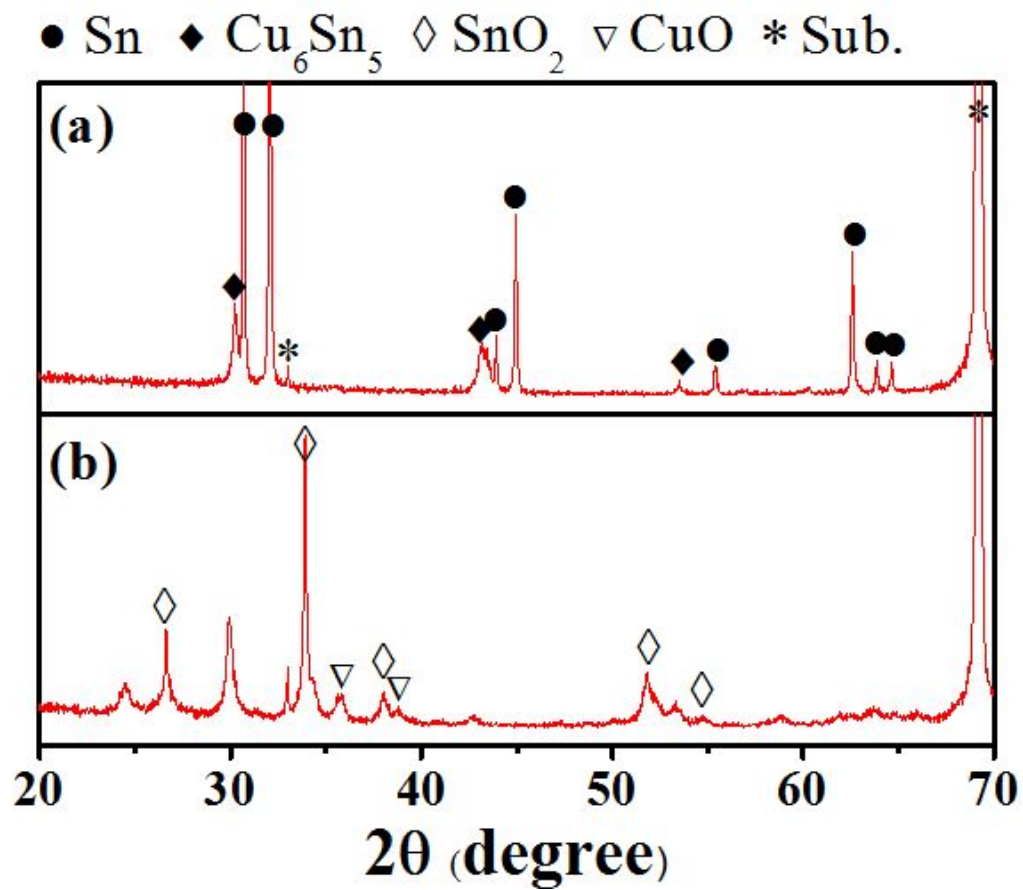


Figure 2.5.10 XRD patterns of Sn foams; (a) the as-deposited and (b) the heat treated at 700 °C.

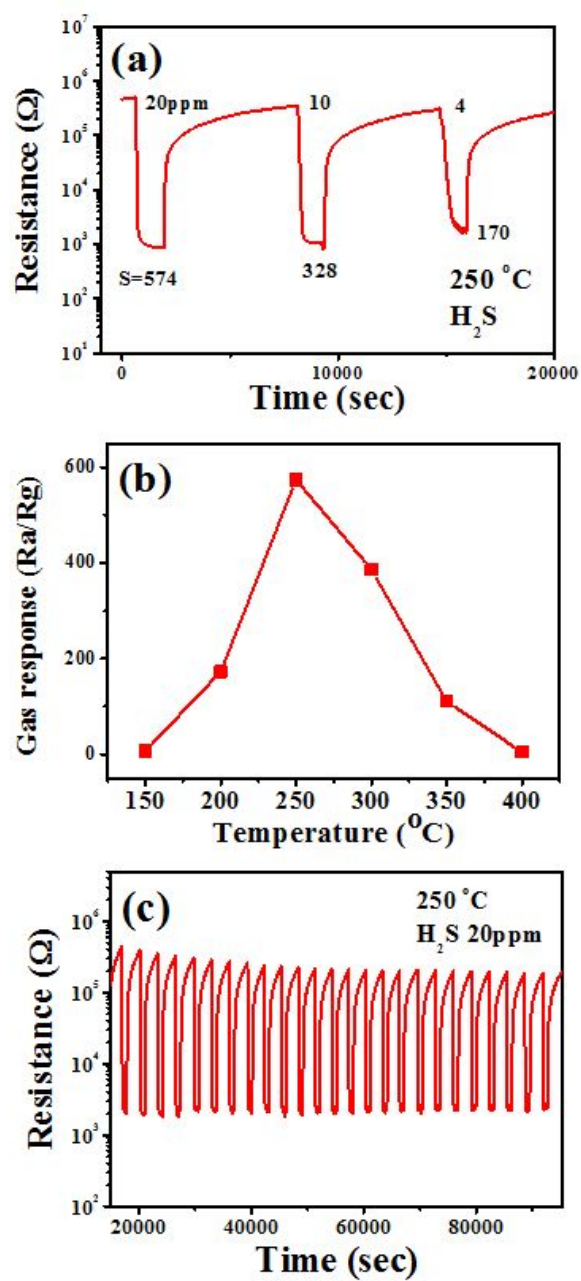


Figure 2.5.11 (a) Gas sensing transient of CuO/SnO₂ porous form, (b) gas response according to operating temperature and the long-term stability of gas sensing performance (c).

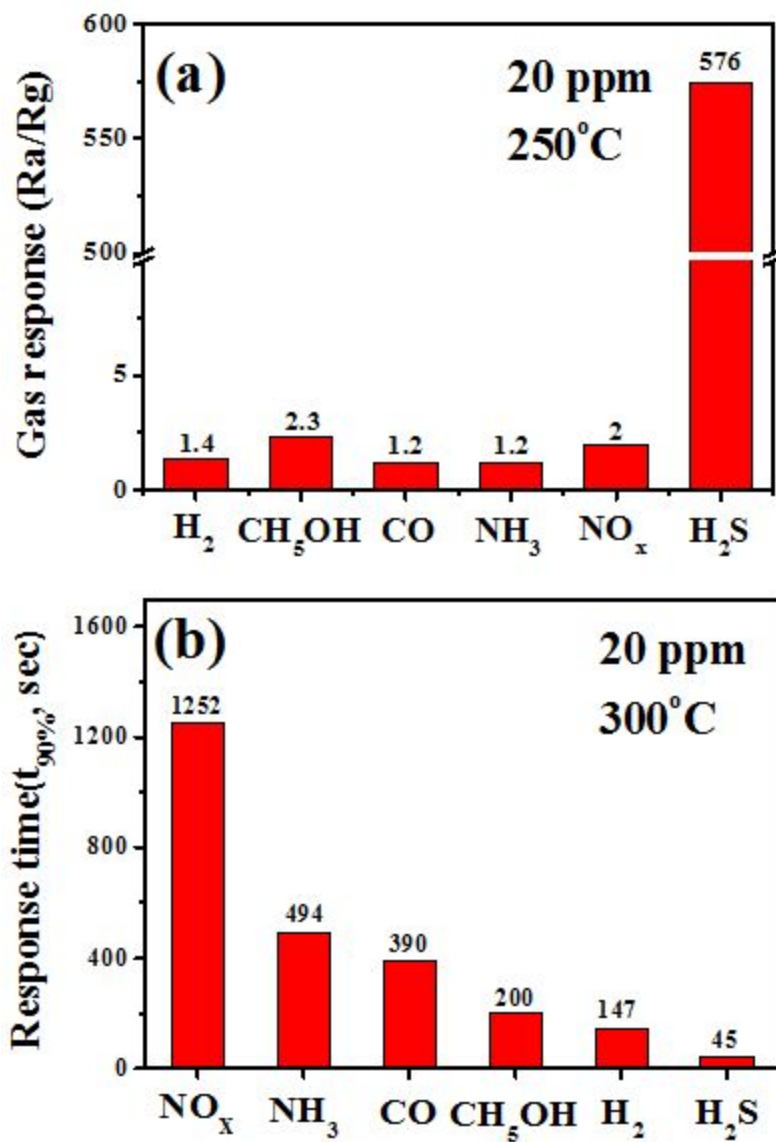


Figure 2.5.12 The comparison of gas sensing performance with other gases: (a) Gas response (Ra/Rg), (b) Response time (t_{90%}).

2.6 Reference

1. K. Ihokura and J. Watson, *The Stannic Oxide Gas Sensor-Principles and Applications*, p. 49-89, CRC Press, Boca Raton, FL (1994).
2. N. Yamazoe, *Sens. Actuators B* 5 (1991) 7.
3. W. Gödel and K. D. Schierbaum, *Sens. Actuators B* 26 (1995) 1.
4. N. Yamazoe and K. Shimano, *Sens. Actuators B* 128 (2008) 566.
5. Y.-H. Choi, M. Yang, and S.-H. Hong, *Sens. Actuators B* 134 (2008) 117.
6. W. Zhu, W. Wang, H. Xu, and J. Shi, *Mater. Chem. Phys.* 99 (2006) 127.
7. Z. R. Dai, Z. W. Pan, and Z. L. Wang, *Solid State Commun* 118 (2001) 351.
8. Z. R. Dai, Z. W. Pan, and Z. L. Wang, *J. Am. Chem. Soc.* 124 (2002) 8673.
9. N. V. Hieu, H. R. Kim, B. K. Ju, and J. H. Lee, *Sens. Actuators B* 133 (2008) 228.
10. B. Pal, M. Sharon, *Mater. Chem. Phys.* 76 (2002) 82.
11. S. Shingubara, *J. Nanoparticle Res.* 5 (2003) 17-30.
12. M.O. Abou-Helal, W.T. Seeber, *Appl. Surf. Sci.* 195 (2002) 53-62.
13. Z. Jin, H. J. Zhou, Z. L. Jin, R. F. Savinell, and C. C. Lin, *Sens. Actuators*

- B* 52 (1998) 188.
- 14 L. R. B. Santos, S. H. Pulcinelli, and C. V. Santilli, *J. Sol-Gel Sci. Technol.* 8 (1997) 477.
 - 15 L. Yuan, Z. P. Guo, K. Konstantinov, H. K. Liu, and S. X. Dou, *J. Power Sources* 159 (2006) 345.
 - 16 G. D. Sulka, S. Stroobants, V. Moshchalkov, G. Borghs, and J. P. Celis, *J. Electrochem. Soc.* 149 (2002) D97.
 - 17 S. J. Kim and J. S. Choi, *Electrochem. Commun.* 10 (2008) 175.
 - 18 Y. K. Jun, H. S. Kim, J. H. Lee, and S. H. Hong, *Sens. Actuators B* 120 (2006) 69.
 - 19 W. H. Song, H. S. Ryu, and S. H. Hong, *J. Am. Chem. Soc.* 88 (2005) 2642.
 - 20 J. Yan, G. V. Ramma Rao, M. Barela, D. A. Brevnov, Y. Jiang, H. Xu, G. P. Lopez, and P. B. Atanassov, *Adv. Mater.* 15 (2003) 23.
 - 21 H. C. Shin, J. Dong, and M. Liu, *Adv. Mater.* 16 (2004) 237.
 - 22 H.T. Chen, S.J. Xiong, X.L. Wu, J. Zhu, J.C. Shen, *Nano Lett.* 9 (2009) 1926.
 - 23 J.M. Wu, C.H Kuo, *Thin Solid Films* 517 (2009) 3870.

- 24 Jr H. He, T.H. Wu, C.L. Hsin, K.M. Li, L.J. Chen, Y.L. Chueh, L.J. Chou, Z.L. Wang, *small* 2 (2006) 116.
- 25 E.N. Dattoli, Q. Wan, W. Guo, Y. Chen, X. Pan, W. Lu, *Nano lett.* 7 (2007) 2463.
- 26 S. Chappel, S.G. Chen, A. Zaban, *Langmuir* 18 (2002) 3336.
- 27 S. Gubbala, V. Chakrapani, V. Kumar, M.K. Sunkara, *Adv. Funct. Mater.* 18 (2008) 2411.
- 28 Y. Idota, T. Kubota, A. Matsufuji, Y. Maekawa, T. Miyasaka, *Science* 276 (1997) 1395.
- 29 W. Zhu, W. Wang, H. Xu, J. Shi, *Mater. Chem. Phys.* 99 (2006) 127.
- 30 W. Lee, R. Ji, U. Gösele, K. Nielsch, *Nature* 439 (2006) 741.
- 31 H. Masuda, K. Fukuda, *Science* 268 (1995) 1446.
- 32 H. C. Shin, J. Dong, and M. Liu, *Adv. Mater.* 16 (2004) 237.
- 33 L. Young, *Anodic Oxide Films*, p. 326, Academic Press, London, New York (1961).

- 34 I.S. Hwang, J.K. Choi, S.J. Kim, K.Y. Dong, J.H. Kwon, B.K. Ju, J.H. Lee, *Sens. Actuators B* 142 (2009) 105.
- 35 J. Tamaki, T. Maekawa, N. Miura, N. Yamazoe, *Sens. Actuators B* 9 (1992) 197.
- 36 G. Sarala Devi, S. Manorama, V.J. Rao, *Sens. Actuators B* 28 (1995) 31.
- 37 J. Tamaki, T. Maekawa, N. Miura, N. Yamazoe, *Sens. Actuators B* 9 (1992) 197.
- 38 G. Sarala Devi, S. Manorama, V.J. Rao, *Sens. Actuators B* 28 (1995) 31.
- 39 A. Chowdhuri, P. Sharma, V. Gupta, K. Sreenivas, *J. Appl. Phys.* 92 (2002) 2172.
- 40 X. Kong, Y. Li, *Sens. Actuators B* 105 (2005) 449.
- 41 L.A. Patil, D.R. Patil, *Sens. Actuators B* 120 (2006) 316.
- 42 M.S. Wagh, L.A. Patil, T. Seth, D.P. Amalnerkar, *Mater. Chem. Phys.* 84 (2004) 228.
- 43 Y. Shimizu, A. Jono, T. Hyodo, M. Egashira, *Sens. Actuators B* 108 (2005) 56.

- 44 X. Zhou, Q. Cao, H. Huang, P. Yang, Y. Hu, *Mater. Sci. Eng. B* 99 (2003) 44.
- 45 J.F. Moulder, W.F. Stickle, P.E. Sobol, K.D. Bomben, Handbook of X-ray photoelectron spectroscopy: A reference book of standard spectra for identification and interpretation of XPS data, Physical Electronics, Minnesota (1995).
- 46 K.I Choi, H.R Kim, J.Heun Lee, *Sens. Actuators B* 138 (2009) 497.
- 47 W. Huang, L. Fu, Y. Yang, S. Hu, C. Li, Z. Li, *Electrochem. Solid-State Lett.* 8 (2005) C166.
- 48 A. Kolmakov, Y. Zhang, M. Moskovits, *Nano lett.* 3 (2003) 1125.
- 49 M.H Xu, F.S Cai, J. Yin, Z.H Yuan, L.J Bie, *Sens. Actuators B* 145 (2010) 875.
- 50 Y. Zhang, X. He, J. Li, Z. Miao, F. Huang, *Sens. Actuators B* 132 (2008) 67.
- 51 Y. Zhang, J. Li, G. An, X. He, *Sens. Actuators B* 144 (2010) 43.

- 52 N.V. Hieu, H.R. Kim, B.K. Ju, J.H. Lee, *Sens. Actuators B* 133 (2008) 228.
- 53 Z. Pan, Z.L. Wang, *Appl. Phys. Lett.* 81 (2002) 1869.
- 54 J. Huang, K. Yua, C. Gua, M. Zhaia, Y. Wua, M. Yang, J. Liu, *Sens. Actuators B* 147 (2010) 467.
- 55 J.P. Ge, J. Wang, H.X. Zhang, X. Wang, Q. Peng, Y.D. Li, *Sens. Actuators B* 113 (2006) 937.
- 56 G. Neri, A. Bonavita, G. Micali, N. Donato, F.A. Deorsola, P. Mossino, I. Amato, B. D. Benedetti, *Sens. Actuators B* 117 (2006) 196.
- 57 M.H Xu, F.S Cai, J. Yin, Z.H Yuan, L.J Bie, *Sens. Actuators B* 145 (2010) 875.
- 58 S.G. Ansari, P. Boroojerdian, S.R. Sainkar, R.N. Karekar, R.C. Aiyyer, S.K. Kulkarni, *Thin Solid Films*, 295 (1997) 271.
- 59 Y. Liu, E. Koep, M. Liu, *Chem. Mater.* 17 (2005) 3997.
- 60 H.C.Shin, J. Dong, M. Liu, *Adv. Mater.* 15 (2003) 1610.

- 61 Y. Li, W. Z. Jia, Y. Y. Song, X. H. Xia, *Chem. Mater.*, 19 (2007) 5758.
- 62 J.H. Jeun, D.H. Kim, S.H. Hong, *Sens. Actuators B* 161 (2012) 784.
- 63 H. C. Shin, M. Liu, *Adv. Funct. Mater.* 15 (2005) 582.
- 64 A. Kolmakov, Y. Zhang, M. Moskovits, *Nano Lett.* 3 (2003) 1125.
- 65 J.H. Jeun, D.H. Kim, S.H. Hong, *Sens. Actuators B* 161 (2012) 784.
- 66 R.B. Vasiliev, M.N. Rumyantseva, N.V. Yakovlev, A.M. Gaskov, *Sens. Actuators B* 50 (1998) 186.
- 67 J. Tamaki, K. Shimano, Y. Yamada, Y. Yamamoto, N. Mirua, N. Yamazoe, *Sens. Actuators B* 49 (1998) 121.
- 68 I.S. Hwang, J.K. Choi, S.J. Kim, K.Y. Dong, J.H. Kwon, B.K. Ju, J.H. Lee, *Sens. Actuators B* 142 (2009) 105.
- 69 J.M. Lee, B.U. Moon, C.H. Shim, B.C. Kim, M.B. Lee, D.D. Lee, J.H. Lee, *Sens. Actuators B* 108 (2005) 84.
- 70 X. Xue, Z. Chen, C. Ma, L. Xing, Y. Chen, Y. Wang, T. Wang, *J. Phys. Chem. C* 114 (2010) 3968.

Chapter 3.

Heterostructured nanotube of SnO₂ and TiO₂ for Li ion Battery Application

3.1. Introduction

The technical needs for large reversible capacity and high functionality of lithium ion batteries (LIBs) has increased in wide range, from hybrid electric vehicles (HEVs) to portable electronic devices.[1-3] In general, graphite-based materials are commercially used as an anode, which its theoretical capacity is relatively low, 372 mA g^{-1} . [4] In this manner, a lot of attention have been attracted for alternative high capacity anode materials such as Si, Sn-based materials.[5-7] Among various candidates, SnO_2 has been considered as a promising anode material due to its high capacity and low reactivity with electrolyte.[8,9] However, a large and uneven volume expansion up to 300 % occurs during lithium insertion/extraction (reaction: $\text{SnO}_2 + x\text{Li}^+ + xe^- \leftrightarrow \text{Li}_x\text{Sn} + \text{Li}_2\text{O}$), which causes a pulverization and electrical connectivity loss. As a result, a fast capacity fading is observed in SnO_2 electrode.

To solve this problem, nanoporous structure with a high surface to volume ratio such as nanotubes, hollow sphere can prevent from aggregating particles, making diffusion of electrolyte difficult within aggregates.[10-13]

The applying nanoporous structures to anode materials would shorten the diffusion length of Li ions further and thus lead to fast high-rate performance. In addition, inner free surface can make mechanical stress accommodated.

Among them, nanotube is the most promising structure for anode electrode of LIBs because inner free space of nanotube can accommodate the large volume expansion without a pulverization of electrical pathway, significant advantage for an enhanced rate capability. Its inner space can release mechanical stress then structural stability can be obtained.[14-16] Recently, the electrochemical performance of SnO₂ hollow structures have been intensively investigated, and these structures showed the enhanced cycling performance compared to that of SnO₂ nanoparticles.[24-31] However, capacity fading still remain a critical problem for the practical implementation.

To overcome this limitation of SnO₂ materials anode, technical approach is a heterostructuring with other structurally stable anode materials in order to obtain a stable cycle electrochemical performance. Among various metal oxides for heterostructuring with SnO₂, TiO₂ is considered as one of appropriate materials.

In order to meet the requirement on environmental benignity, availability and safety, the employment of titanium dioxide (TiO₂) as anode materials of LIBs is more benefits over the conventional anode materials to achieve higher safety and stability.[25] The volume change of TiO₂ is less than 4% during the formation of typical Li-ion intercalation compound in the reaction: $\text{TiO}_2 + x\text{Li}^+ + xe^- \leftrightarrow \text{Li}_x\text{TiO}_2$ ($0 \leq x \leq 1$), which thus greatly improves the overall safety of battery and this structural stability enable outstanding faster charge/discharge properties

at high C-rate.[25-28] In addition, the operating voltage of TiO₂ is relatively high (1.5-1.8 V verse Li/Li⁺) therefore the formation of solid-electrolyte interface (SEI) layer on the surface of anode can be effectively avoided due to such a high operating voltage.[27,29] However, less energy is generated than the reported maximum practical capacity of TiO₂ was approximately 150~170 mA hg⁻¹ and lower than currently used graphite.[26-30] This low capacity is originated from the poor electrical conductivity and low diffusion coefficient of Li-ion in TiO₂ ($\sim 1 \times 10^{-12}$ S m⁻¹) thus the advancement of TiO₂ as anode materials is severely restricted.[29] In recent decades, one widely practiced strategy to overcome this drawback of TiO₂ based anodes is the utilization of various TiO₂ nanostructures and many researches related on those have been intensely conducted.[28,31-33]

SnO₂/TiO₂ double shell nanotube have been recently suggested to overcome the demerits of both materials, and to improve the electrode performance.[33-40] TiO₂ encapsulation can effectively maintain the mechanical integrity of SnO₂ during the reaction with Li ions while the low specific capacity of TiO₂ can be compensated by the high capacity of SnO₂. SnO₂ nanoparticles encapsulated with TiO₂ have been considered most frequently.[33-35,39,40] Although a nanotubar hollow type is more suitable for accommodating volume expansion and thus enabling better cycle performance than the nanoparticle type,[41, 42] studies on SnO₂ nanotubes encapsulated with TiO₂ for LIB anode has been very limited.

In $\text{SnO}_2@\text{TiO}_2$ double-shell nanotube, a TiO_2 outer shell can encapsulate the SnO_2 inner nanotube, allowing the structural integrity to be maintained. The large internal stresses caused by volume expansion of SnO_2 during Li-ion charge/discharge can also be accommodated through the sufficient inner space of the nanotube.

In this study, $\text{SnO}_2\text{-TiO}_2$ multi-layer nanotubes were fabricated by utilizing electrospinning and atomic layer deposition (ALD). Polyacrylonitrile (PAN) is chosen as an electrospinning material, and as-electrospun PAN nanofiber is used as a template for the nanotube. The thicknesses of the SnO_2 inner shell and TiO_2 outer shell are precisely controlled in nanoscale. The synthesized products were fabricated to coin-cell for electrochemical test and those enhanced electrochemical properties were confirmed.

3.2 SnO₂@TiO₂ double-shell nanotube and its electrochemical properties

3.2.1. Experimental procedure

Synthesis of SnO₂@TiO₂ double-shell nanotubes

For electrospinning, PAN (Polyacrylonitrile, MW = 200,000 g mol⁻¹, Misui Chemical) was dissolved in dimethylformamide (DMF, purity = 99.5%, Daejung Chemical), and the concentration of the solution was fixed to 15 wt% to produce uniform nanofibers with an average diameter of 200–300 nm. The electrospinning conditions were optimized as follows: applied voltage: 15 kV, tip-to-collector distance: 10 cm, and flow rate of solution: 0.5 ml h⁻¹. The as-electrospun PAN nanofibers were directly collected on a 4-inch silicon wafer for the subsequent SnO₂ and TiO₂ coatings by ALD. The SnO₂ inner shell and TiO₂ outer shell were deposited on the as-electrospun PAN nanofibers by plasma-enhanced atomic layer deposition (PEALD). Dibutyltin diacetate (DBTDA) ((CH₃CO₂)₂Sn [(CH₂)₃–CH₃]₂) was used as the Sn precursor, which was evaporated at 40 °C and transported to the deposition chamber by a 20-sccm Ar (99.99%) gas. Titanium isopropoxide (Ti(OCH(CH₃)₂)₄) was used as the Ti precursor, which was evaporated at room temperature and transported by 10-sccm Ar gas. The 50-sccm O₂ (99.99%) and Ar (99.99%) gases were used as the plasma and purge gases,

respectively. The time sequence for source pulse, first purge, O₂ pulse, plasma pulse, and second purge was 3, 12, 8, 1, and 12 s for SnO₂ deposition and 1, 12, 8, 1, and 12 s for TiO₂ coating, respectively. The deposition was conducted with an RF power of 100 W at 240 mTorr, and the substrate temperature during deposition was maintained at 100 °C to reduce the degradation of PAN nanofibers. The number of ALD cycles for SnO₂ and TiO₂ coatings were 300 and 600, respectively. The SnO₂@TiO₂ double-shell-coated PAN nanofibers were annealed at 700 °C for 1 h to burn out the PAN template and to crystallize the SnO₂ and TiO₂ shells. The detailed fabrication procedures are schematically shown in Fig. 3.2.1.

Characterization

SnO₂@TiO₂ double-shell nanotubes were characterized by field emission scanning electron microscopy (FESEM, Hitachi, S-4800) and transmission electron microscopy (TEM, FEI, Tecnai F20) equipped with energy dispersive spectroscopy (EDS). For electrochemical measurements, the test electrodes consisted of the active powder material (70 wt%), carbon black (Ketchen Black, 10 wt%) as a conducting agent and poly amide imide (PAI, 20 wt%) dissolved in N-methyl pyrrolidinone (NMP) at 60 °C as a binder. Each component was well mixed to form slurry using a magnetic stirrer. The slurry was coated onto a copper foil substrate, pressed, and dried at 200 °C for 4 h under a vacuum. A coin-type

electrochemical cell was used with Li foil as the counter and reference electrodes, and 1 M LiPF₆ in ethylene carbonate (EC)/diethylene carbonate (DEC) (5:5 (v/v), PANAX) was used as the electrolyte. The cell assembly and all of the electrochemical tests were carried out in an Ar-filled glove box. The cycling experiments were galvanostatically performed using a Maccor automated tester at a constant current of 800 and 1500 mA g⁻¹ for the active material within the voltage range between 0.0 and 3.0 V (vs. Li/Li⁺). During the discharging step, Li was inserted into the electrode, while Li was extracted from the electrode during the charge. After the electrochemical measurements, the coin cell was disassembled and washed completely with ethanol for SEM and TEM analyses.

3.2.2. Result and discussion

The as-electrospun PAN nanofibers were connected to each other, forming a self-supporting network (Figure 3.2.2). The PAN nanofibers had a relatively uniform diameter of 200~300 nm with a smooth surface, and their length was more than several tens of micrometers. The nanofiber network was well adhered to the Si substrate, and it was detached from the substrate after annealing at 700 °C. The original arrangement of PAN templates was preserved in the SnO₂@TiO₂ double-shell nanotubes forming the network structure (Figure 3.2.3(a)). The

nanotubes had uniform diameter without structural distortion, demonstrating that the ALD process yielded uniform and conformal $\text{SnO}_2@\text{TiO}_2$ coating on PAN templates. The templates were effectively removed by calcination (inset of Figure 3.2.3(a)) and the thermogravimetric (TG) analysis indicated that no residual carbon was left. Low-magnification TEM image showed the tube-like structure, with bright-colored core free inner space and dark-colored metal oxide shell (Figure 3.2.3(b)). The wall thickness was constant along the entire length of the nanotubes. The STEM image confirmed that the walls of the nanotubes were composed of two shells; bright-colored inner shell with high atomic number and dark-colored outer shell with low atomic number (Figure 3.2.3(c)). The EDS line profiles clearly demonstrated that Sn was present in the inner shell and Ti was located in the outer shell. The two distinct layers with different contrast were observed in the high-magnification TEM image (Figure 3.2.3(d)), and the thicknesses of each layer were ~ 12 and ~ 22 nm. Thus, the fabricated nanotubes had 12 nm-thick inner SnO_2 and 22 nm-thick outer TiO_2 shells. It is noted that the precise thickness control of SnO_2 nanotubes on PAN template by ALD has been demonstrated in a previous study.[43] Also, the shell thickness of TiO_2 nanotubes could be easily controlled and it was 5, 10, and 22 nm for 75, 150, and 300 ALD cycles, respectively (Figure 3.2.4). The TiO_2 shell thickness increased linearly with the number of ALD cycles, and the average growth rate was determined to be ~ 0.07 nm cycle⁻¹. The present study is focused on the TiO_2 nanotubes with the

shell thickness of 22 nm, based on the optimum ratio of Sn to Ti proposed by Park et al.⁴⁴ The spots and rings appeared in the selected area diffraction (SAED) pattern, which was indexed to the rutile phase (inset of Figure 3.2.3(d)). However, the beam size for SAED was larger than the wall thickness of nanotubes, and TiO₂ could not be separated from SnO₂. The high resolution TEM image of the outer shell showed lattice fringes, indicating that TiO₂ was well crystallized (Figure 3.2.3(e)). The X-ray diffraction pattern shown in Figure 3.1.5 clearly indexed to be the mixture phase of rutile SnO₂ and anatase TiO₂.

The atomic ratio of Ti to Sn estimated by the nanotube geometry was 2.1, and the ratio determined by EDS was 2.6. Consequently, crystalline SnO₂@TiO₂ double-shell nanotubes were successfully fabricated by combining PAN nanofiber templates and ALD coating process. For comparison, SnO₂ single-shell nanotubes were fabricated in the same process (Figure 3.2.6). The wall thickness of SnO₂ single-shell nanotubes was ~12 nm after 300 ALD cycles. The nanotubes were crystalline and composed of nanocrystallites similar to the previous report.^[43]

The discharge/charge voltage profile of the SnO₂@TiO₂ double-shell nanotube electrode is illustrated in Figure 3.2.7(a). The cycling experiments were conducted in the voltage range between 0.01 and 3.0 V (vs. Li/Li⁺) at a current density of 800 or 1500 mA g⁻¹. The shape of the voltage profile was very close to that of the typical rutile TiO₂ electrode.^[25,29] At the current density of 800 mA g⁻¹, the initial discharge and charge capacities were 599 and 237 mA h g⁻¹, respectively.

The coulombic efficiency of the first cycle was low (about 40 %), which was due to the irreversible reduction of SnO_2 to Sn and Li_2O . After the first cycle, the discharge and charge capacities rapidly approached the constant value of $\sim 300 \text{ mA h g}^{-1}$ with the Coulombic efficiency of $\sim 97\%$ (Figure 3.2.7(b)). In order to understand the Li-ion charge/discharge reactions, cyclic voltammetry (CV) of the $\text{SnO}_2@\text{TiO}_2$ double-shell nanotubes was conducted at 1 mVs^{-1} , and the ex-situ TEM images and SAED patterns of active anode materials at each potential (points 1~3 in Figure 3.2.7(c)) were shown in Figure 3.2.8. The first cycle curve was different from the second and third ones, possibly due to the formation of solid-electrolyte interface (SEI) and Li_2O . [45,46] At the discharge potential of 0.2 V (point 1), $\text{SnO}_2@\text{TiO}_2$ double-shell nanotube was fully charged and transformed to $\text{Li}_{22}\text{Sn}_5$ and $\text{Li}_{0.5}\text{TiO}_2$ (Figure 3.2.8b). As the charge potential increased, lithium ions were extracted from $\text{Li}_{22}\text{Sn}_5$ to Sn (point 2) and from $\text{Li}_{0.5}\text{TiO}_2$ to TiO_2 (point 3) in sequence (Figure 3.2.8(c, d)). Thus, the reduction/oxidation peak pairs at 0.17 and 0.51 V are attributed to lithium ion alloying/dealloying with SnO_2 , and the small reduction/oxidation peak pairs at 1.72 and 2 V are ascribed to lithium ion insertion/extraction from TiO_2 . [45-48] In addition, the integrity of $\text{SnO}_2@\text{TiO}_2$ nanotube during the discharge/charge process was verified by ex-situ TEM images (Figure 3.2.8). A similar shape of the voltage profile with slightly higher initial discharge and charge capacities was observed in the SnO_2 single-shell nanotube electrode (Figure 3.2.9), but the

reversible capacity continuously decreased during 50 cycles (Figure 3.2.10(a, b)). Interestingly, the $\text{SnO}_2@\text{TiO}_2$ double-shell nanotube electrode exhibited a stable reversible capacity for 50 cycles at both current densities (Figure 3.2.10(a, b)) and the good rate capability was exhibited with the variation of current density. (Figure 3.2.11) In case of TiO_2 single-shell nanotubes with 20 nm thickness, the discharge capacity was ~ 80 and $\sim 25 \text{ mA h g}^{-1}$ at the current density of 800 and 1500 mA g^{-1} , respectively (Figure 3.2.12). It is noted that the double-shell nanotube electrode showed better capacity retention at higher current density. After 50 cycles, the reversible capacities of the $\text{SnO}_2@\text{TiO}_2$ double-shell nanotube electrode were 300 and 200 mA h g^{-1} at the current densities of 800 and 1500 mA g^{-1} , respectively. These capacities were higher than the values observed in the SnO_2 and TiO_2 single-shell nanotube electrodes and the reported practical capacity of TiO_2 ($150\sim 170 \text{ mA h g}^{-1}$). [27-29] We believe that the high capacity of SnO_2 and the superior cycling performance of TiO_2 are synergistically combined in the $\text{SnO}_2@\text{TiO}_2$ double-shell nanotube electrode.

To confirm the structural integrity of the double-shell nanotube electrode during repeated cycling, coin-type half-cells were disassembled in an Ar-filled glove box, and the electrode was observed using SEM and TEM. After 5 cycles at 1500 mA g^{-1} , the initial nanotube morphology of SnO_2 single-shell nanotube electrode was completely lost (Figure 3.2.13(a)). The TEM image showed the agglomerated spherical nano-particles of $50\sim 100 \text{ nm}$ size (Figure 3.2.13 (b)),

which were confirmed to be Sn by EDS (Figure 3.2.14(b)). Similar agglomerated particle morphology was also observed in the 50-cycled SnO_2 single-shell nanotube electrode (Figure 3.2.15(a, b)), supporting that SnO_2 nanotubes were disintegrated into nanoparticles during charging/discharging due to the large volume expansion of SnO_2 . In contrast, $\text{SnO}_2@\text{TiO}_2$ double-shell nanotubes maintained their 1-D structure with conductive carbon particles after 5 cycles without any mechanical degradation, and the morphology was similar to that of the pristine sample (Figure 3.2.13(c, d)). The STEM image further confirmed the hollow nature of the cycled double-shell nanotubes (Figure 3.2.13(e)). The EDS mapping revealed that Ti and Sn were present on the nanotubes (Figure 3.2.13(f, g)). Furthermore, the nanotube morphology was still preserved after 50 cycles (Figure 3.2.15(c, d)). These observations corroborate that rigid TiO_2 encapsulation and hollow inner space are very effective for accommodating the large volume expansion of SnO_2 , which brings about stable cyclability even in the high rate condition.

3.2.3 Conclusion

We have reported on a simple process to fabricate $\text{SnO}_2@\text{TiO}_2$ double-shell nanotubes with a precisely controlled shell thickness. The $\text{SnO}_2@\text{TiO}_2$ double-shell nanotubes was beneficial on the electrochemical performance, as

demonstrated in terms of stable cycling and higher rate performance, suggesting that $\text{SnO}_2@\text{TiO}_2$ nano-sized heterostructure in the nanotubular form can be a solution for robust and fast charge/discharge anode for LIBs.

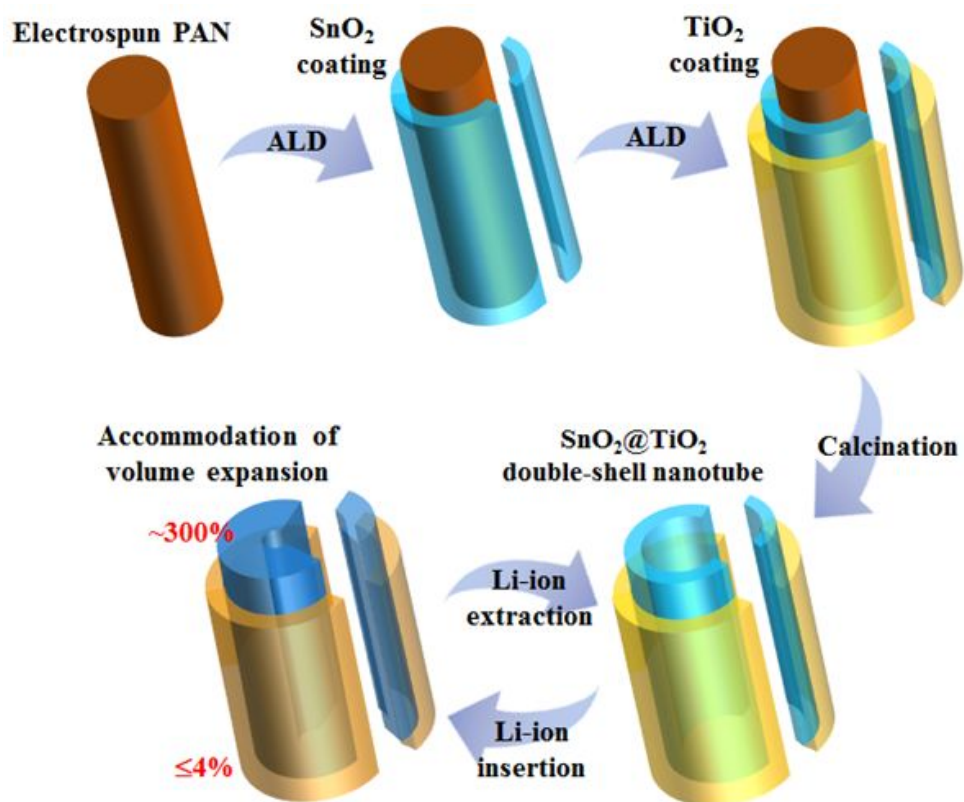


Figure 3.2.1 Schematic diagram of the fabrication procedures and schematic illustration of Li-ion insertion/extraction in $\text{SnO}_2@\text{TiO}_2$ double-shell nanotubes.

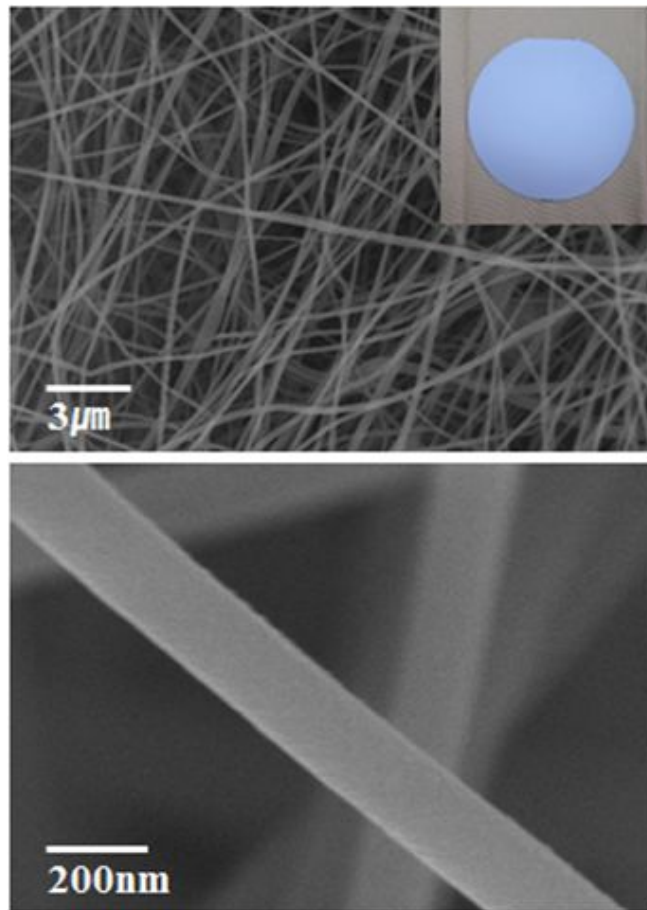


Figure 3.2.2 Morphologies of as-electrospun PAN nanofibers on wafer.

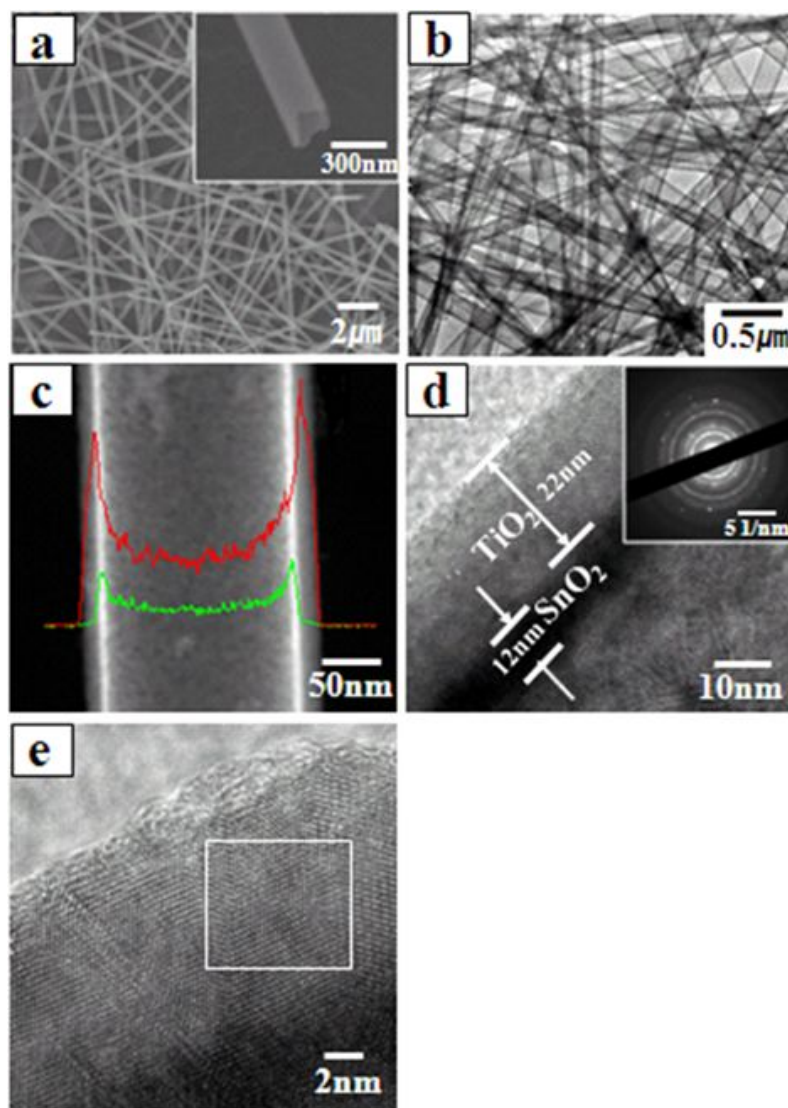


Figure 3.2.3 Characterization of $\text{SnO}_2@\text{TiO}_2$ double-shell nanotubes; a) FE-SEM and b) low magnification TEM images of double-shell nanotube network, c) STEM image and EDS line profiles of individual double-shell nanotube (red line: Ti, green line: Sn), d) high magnification TEM image and SAED pattern of double-shell nanotube

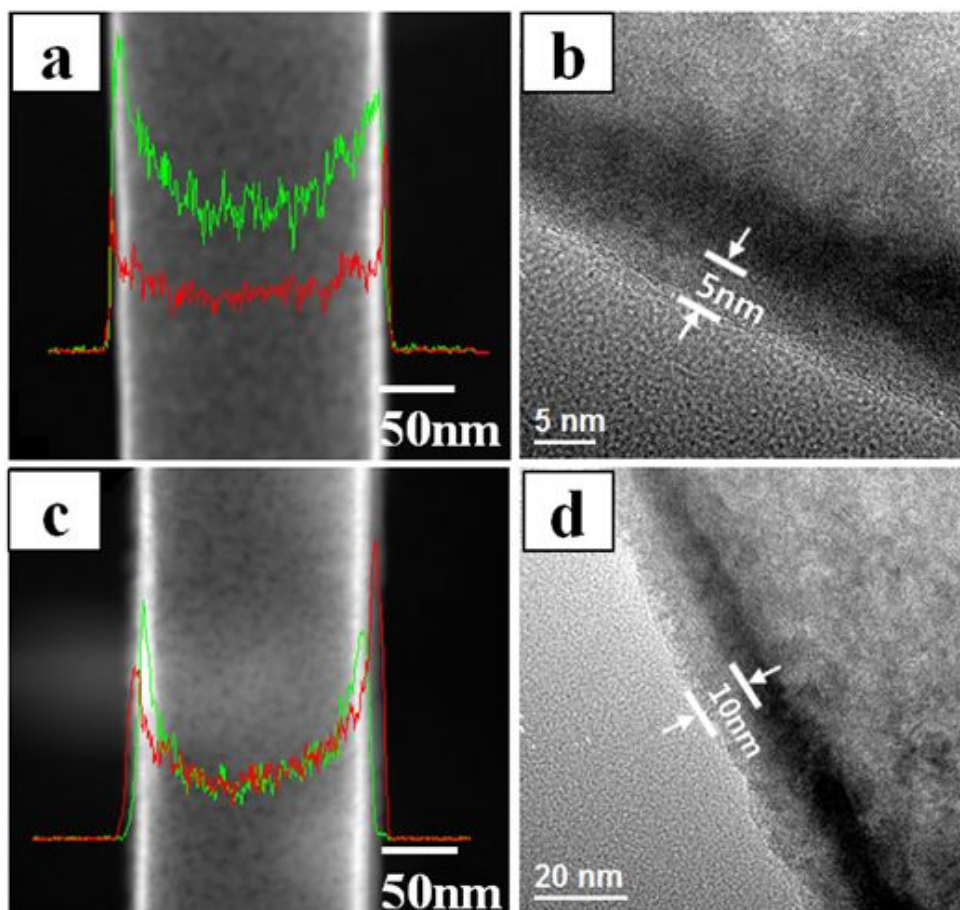


Figure 3.2.4 STEM images with EDS mapping (green: Sn, red: Ti) and low-magnification TEM images; the SnO₂-TiO₂ multi-shell nanotube of (a, b) 75 and (c, d) 150 ALD cycles for TiO₂ shell coating.

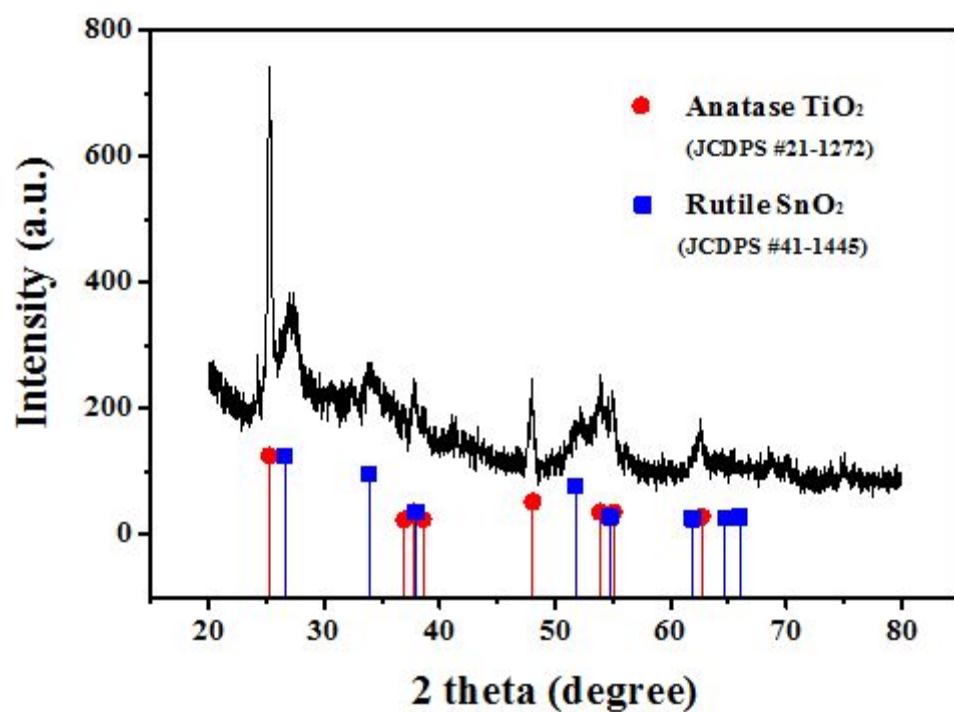


Figure 3.2.5 X-ray diffraction pattern of SnO₂@TiO₂ double-shell nanotubes

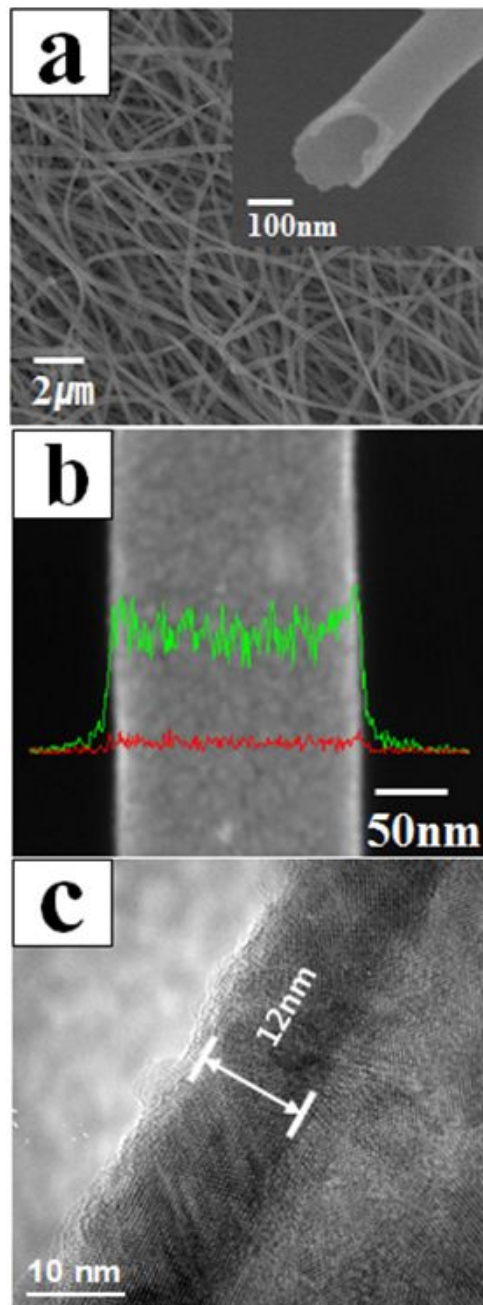


Figure 3.2.6 SnO₂ single shell nanotubes; (a) FE-SEM image, (b) STEM image and EDS line-profile (green: Sn, red: Ti), and (c) low-magnitude TEM image.

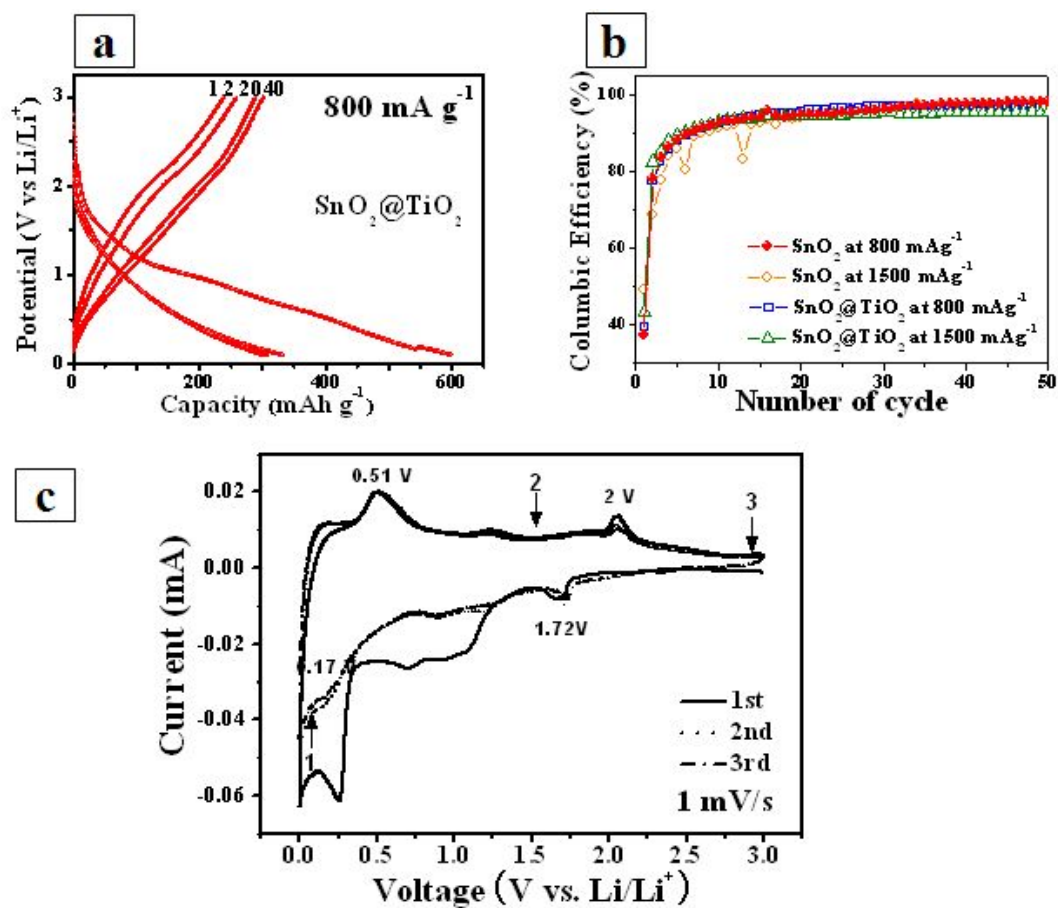


Figure 3.2.7 a) Charge/discharge voltage profile of $\text{SnO}_2@\text{TiO}_2$ nanotube electrode between 0.01 and 3.0 V at 800 mA g^{-1} , b) Coulombic efficiency of SnO_2 and $\text{SnO}_2@\text{TiO}_2$ nanotube electrodes at 800 and 1500 mA g^{-1} , c) Cyclic voltammetry of $\text{SnO}_2@\text{TiO}_2$ nanotube electrode.

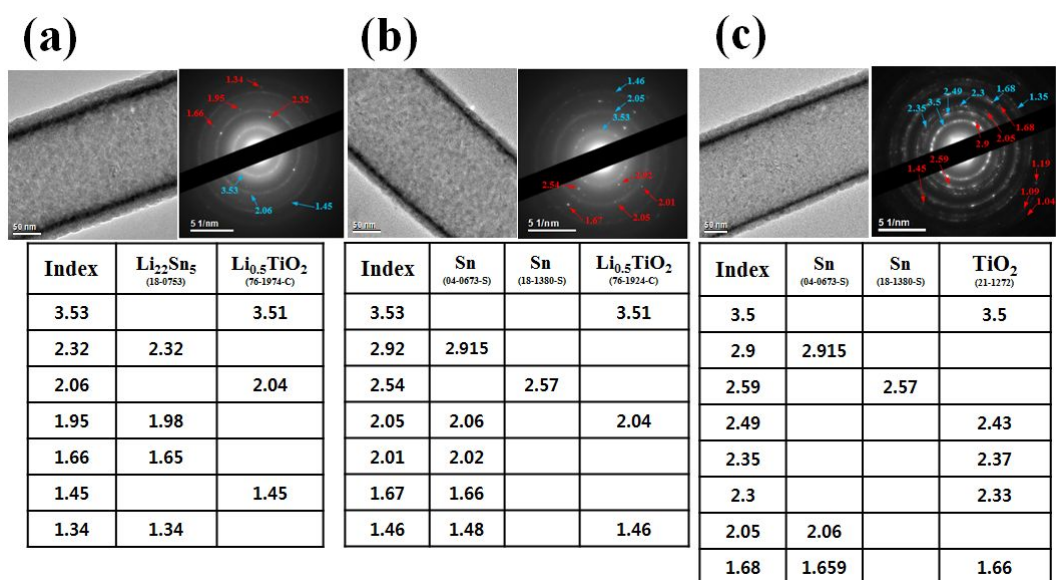


Figure 3.2.8 TEM images and SAED patterns at each potential in Figure 3.1.7c: a) discharge 0.2 V (point 1), b) charge 1.5V (point 2), and c) charge 2.9 V (point 3).

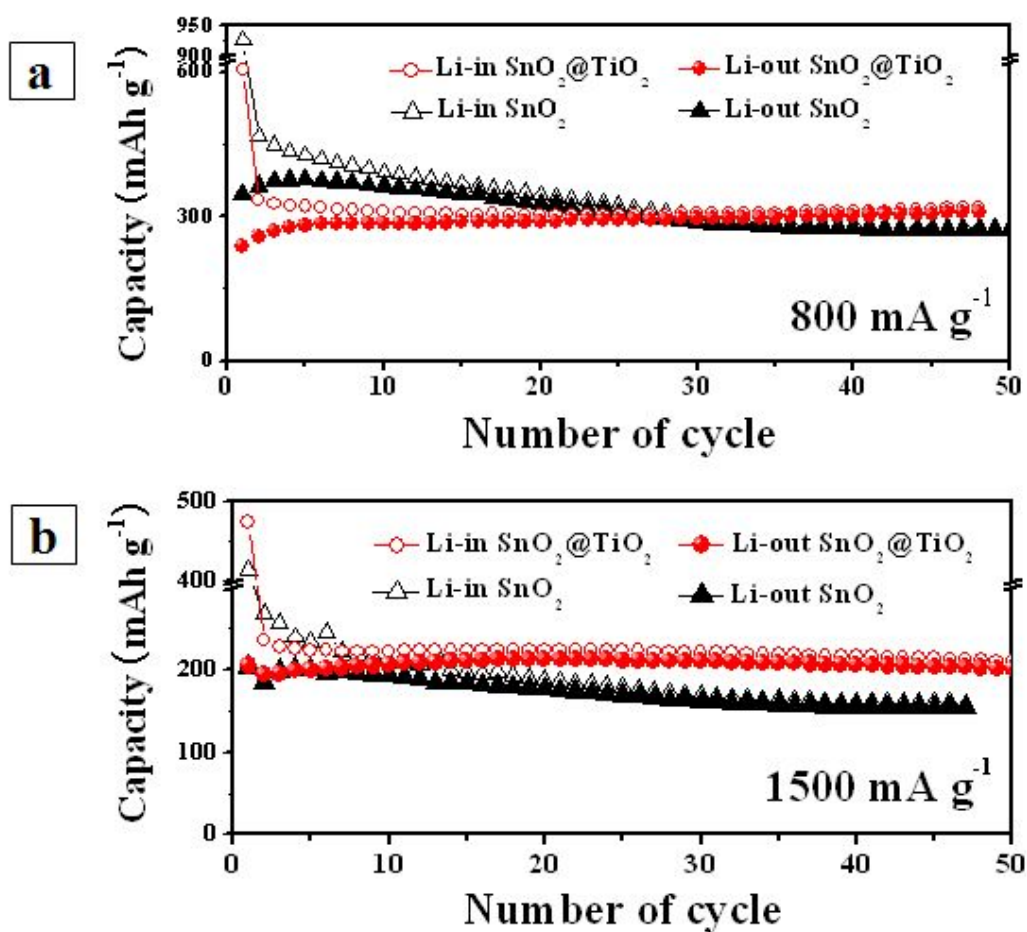


Figure 3.2.9 Cyclability of SnO₂ and SnO₂@TiO₂ nanotube electrodes at (a) 800 and (b) 1500 mA g⁻¹, respectively.

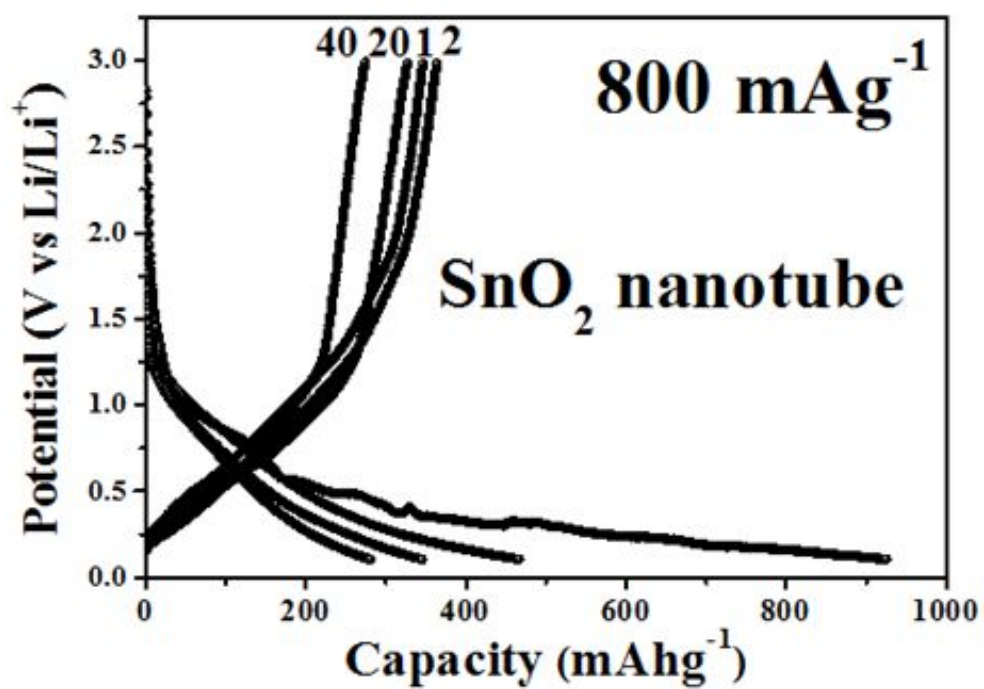


Figure 3.2.10 Charge/discharge voltage profile of SnO_2 nanotube electrode between 0.01 and 3.0 V at 800 mA g⁻¹.

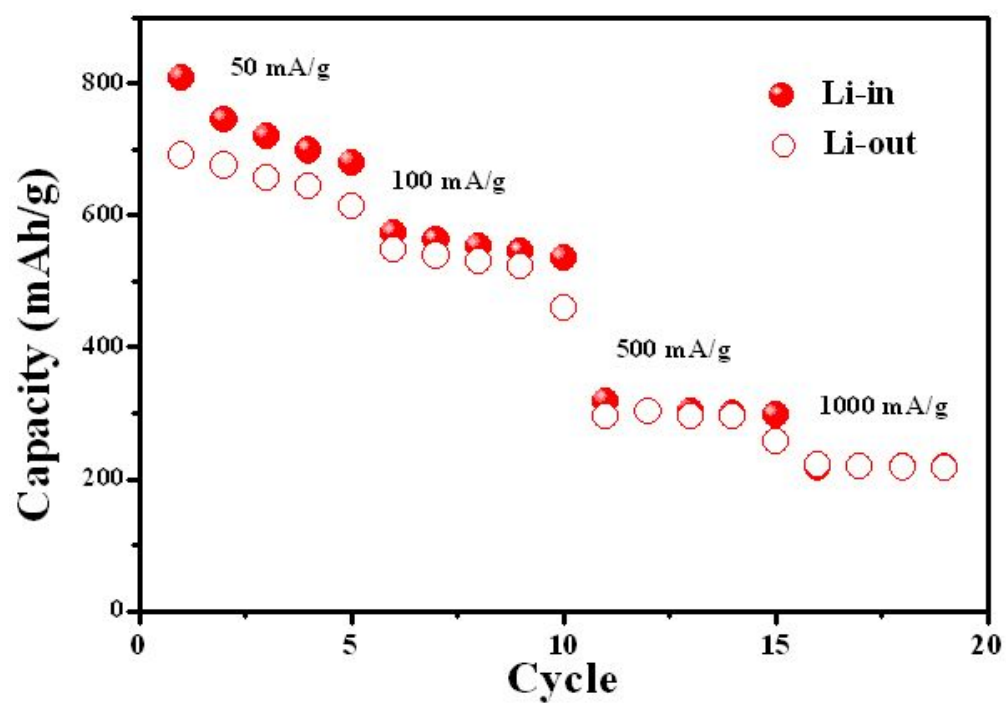


Figure 3.2.11 Rate capability test of SnO₂@TiO₂ double shell nanotube

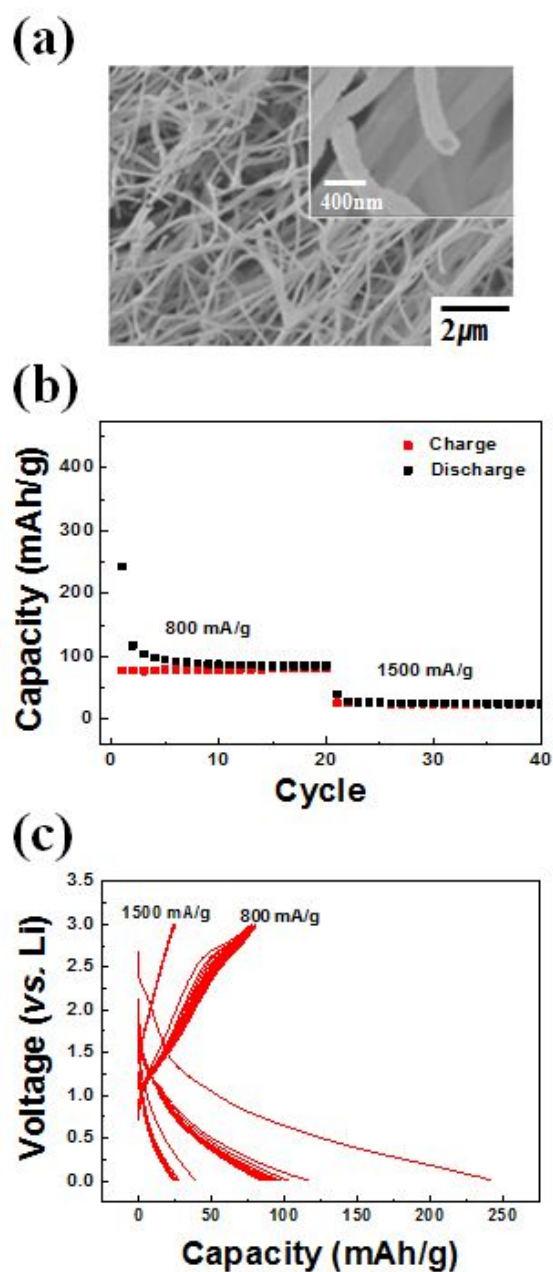


Figure 3.2.12 (a) The morphology of TiO_2 nanotube, (b) cycle performance and (c) charge/discharge voltage profile of TiO_2 nanotube electrode between 0.01 and 3.0 V at 800 and 1500 mA g^{-1} .

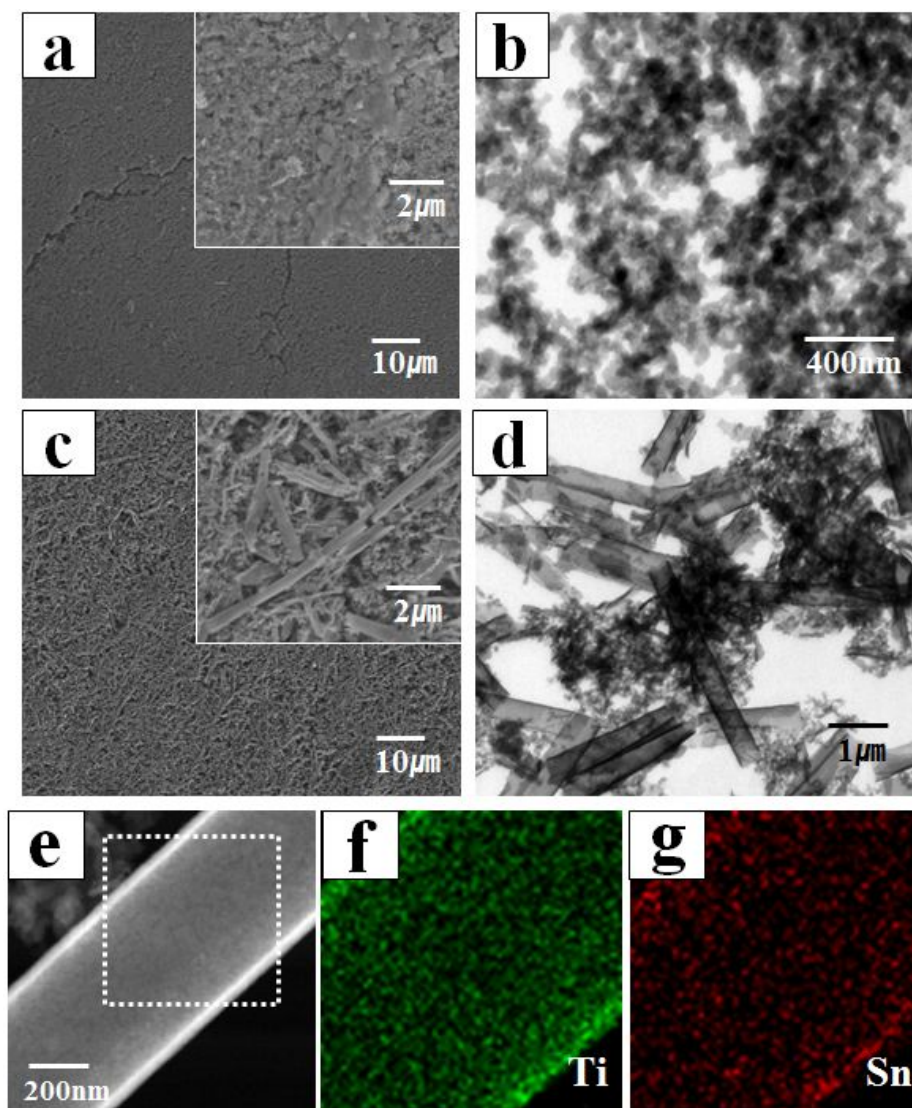


Figure 3.2.13 a) FESEM and b) TEM images of SnO_2 nanotube electrode after 5 cycles at 1500 mA g^{-1} , c) FESEM and d) TEM images of $\text{SnO}_2@\text{TiO}_2$ double-shell nanotube electrode after 5 cycles at 1500 mA g^{-1} , e) STEM image of individual double-shell nanotube in d), and (f, g) EDS element mapping of e)

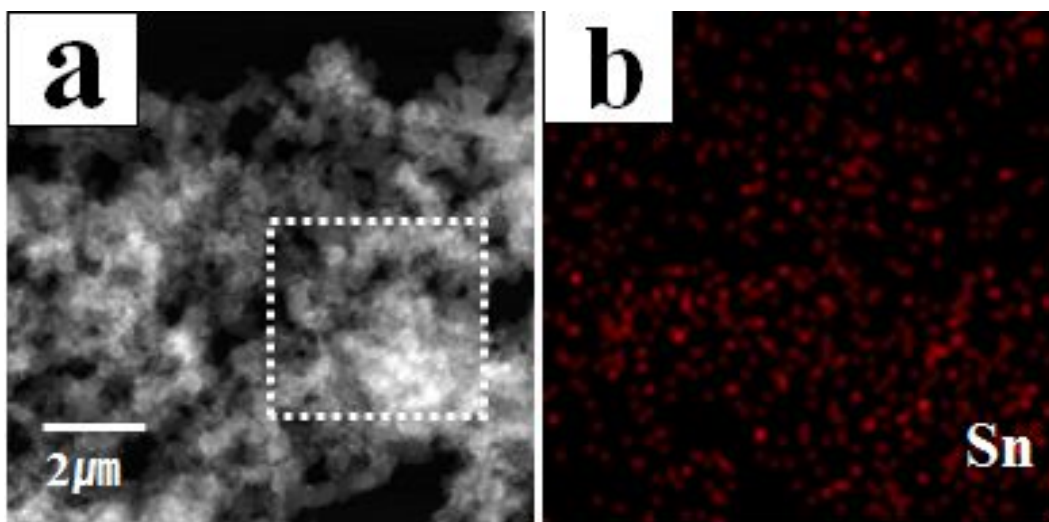


Figure 3.2.14 (a) STEM image of SnO₂ nanotube electrode after 5 cycles at 1500 mA g⁻¹ and (b) EDS element mapping.

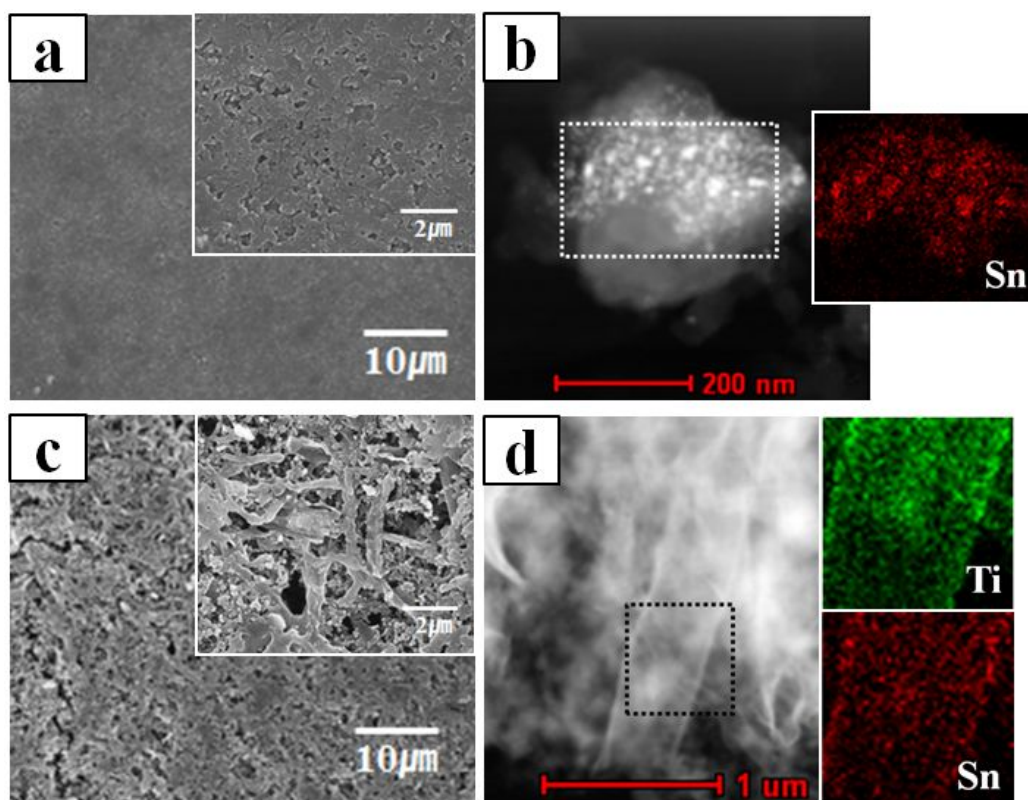


Figure 3.2.15 FESEM, STEM images, and element mapping of a, b) SnO_2 single-shell nanotube electrode and c, d) $\text{SnO}_2@\text{TiO}_2$ double-shell nanotube electrode after 50 cycles at 1500 mA g^{-1} .

3.3 TiO₂@SnO₂@TiO₂ Multi-shell Nanotube and its electrochemical properties

3.3.1. Experimental procedure

Synthesis and analysis of TiO₂@SnO₂@TiO₂ double-shell nanotubes

For electrospinning, PAN was dispersed on SiO₂/Si substrate and detail experimental conditions are shown in 3.1.1.1. The TiO₂, SnO₂, TiO₂ were deposited in turn on the as-electrospun PAN nanofibers by plasma-enhanced atomic layer deposition (PEALD). Dibutyltin diacetate and Titanium isopropoxide were used as the Sn and Ti precursor each and the time sequence for source pulse, first purge, O₂ pulse, plasma pulse, and second purge was 3, 12, 8, 1, and 12 s for SnO₂ deposition and 1, 12, 8, 1, and 12 s for TiO₂ coating, respectively. The number of ALD cycles for SnO₂ and TiO₂ coatings were 300 cycles in each coating step. The TiO₂@SnO₂@TiO₂ multi-shell coated PAN nanofibers were annealed at 700 °C for 1 h to burn out the PAN template and to crystallize the SnO₂ and TiO₂ shells. The schematic experimental procedure was shown in TiO₂@SnO₂@TiO₂ multi-shell nanotubes were characterized by X-ray diffraction (XRD, Bruker, D8-Advance) field emission scanning electron microscopy (FESEM, Hitachi, S-48000), inductively coupled plasma (ICP) mass spectrometer

and transmission electron microscopy (TEM, FEI, Tecnai F20) equipped with energy dispersive spectroscopy (EDS).

Electrochemical measurement

For electrochemical measurements, the test electrodes consisted of the active powder material (70 wt%), carbon black (Ketchen Black, 10 wt%) as a conducting agent and poly amide imide (PAI, 20 wt%) dissolved in N-methyl pyrrolidinone (NMP) at 60 °C as a binder. Each component was well mixed to form slurry using a magnetic stirrer. The slurry was coated onto a copper foil substrate, pressed, and dried at 200 °C for 4 h under a vacuum. A coin-type electrochemical cell was used with Li foil as the counter and reference electrodes, and 1 M LiPF₆ in ethylene carbonate (EC)/diethylene carbonate (DEC) (5:5 (v/v), PANAX) was used as the electrolyte. The cell assembly and all of the electrochemical tests were carried out in an Ar-filled glove box. The cycling experiments were galvanostatically performed using a Maccor automated tester at a constant current of 50 mA g⁻¹ for the active material within the voltage range between 0.0 and 3.0 V (vs. Li/Li⁺) and additionally various condition of current density was applied for investigating high rate cyclability. During the discharging step, Li was inserted into the electrode, while Li was extracted from the electrode during the charge. After the electrochemical measurements, the coin cell was disassembled and washed completely with ethanol for SEM and TEM analyses.

3.3.2. Result and discussion

The as-electrospun PAN nanofibers were connected to each other, forming a self-supporting network (Figure 3.3.1a). The PAN nanofibers had a relatively uniform diameter of 200 ~ 300 nm with a smooth surface, and their length was more than several tens of micrometers. The nanotubes had uniform diameter without structural distortion, demonstrating that the ALD process yielded uniform and conformal $\text{TiO}_2@\text{SnO}_2@\text{TiO}_2$ coating on PAN templates. (Figure 3.3.1b) The nanofiber network was well adhered to the Si substrate, and it was detached from the substrate after annealing at 700 °C.

The morphology of $\text{TiO}_2@\text{SnO}_2@\text{TiO}_2$ multi-shell nanotubes was characterized by FESEM. The original arrangement of PAN templates was preserved in the $\text{TiO}_2@\text{SnO}_2@\text{TiO}_2$ multi-shell nanotubes forming the network structure (Figure 3.3.2). As shown in Figure 3.3.2a and b, the synthesized nanotubes show straight shape with 1-dimensional direction and uniform diameter without any structural distortion such as collapsing. The calcination at 700°C removed effectively the PAN nanofiber cores, resulting the hollow nanotubes. Low-magnification TEM image showed the tube-like structure, with bright-colored core free inner space and dark-colored metal oxide shell (Figure 3.3.2c). The wall thickness was constant along the entire length of the nanotubes. A typical XRD result showing the product evolution after the heat treatment at

700°C for 1h is shown in Figure 3.3.2d. The analysis of the as-synthesized nanotubes by X-ray diffraction corresponds to the mixture phase of anatase TiO₂ (JCPDS No. 21-1272) and rutile SnO₂ (JCPDS No. 41-1445). The weight ratio of Ti to Sn estimated by EDS, ICP was 2.

For the further study on multi-shells nanotube, the cross-sectional view of nanotube shell was investigated in the perpendicular direction to nanotube cross-view. (Figure 3.3.3a) The STEM image shown in Figure 3.3.3b confirmed that the walls of the nanotubes were composed of multi-shells; dark-colored shell with low atomic number and bright-colored shell with high atomic number in the center of shell. The EDS line profiles clearly demonstrated that Sn was present in the core and Ti was located in the outer shell and this line profile and element mapping images were corresponding to STEM images with three district shells. (Figure 3.3.3b~d) The thickness of each shell was ~ 10 nm. It is noted that the precise thickness control of shell thickness in nanotube structure by ALD has been demonstrated in a previous study. [49] Consequently, crystalline TiO₂@SnO₂@TiO₂ multi-shell nanotubes were successfully fabricated by combining PAN nanofiber templates and ALD coating process.

For comparison, SnO₂ and TiO₂ single-shell nanotubes and SnO₂@TiO₂ double-shell nanotubes were synthesized in the same process. The wall thickness of SnO₂, TiO₂ single-shell nanotubes was ~30 nm. The each nanotubes were crystallized to rutile SnO₂ (JCPDS#41-1445) and anatase TiO₂ (JCDPS#21-1272).

(Figure 3.3.4)

The discharge/charge voltage profile of the $\text{TiO}_2@\text{SnO}_2@\text{TiO}_2$ multi-shell nanotube electrode is illustrated in Figure 3.3.5a. In order to understand the Li-ion charge/discharge reaction further, cyclic voltammetry (CV) of the $\text{TiO}_2@\text{SnO}_2@\text{TiO}_2$ multi-layered nanotubes was conducted with 0.2 mV s^{-1} . (Figure 3.3.5b) The curve of the first cycle is different from later ones, possibly due to the formation of a solid-electrolyte interface (SEI) and Li_2O . [50,51] It were confirmed that the reduction/oxidation peak pairs at 0.27 V and 0.56 V is attributable to lithium ion alloying/dealloying with SnO_2 and the small reduction/oxidation peak pairs at 1.65 V and 2.1 V is attributable to lithium ion insertion into/extraction out of TiO_2 . [50-53] Even through SnO_2 layer is embedded in TiO_2 shell, the reaction of Li-ion charge/discharge with SnO_2 is activated due to nanosized thickness of TiO_2 shell therefore the low capacity of TiO_2 can be compensated. The cycling experiments were conducted in the voltage range between 0.01 and 3.0 V (vs. Li/Li^+) at a current density of 50 mA g^{-1} . (Figure 3.3.5c) As control groups, SnO_2 , TiO_2 single nanotube with 30nm shell thickness were synthesized and fabricated to coin-cell for test. TiO_2 nanotube exhibited excellent capacity retention from initial stages but reversible capacity was relatively low, 235 mAh/g at 50th cycle. Otherwise, SnO_2 nanotube shows high reversible capacity but severe capacity fading was observed. In order to investigate the structural geometry effect on electrochemical properties,

$\text{SnO}_2(10\text{nm})@\text{TiO}_2(20\text{nm})$ nanotubes were prepared, SnO_2 inner shell (10nm thickness) encapsulated by TiO_2 outer shell (20nm thickness). From the result, electrical performance in initial stage was similar to that of $\text{TiO}_2@\text{SnO}_2@\text{TiO}_2$ multi-shell nanotube but the tendency to fade reversible capacity is more severe as cycle number increased. The structure of SnO_2 sandwiched between TiO_2 layers can effectively accommodate the SnO_2 volume expansion during reaction with Li -ion, leading to stable electrochemical performance. $\text{TiO}_2@\text{SnO}_2@\text{TiO}_2$ multi-shell nanotube exhibit different discharge-charge profiles in the first and second cycles. The specific discharge capacity is 2439 mAh g^{-1} in the first cycle but it dramatically dropped to 1213 in the second cycle. The coulombic efficiency of the first cycle was low (about 40 %) in Figure 3.3.5d, which was due to the irreversible reduction of SnO_2 to Sn and Li_2O and the formation of the solid electrolyte interface (SEI) layer on the surface of electrode. As the number of cycle increase, the coulombic efficiency increase dramatically up to 96% in the following cycles. (Figure 3.3.5d) With extended cycling, the capacity change tends to be stable and the discharge capacity is relatively maintained shown in Figure 3.3.5d, indicating good capacity retention and the discharge capacity was $\sim 550 \text{ mAh g}^{-1}$ at 60th cycle. Figure 3.3.6a shows the cycling performance of SnO_2 , TiO_2 nanotubes and $\text{TiO}_2@\text{SnO}_2@\text{TiO}_2$ multi-shell nanotube at different current densities (from the second cycle). The $\text{TiO}_2@\text{SnO}_2@\text{TiO}_2$ multi-shell nanotube exhibited decent high rate performance. The discharge capacities were

maintained at high value when cycled at different current densities: 500 mAh g⁻¹ at 0.2 A g⁻¹, 440 mAh g⁻¹ at 0.5 A g⁻¹, 400 mAh g⁻¹ at 1 A g⁻¹, 370 mAh g⁻¹ at 1.5 A g⁻¹, 350 mAh g⁻¹ at 2 A g⁻¹, 305 mAh g⁻¹ at 4 A g⁻¹, 295 mAh g⁻¹ at 5 A g⁻¹. The high-rate performances of SnO₂, TiO₂ nanotubes with 30 nm shell thickness were compared to that of TiO₂@SnO₂@TiO₂ multi-shell nanotube. The reversible capacity of SnO₂ nanotube in initial stage was much higher than that of TiO₂@SnO₂@TiO₂ multi-shell nanotube but severe capacity fading was observed as current density and number of cycle increase. TiO₂ nanotube shows excellent capacity retention capability at current densities from 0.2 to 5 A g⁻¹ but reversible capacities were relatively low. The high rate performance of TiO₂@SnO₂@TiO₂ multi-shell nanotubes exhibited high reversible capacity and coulombic efficiency up to ~99%. (Figure 3.3.6b) In terms of capacity value and capacity retention, the synergetic effect was confirmed in the electrochemical performance of TiO₂@SnO₂@TiO₂ multi-shell nanotube.

3.3.3 Conclusion

TiO₂@SnO₂@TiO₂ triple multi shell nanotubes were synthesized via simple process with a precise thickness control and fabricated to coin cell for electrochemical test. The TiO₂@SnO₂@TiO₂ multi shell nanotubes were beneficial for the electrochemical performance, as demonstrated in terms of stable

cyclability and high rate performance. We believe that the high capacity of SnO_2 and the superior cycling performance of TiO_2 are synergistically combined in the $\text{TiO}_2@\text{SnO}_2@\text{TiO}_2$ multi-shell nanotube electrode.

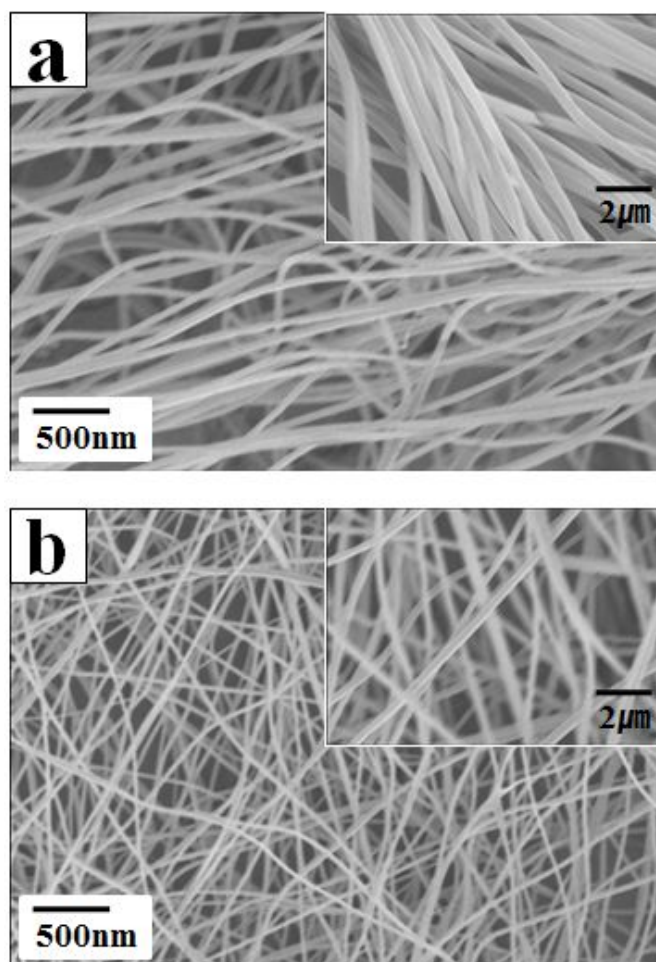


Figure 3.3.1 (a) As prepared PAN and (b) As-coated PAN

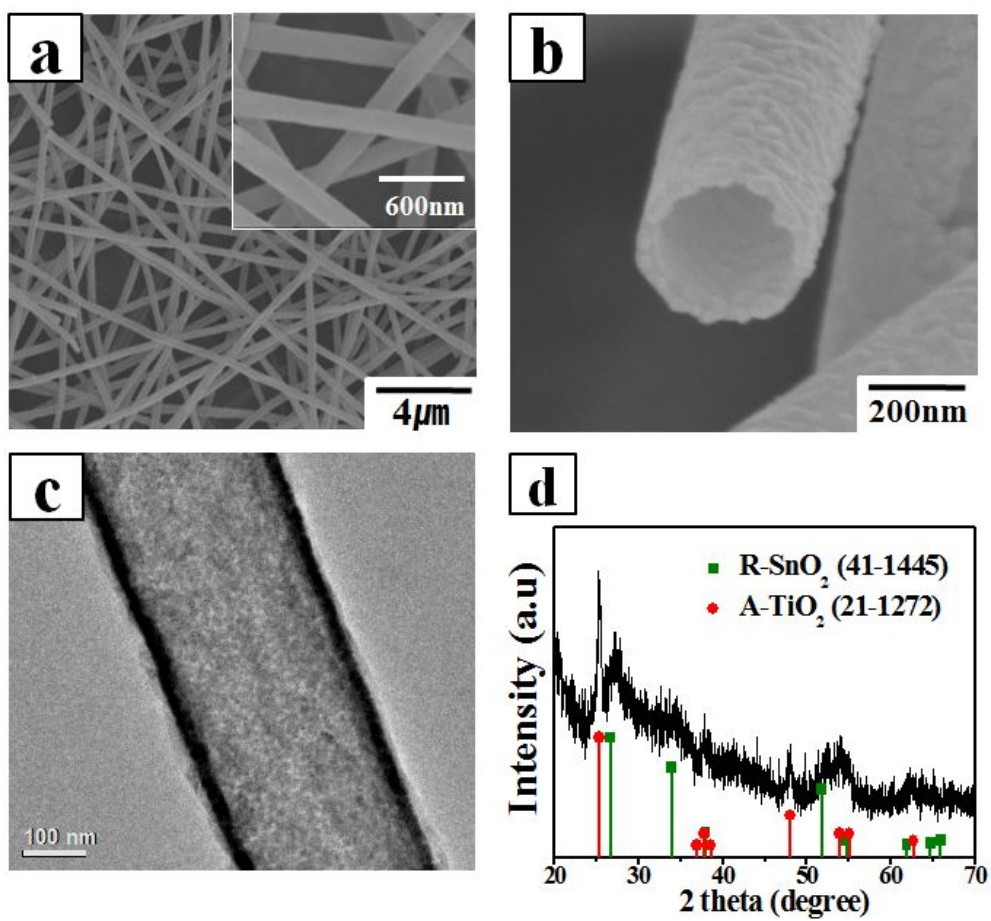


Figure 3.3.2 (a, b) FESEM, (c) TEM images and (d) X-ray diffraction pattern of $\text{TiO}_2@\text{SnO}_2@\text{TiO}_2$ nanotube

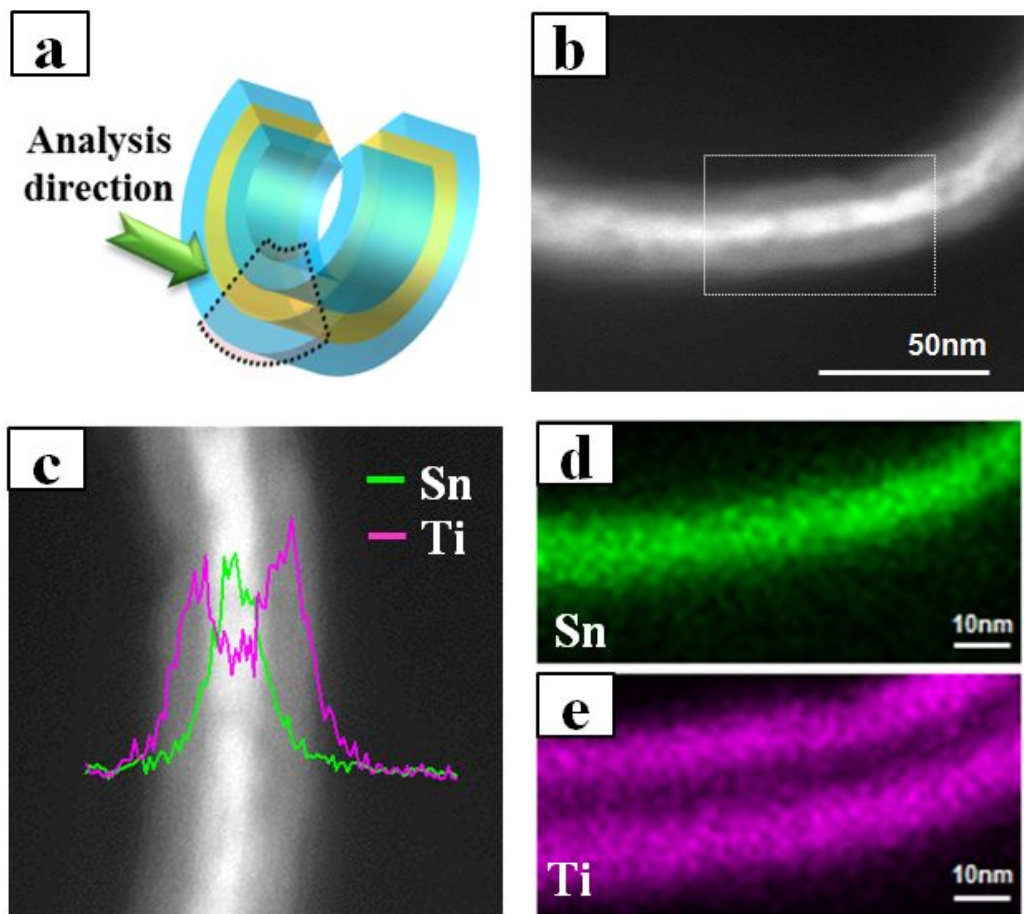


Figure 3.3.3 (a) STEM analysis direction, (b) STEM image and its (c) line profile and (d, e) elements mapping image in inert square of (b)

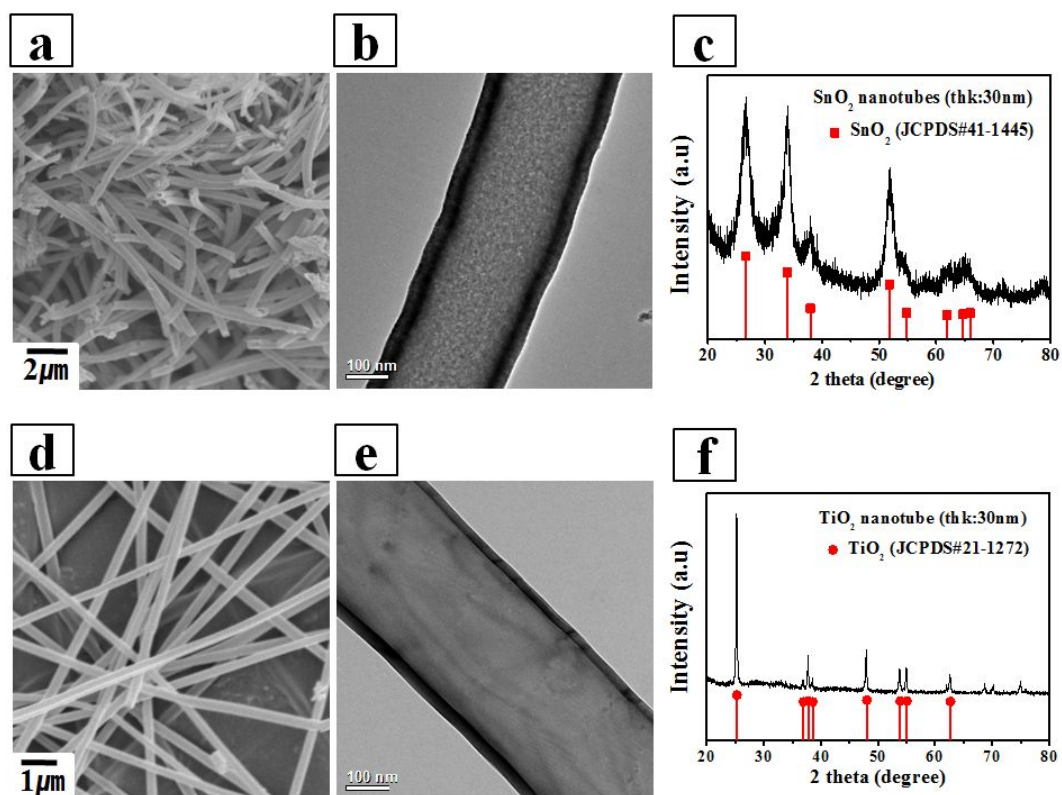


Figure 3.3.4 FESEM, TEM images and X-ray diffraction pattern of (a~c) SnO₂ and (d~f) TiO₂ nanotube

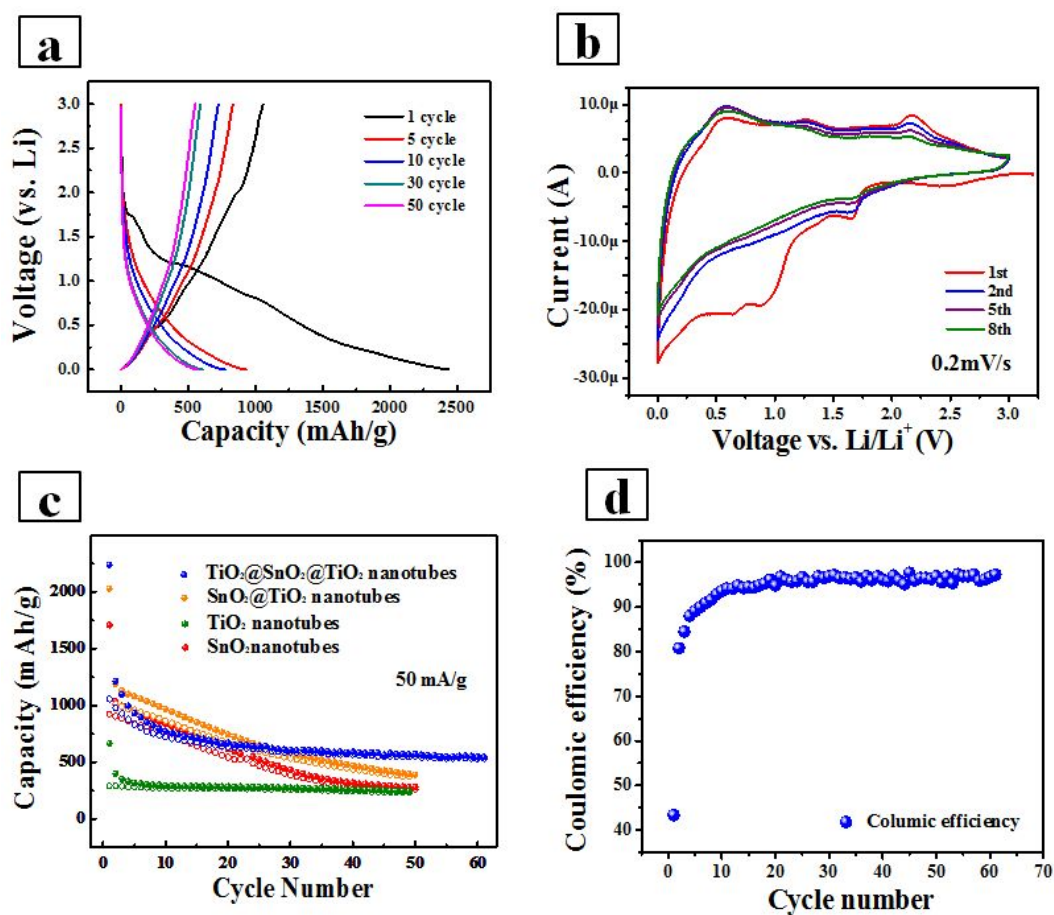


Figure 3.3.5 (a) Charge/discharge voltage profile, (b) cyclic voltammetry, (c) cycle performances and (d) its coulombic efficiency of $\text{TiO}_2@\text{SnO}_2@\text{TiO}_2$ nanotube

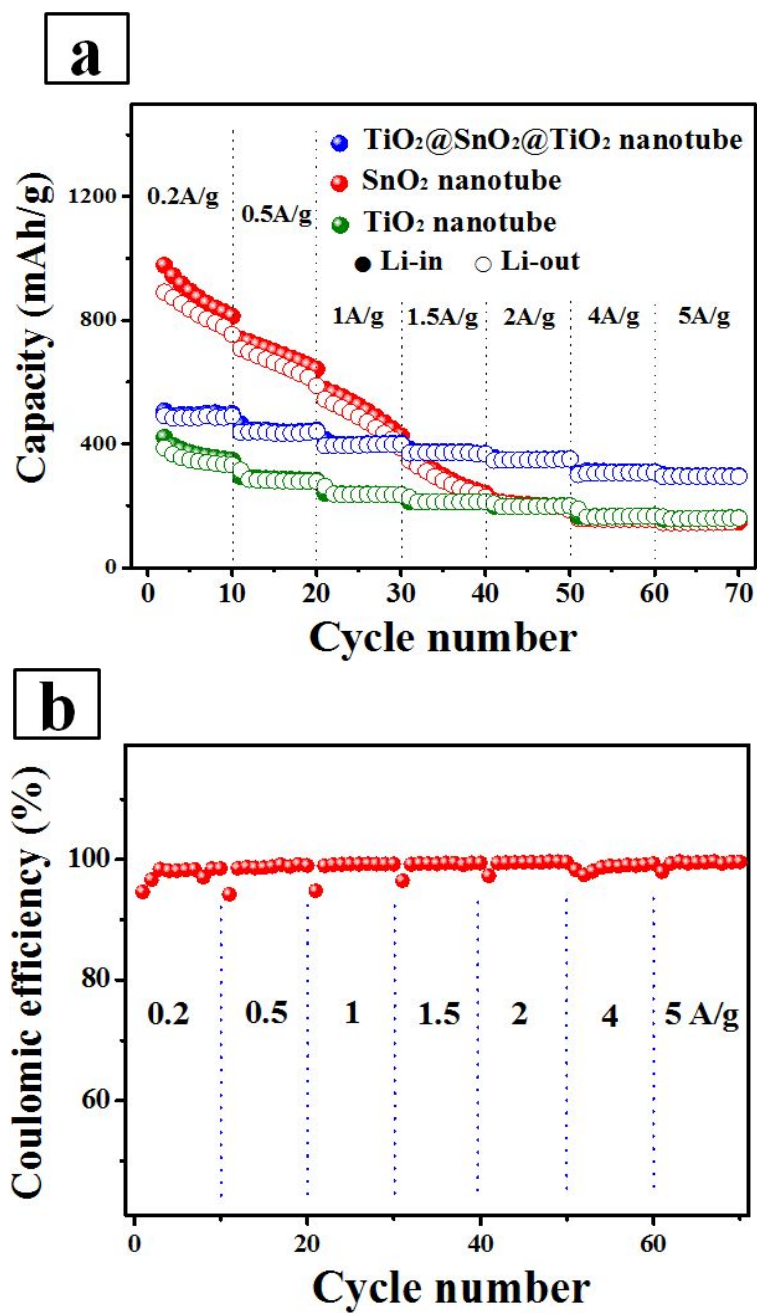


Figure 3.3.6 (a) Rate performance and (b) coulombic efficiency of $\text{TiO}_2@\text{SnO}_2@\text{TiO}_2$ nanotube at varied current density

3.4 Reference

1. B. Scrosati, *Nature*, 373 (1995) 557.
2. S. Megahed and W. Ebner, *J. Power. Sourc.*, 54 (1995) 155.
3. Y. Nishi, *J. Power. Sourc.*, 100 (2001) 101.
4. M. Endo, C. Kim, K. Nishimura, T. Fujino and K. Miyashita, *Carbon*, 38 (2000) 183.
5. D. Fauteux and R. Koksang, *J. Appl. Electrochem.*, 23 (1993) 1.
6. L. Ji, Z. Lin, M. Alcoutlabi and X. Zhang, *Energ. Environ. Sci.*, 4 (2011) 2682.
7. K. T. Lee, Y. S. Jung and S. M. Oh, *J. Am. Chem. Soc.*, 125 (2003) 5652.
8. I. A. Courtney and J. Dahn, *J. Electrochem. Soc.*, 144 (1997) 2045.
9. M. Winter, J. O. Besenhard, M. E. Spahr and P. Novák, *Adv. Mater.*, 10 (1998) 725.
10. K.S Park, K.M Min, Y.H Jin, S.D. Seo, G.H. Lee, H.W. Shin, D.W. Kim, *J. Mater. Chem.*, 22 (2012) 15981.
11. G.F. Ortiz, I. Hanzu, T. Djenizian, P. Lavela, J.L. Tirado, P. Knauth, *Chem. Mater.*, 21 (2009) 63.
12. J. Wang, Y. Bai, M. Wu, J. Yin, W.F. Zhang, *J. Power Source*, 191 (2009) 614.

13. F. Zhang, Y. Zhang, S. Song, H. Zhang, *J. Power Source*, 496 (2011) 8618.
14. Y. Yao, M. T. McDowell, I. Ryu, H. Wu, N. Liu, L. Hu, W. D. Nix and Y. Cui, *Nano Lett.*, 11 (2011) 2949.
15. M. H. Park, K. Kim, J. Kim and J. Cho, *Adv. Mater.*, 22 (2010) 415.
16. H. Ma, F. Cheng, J. Y. Chen, J. Z. Zhao, C. S. Li, Z. L. Tao and J. Liang, *Adv. Mater.*, 19 (2007) 4067.
17. X. M. Yin, C. C. Li, M. Zhang, Q. Y. Hao, S. Liu, L. B. Chen and T. H. Wang, *J. Phys. Chem. C*, 114 (2010) 8084.
18. S. Han, B. Jang, T. Kim, S. M. Oh and T. Hyeon, *Adv. Funct. Mater.*, 15 (2005) 1845.
19. H. X. Yang, J. F. Qian, Z. X. Chen, X. P. Ai and Y. L. Cao, *J. Phys. Chem. C*, 111 (2007) 14067.
20. D. Deng and J. Y. Lee, *Chem. Mater.*, 20 (2008) 1841.
21. L. Xiao, J. Li, Q. Li and L. Zhang, *J. Solid State Electrochem.*, 14 (2010) 931.
22. S. Ding, J. S. Chen, G. Qi, X. Duan, Z. Wang, E. P. Giannelis, L. A. Archer and X. W. Lou, *J. Am. Chem. Soc.*, 133 (2010) 21.
23. Z. Wang, D. Luan, F. Y. C. Boey and X. W. Lou, *J. Am. Chem. Soc.*, 133 (2011) 4738.

24. X. W. Lou, Y. Wang, C. Yuan, J. Y. Lee and L. A. Archer, *Adv. Mater.*, 18 (2006) 2325.
25. 3.X. Su, Q.L. Wu, X. Zhan, J. Wu, S. Wei, Z. Guo, *J. Mater. Sci.*, 47 (2012) 2534.
26. J.S Chen, L.A. Archer, X.W. Lou, *J. Mater. Chem.*, 21 (2011) 9912.
27. J. Xu, C. Jia, B. Cao, W.F. Zhang, *Electrochim. Acta*, 52 (2007) 8044.
28. D. Deng, M. G. Kim, J. y. Lee, J. Cho, *Energy Environ. Sci.*, 2 (2009) 818.
29. Y.S. Hu, L. Kienle, Y.G. Guo, J. Maier, *Adv. Mater.*, 18 (2006) 1421.
30. K.S Park, K.M Min, Y.H Jin, S.D. Seo, G.H. Lee, H.W. Shin, D.W. Kim, *J. Mater. Chem.*, 22 (2012) 15981.
31. B. Zachau-Christiansen, K. West, T. Jacobsen, S. Atlung, *Solid State Ionics*, 28 (1988) 1176.
32. J.S. Chen, X.W. Lou, *J. Power Source*, 95 (2010) 2905.
33. S. Dong, H. Wang, L. Gu, X. Zhou, Z. Liu, P. Han, Y. Wang, X. Chen, G. Cui, L. Chen, *Thin Solid Films*, 519 (2011) 5978.
34. Y.G. Guo, J.S. Hu, L.J. Wan, *Adv. Mater.*, 20 (2008) 2878.
35. C. Jiang, I. Honma, T. Kudo, H. Zhou, *Electrochem.Solid-State Lett.*, 10 (2007) A127.

36. G.F. Ortiz, I. Hanzu, T. Djenizian, P. Lavela, J.L. Tirado, P. Knauth, *Chem. Mater.*, 21 (2009) 63.
37. J. Wang, Y. Bai, M. Wu, J. Yin, W.F. Zhang, *J. Power Source*, 191 (2009) 618.
38. F. Zhang, Y. Zhang, S. Song, H. Zhang, *J. Power Source*, 496 (2011) 8618.
39. I.A. Courtney, J.R. Dahn, *J. Electrochem. Soc.*, 144 (1997) 2045.
40. M. Winter, J.O. Besenhard, M.E. Spahr, P. Novak, *Adv. Mater.*, 10 (1998) 725.
41. M.S. Park, Y.M. Kang, G.X. Wang, S.X. Dou, H.K. Liu, *Adv. Funct. Mater.* 18 (2008) 455.
42. H. Wu, G. Chan, J.W. Choi, I. Ryu, Y. Yao, M.T. McDowell, S.W. Lee, A. Jackson, Y. Yang, L. Hu, Y. Cui, *Nature nanotechnology* 7 (2012) 310.
43. W. S. Kim, B. S. Lee, D. H. Kim, H. C. Kim, W. R. Yu and S. H. Hong, *Nanotechnology* 21 (2010) 245605.
44. H. Park, T. Song, H. Han, A. Devadoss, J. Yuh, C. Choi and U. Paik, *Electrochem. Commun.* 22 (2012) 81.
45. G. Kilibarda, D. V. Szabo, S. Schlabach, V. Winkler, M. Bruns, T. Hanemann, *J. Power. Sources* 233 (2013) 139.

46. G. Du, Z. Guo, P. Zhang, Y. Li, M. Chen, D. Wexler, H. Liu, *J. Mater. Chem.*, 20 (2010) 5689.
47. X. Wu, S. Zhang, L. Wang, Z. Du, H. Fang, Y. Ling and Z. Huang, *J. Mater. Chem.*, 22 (2012) 11151.
48. J. Wang, Y. Zhou, Y. Hu, R. O'Hayre, Z. Shao, *J. Phys. Chem. C*, 115 (2011) 2529.
49. J.H. Jeun, K.Y. Park, D.H. Kim, W.S. Kim, H.C. Kim, B.S. Lee, H. Kim, W.R. Yu, K. Kang, S.H. Hong, *Nanoscale*, 5 (2013) 8480.
50. G. Kilibarda, D. V. Szabo, S. Schlabach, V. Winkler, M. Bruns, T. Hanemann, *J. Power. Sources*, 233 (2013) 139.
51. G. Du, Z. Guo, P. Zhang, Y. Li, M. Chen, D. Wexler, H. Liu, *J. Mater. Chem.*, 20 (2010) 5689.
52. J. Wang, Y. Zhou, Y. Hu, R. O'Hayre, Z. Shao, *J. Phys. Chem. C*, 115 (2011) 2529.
53. X. Wu, S. Zhang, L. Wang, Z. Du, H. Fang, Y. Ling and Z. Huang, *J. Mater. Chem.*, 22 (2012) 11151.

국문 초록

본 연구에서는 나노 다공체를 합성하여 1) 반도체식 가스 센서, 2) 이차전지의 음극재로 활용하는 연구를 진행하였다.

첫 번째 장에서는 전기 화학적 방법인 양극산화법과 전기 도금법을 이용하여 나노다공 구조체를 합성하여 가스 센서에 응용하는 연구를 진행하였다. SnO_2 는 넓은 Energy band gap을 가지는 n-type 반도체 물질로써 가스와 흡착 반응을 통한 저항의 변화로 가스를 탐지하는 대표적인 센서의 물질로 여러 분야에 이용되고 있다. 최근에는 다양한 형태의 구조를 이용하여 센서의 성능을 결정짓는 반응 및 회복 시간과 장기 안정성을 향상을 위해 나노구조체를 이용한 가스 센서의 연구가 활발히 진행되고 있다. 특히 나노 다공 구조체는 넓은 부피 대 면적 비를 가지고 있고 template으로 사용 가능하여 다른 물질과의 이종물질 접합 구현이 유리하다는 점에 있어서 차세대 가스 센서의 구조로 연구되고 있다. 이러한 다공성 구조를 구현하기 위해 양극산화 및 전기 도금법이 널리 쓰이고 있다.

양극산화 및 전기 도금법을 통해 구현된 Sn foil의 표면에 생성된 합성체는 비정질 결정상 및 금속상을 나타내기 때문에 결정화 과정이

요구되지만 250℃의 낮은 녹는점을 가지는 모체 물질인 Sn로 인해 결정화에 어려움이 있어왔다. 이러한 문제점으로 인해 본 연구에서는 SiO₂기판 위에 Sn을 열 증착법을 이용하여 코팅하여 Sn 박막을 전극으로 활용하였다. 실험 결과 두 전기화학 방법을 통해 나노 다공성 구조체가 합성되는 것을 확인할 수 있었으며 SnO₂로 결정화하는 열처리 과정 이후에도 구조가 잘 유지되고 있음을 확인할 수 있었다. 가스 감응 특성에서도 기존의 분말 형태의 가스 감응 특성보다 더 우수한 감응 특성을 나타내는 것을 확인할 수 있었다. 이와 더불어 각각의 합성된 구조체와 CuO를 이중 접합하여 가스 감응 특성의 선택성을 향상 시키는 연구를 진행하였으며 가스 감응 특성에서 H₂S가스에 대해 높은 선택적 감응 특성을 나타내는 것을 확인할 수 있었다. 이는 SnO₂와 CuO의 이중 접합으로 인한 pn junction의 형성과 소멸에 의해 발생된 현상임을 분석을 통해 확인하였다.

두 번째 장에서는 SnO₂와 TiO₂의 이중층의 나노튜브를 합성하고 이를 전기 화학 특성을 평가하는 실험을 진행하였다. SnO₂의 경우에는 현재 대용량 리튬이온 배터리의 실현을 위해 흑연 음극재를 대체할 물질로 많이 연구가 되고 있다. 하지만 리튬이온과 충방전 반응에서 발생하는 300% 가까이 되는 부피팽창으로 인하여 실용화되는데 많은

문제점을 가지고 있다. 이를 해결하기 위해 나노튜브 형태로 합성하여 부피팽창 시 내부 빈 공간을 통해 기계적 stress를 완화하고 바깥층으로 TiO_2 를 감싸 encapsulation하여 전기 화학적 특성을 향상시키는 실험을 진행하였다. TiO_2 의 경우에는 음극재로써 상대적으로 낮은 용량을 나타내지만 빠른 충방전 속도와 구조적 안정성을 유지한다는 장점이 있다. SnO_2 와 TiO_2 의 이중 접합을 통해 용량을 향상시키고 충방전 과정에서 안정성을 추구하는 시너지 효과를 얻는 것을 목표로 실험을 진행하였다.

합성 방법은 실리콘 웨이퍼 위에 polyacrylonitrile(PAN)을 방사하고 이를 template으로 하여 ALD를 통해 SnO_2 와 TiO_2 를 순차적으로 코팅하였다. 코팅된 시편은 PAN을 제거하고 결정화를 위해 열처리를 진행하였다. 실험 결과 200~300 nm 두께의 나노튜브가 합성된 것을 확인할 수 있었으며 SnO_2 10nm, TiO_2 20nm의 두께로 각각 코팅된 것을 확인할 수 있었다. 전기 화학적 특성 평가 결과 800, 1500 mA g^{-1} 의 빠른 충방전 속도에서도 장기 안정성과 향상된 용량을 나타내는 것을 확인하였으며 충방전 시험이 끝난 시편을 분석한 결과 튜브 형태가 그대로 유지되고 있음을 확인할 수 있었다. 따라서 이와 같이 향상된 전기 화학적 특성의 경우에는 음극 물질이 리튬이온과의

반응에서 구조적으로 안정함에 있어서 얻을 수 있음을 확인하였다.
이와 더불어 TiO_2 10nm, SnO_2 10nm, TiO_2 10nm 두께로 삼중
구조체를 가진 나노 튜브를 합성하여 전기 화학 특성을 평가하였다.
실험 결과 용량이 향상된 것을 확인할 수 있었으며 특히 고속 충방전
특성 또한 향상된 것을 확인 할 수 있었다.

주요어 : 나노 다공 구조, 전기 화학, 가스 센서, pn junction, 양극 산
화, 전기 도금, 원자층 증착법, 나노 튜브, 리튬이차전지, 음극, 산화주
석, 산화구리, 산화 티타늄.

학 번 : 2009-31239